






Designed and biologically active protein lattices

Shih-Ting Wang ¹, Brian Minevich², Jianfang Liu³, Honghu Zhang¹, Dmytro Nykypanchuk¹, James Byrnes⁴, Wu Liu⁵, Lev Bershady¹, Qun Liu ⁵, Tong Wang ⁶, Gang Ren ³ & Oleg Gang ^{1,2,7}✉

Versatile methods to organize proteins in space are required to enable complex biomaterials, engineered biomolecular scaffolds, cell-free biology, and hybrid nanoscale systems. Here, we demonstrate how the tailored encapsulation of proteins in DNA-based voxels can be combined with programmable assembly that directs these voxels into biologically functional protein arrays with prescribed and ordered two-dimensional (2D) and three-dimensional (3D) organizations. We apply the presented concept to ferritin, an iron storage protein, and its iron-free analog, apoferritin, in order to form single-layers, double-layers, as well as several types of 3D protein lattices. Our study demonstrates that internal voxel design and inter-voxel encoding can be effectively employed to create protein lattices with designed organization, as confirmed by in situ X-ray scattering and cryo-electron microscopy 3D imaging. The assembled protein arrays maintain structural stability and biological activity in environments relevant for protein functionality. The framework design of the arrays then allows small molecules to access the ferritins and their iron cores and convert them into apoferritin arrays through the release of iron ions. The presented study introduces a platform approach for creating bio-active protein-containing ordered nanomaterials with desired 2D and 3D organizations.

¹Center for Functional Nanomaterials, Brookhaven National Laboratory, Upton, NY, USA. ²Department of Chemical Engineering, Columbia University, New York City, NY, USA. ³The Molecular Foundry, Lawrence Berkeley National Laboratory, Berkeley, CA, USA. ⁴Energy Sciences Directorate/Photon Science Division, NSLS II, Brookhaven National Laboratory, Upton, NY, USA. ⁵Biology Department, Brookhaven National Laboratory, Upton, NY, USA. ⁶Advanced Science Research Center at the Graduate Center of the City University of New York, New York City, NY, USA. ⁷Department of Applied Physics and Applied Mathematics, Columbia University, New York, NY, USA. ✉email: og2226@columbia.edu

The assembly of proteins, nature's most powerful and versatile building blocks, into rationally organized arrays is of substantial interest for enabling protein-containing materials and their cell-free functionality^{1–4}. Establishing approaches for creating protein-based well-ordered structures has been a long-standing focus of structural biology for revealing their atomic structures⁵. Although such protein crystals can teach us about the bio-machinery through detailed structural information, crystallization methods are not compatible with creating biologically active protein organizations, nor exploring their function in operando. The need for developing methods to design and form 3D functional protein arrays has become even more apparent for addressing outstanding problems in cellular^{6–9} and tissue engineering^{10,11}, fabrication of multi-enzyme systems^{12,13}, for proteomic profiling¹⁴ and synthetic biology applications¹⁵.

Establishing methodology for building desired organizations of proteins remains challenging due to the varied and transient nature of protein shapes, and chemical and charge heterogeneities of their surfaces. Thus, individual systems typically require unique approaches, such as optimization of conditions in protein crystallography⁵ and protein coacervation⁹, design of protein interfaces^{16–18}, and use of protein cages^{2,19,20}. It is highly attractive to consider methods for assembling proteins into desired spatially organized systems.

The original idea of using DNA as a structural material, proposed by Seeman²¹ almost four decades ago, strived to address a challenge faced by protein crystallography in generating atomically defined 3D protein organizations. The idea has given rise to the field of DNA and RNA nanotechnology, where sequentially defined polynucleotide polymers can be programmed into different structural states to form designed nucleic acids constructs^{22–28} that can be assembled in ordered 2D^{29–31} and 3D organizations^{32–37}, with different degrees of structural fidelity. Structural control offered by DNA-based methods is highly attractive for creating 3D nanoscale organizations of functional inorganic nanoparticles^{33,38–44}. Recent efforts demonstrate that designed DNA constructs can be coupled with proteins, allowing for applications in bio-catalysis^{45,46}, nanomedicine^{47–51}, probing biological structures^{52,53} and processes^{6,54,55}, and manipulation of protein functionalities^{13,56}. Although it was demonstrated that enzymes can be organized in space⁵⁷ and their 3D ordered cascades³³ can exhibit an enhanced activity, gaining an engineering control over the organization of biologically functional proteins, which often comprise multiple subunits, and symmetric or asymmetric domains, remains an elusive and highly desirable goal.

The quest for orchestrating the assembly of one or many types of proteins into a bio-active and fully prescribed 3D scaffold has become more evident with a rapid conversion of nanotechnology and synthetic biology towards developing molecularly controlled systems. Several challenges have to be solved in order to establish a broadly applicable strategy for creating bio-active protein arrays, regardless of their shape and surface groups, while maintaining an environment and molecular transport for their operation. They include: (i) “transparency” for molecular transport, (ii) a structural designability; and (iii) a broad protein integration suitability. These problems, as we show below, can be tackled by DNA-based approaches by trading a complex inter-protein interaction for Watson–Crick base-pairing, which can be controlled on multiple length scales.

In this work, we demonstrated that DNA material voxels, polyhedral DNA frames with encapsulated nano-objects, could integrate with proteins and be adapted for assembly of ferritin, a biological functional iron storage protein macromolecule (~450 kDa, 24 subunits) and its coreless, iron-free form, apoferritin, into desired ordered arrangements, including single-layer, double-

layer, and different types of 3D lattices. Here, we created functional protein arrays by combining internal voxel design, which tailored placement of protein inside DNA voxels, and inter-voxel encoding, which provided connectivity control. The work showed that assembled proteins remained active in a lattice and their state could be structurally monitored in situ. The detailed probing revealed an excellent correspondence between electron microscopy (EM), EM-based tomography, and small-angle X-ray scattering (SAXS), while SAXS further captured iron ion release kinetics from the ordered 3D ferritin arrays. This demonstrated a feasibility for creating organized protein systems as fully designed protein-based materials with preserved inherent characteristics and biological activity, and as a general methodology for investigating protein conformations and interactions.

Depicted in Fig. 1 is the concept of our developed approach for assembly of biologically functional proteins into ordered arrays through programmable DNA frameworks that can host and control the placement of the guest proteins within each voxel. To demonstrate the applicability of the proposed concept, our selected proteins, ferritins, and apoferritins were grafted with single-stranded (ss) DNA through covalent chemistry to facilitate high efficiency (~70%) of encapsulation inside the 3D wire-framed octahedral origami (Octa, Supplementary Figs. 1 and 2)^{40,42} via hybridization with complementary ssDNA at designated sites of Octa. This strategy generates a “protein voxel” with a tailored ferritin or apoferritin placement within. In order to create 2D and 3D protein arrays, we encode the specific voxels' vertices to facilitate a desired inter-vertex hybridization and to drive the assembly of designed arrays. A combination of the two strategies, a protein voxel and programmable assembly of voxels, offers control over the formation of protein arrays with prescribed lattice symmetries. The open architecture of the individual frames and assembled framework provide a native protein environment and molecular accessibility to proteins (Fig. 1). We demonstrate that the structural stability of ferritin and its biological activity to release iron ions are maintained within the assembled arrays.

Results

The selected proteins, ferritin and apoferritin from the horse spleen (Sigma), were composed of 24 subunits and shared a shell topology with ferritin containing a distinctive iron core. Each subunit consisted of ~9 primary amines (PDB IDs: 1IER and 2W0O) which enabled surface modification using DNA. We first analyzed, using negative-stained TEM imaging, ferritin, and apoferritin, and both showed average sizes of ~12 nm at dry states (Fig. 2). The native proteins in solution were probed by in situ SAXS, where both proteins exhibited oscillations. Ferritin showed a smaller amplitude and period of oscillations than apoferritin (Fig. 2c and Supplementary Fig. 3), and these observations were in good agreement with our scattering models, accounting for the core-shell protein structure (see “Methods” section). The fitted form factors revealed overall diameters of ~12 nm with 7–8 nm iron core and cavity for ferritin and apoferritin, respectively (Fig. 2c). The close correspondence between TEM and SAXS was also in agreement with crystallographic studies, exhibiting core and shell diameters of about 8 and 12 nm, respectively^{58,59}.

To efficiently encapsulate proteins in the frame, we established a two-step chemical conjugation process, in which the primary amines of ferritin or apoferritin were first activated by a bifunctional crosslinker through *N*-hydroxysuccinimide (NHS)-amine reaction, followed by covalent coupling of the dibenzocyclooctyne (DBCO) modified ssDNA using click chemistry (see “Methods” section). Agarose gel electrophoresis and dynamic light scattering (DLS) confirmed the successful protein modification, and UV-vis

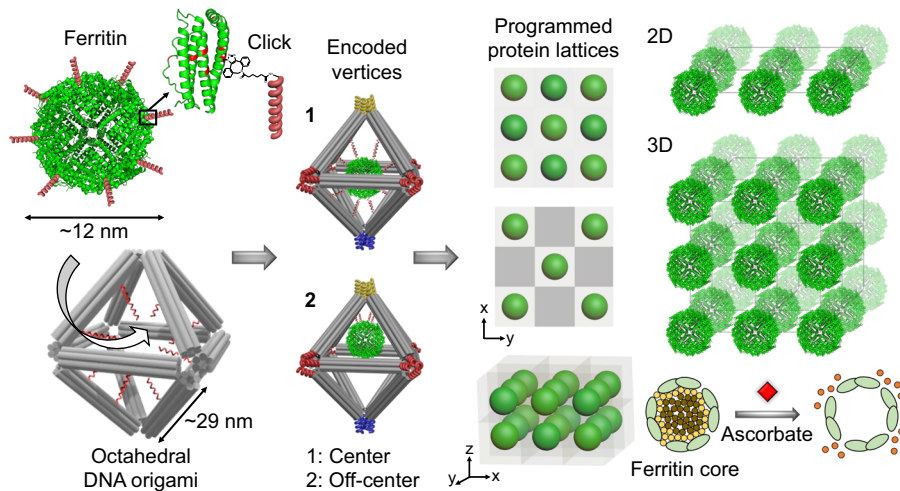


Fig. 1 The concept of programmable assembly of bio-active 2D and 3D protein arrays by integrating ferritin with DNA frames (octahedra, Octa) into protein voxels. A high-yield stable frame-encapsulation of ferritin and apoferritin into protein voxels and their assembly into ordered arrays through a stepwise modification of protein (ferritin, PDB ID: 1IER) surfaces (at the lysine residues (red)). A targeted placement of proteins, encoded with DNA sequences, at the frame’s center (1) and shifted toward a vertex (2). Various positions of the encapsulated ferritin (see “Methods” section and Supplementary Fig. 7 for design in detail) inside the frame can be prescribed, as discussed later in the text. The designed 2D single- and double-layered, and 3D ferritin and apoferritin lattices were formed by establishing prescribed vertex-to-vertex Watson-Crick interconnections. The 3D ordered ferritin array could be converted into a coreless apoferritin array with preserved structure using ascorbate to reduce and release iron ions (orange circles) from ferritin.

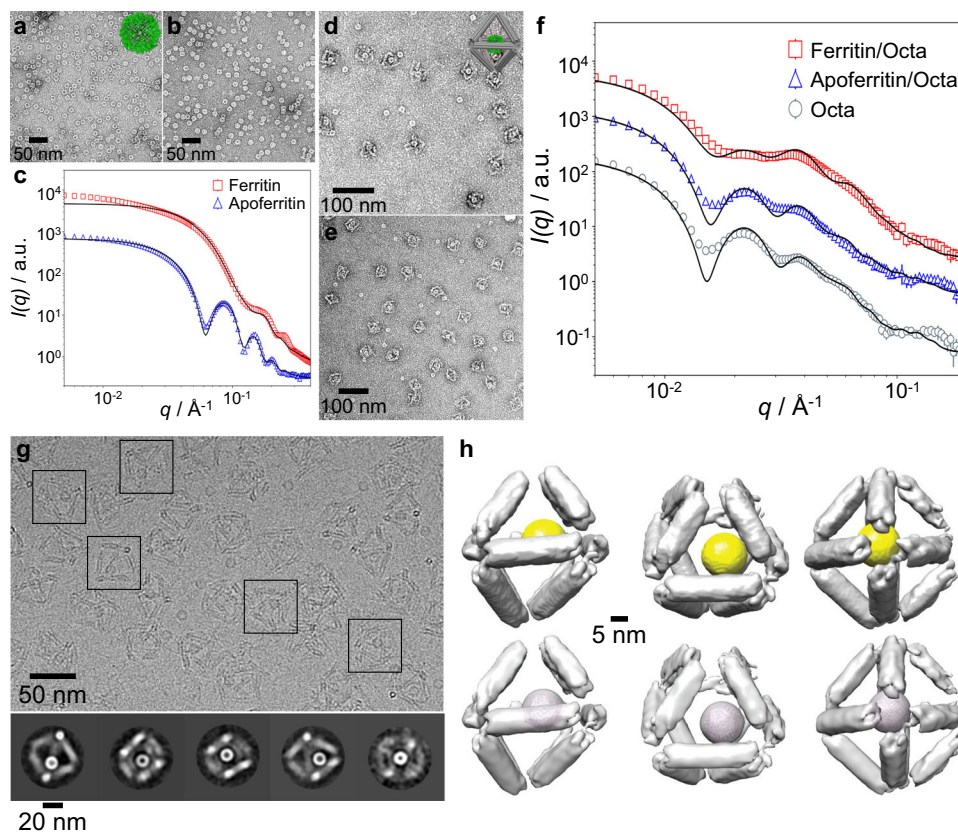


Fig. 2 Protein voxels: ferritin and apoferritin placed in the center (position Off₀) of Octa frames, and characterized by in situ SAXS, ex situ TEM, and cryo-EM. **a, b** Negative-stained TEM imaging (**a** ferritin, **b** apoferritin) and **c** SAXS measurement and analysis of free ferritin and apoferritin in solution (intensity profiles were shifted vertically for clarity). **d, e** Negative-stained TEM imaging (**d** ferritin/Octa, **e**: apoferritin/Octa) and **f** SAXS data and analysis of ferritin and apoferritin encapsulated inside Octa (intensity profiles were shifted vertically for clarity). The insets in **a** and **d** show illustrated views of ferritin (PDB ID: 1IER) and ferritin/Octa. **g** Cryo-EM micrograph (top row) and 2D reference-free class average (bottom row) provided representative views of apoferritin/Octa. The black squares enclose the representative structures. **h** Surface-rendered 3D density maps of apoferritin/Octa, viewed from the two-fold (left), three-fold (middle), and four-fold (right) symmetry axes. In the bottom view, the apoferritin model (PDB ID: 2W00) is docked in the density of apoferritin.

analyses indicated about 6–7 ssDNAs were attached per ferritin (Supplementary Figs. 4–6). The ssDNA-grafted proteins were mixed with Octa frame, which had complementary ssDNA chains extended from select DNA bundles to position guest proteins at prescribed positions inside Octa (Supplementary Fig. 7), followed by heating to 48 °C and slowly cooling to room temperature. For symmetric encapsulation of proteins (Fig. 2 and Supplementary Fig. 7), we positioned them at the center of the Octa frame (termed Off0) using eight internal anchoring ssDNA, located on four meridian bundles that complemented with $l = 15$ nucleotides (nt) of ssDNA on proteins, with remaining ssDNA parts of $m = 24$ nt and $n = 3$ nt on the bundles and the protein, respectively. A protein position inside Octa could be modulated by changing the length and position of the internal anchoring strands (Supplementary Fig. 7). Negative-stained TEM imaging confirmed protein encapsulation inside Octa by the additional globular shape at the Octa center (Fig. 2 and Supplementary Figs. 8, 9), and from ~400 imaged single particles, encapsulation yields were estimated as ~79% and ~70% for ferritin and apoferritin, respectively. Although for smaller proteins, the single-molecule fluorescence approach can be used to quantify the encapsulation⁶⁰, the size of ferritin and apoferritin permits a direct quantification of the encapsulation using electron microscopy.

The integrity of Octa frame after protein encapsulation is important for the robust assembly of protein arrays. Neither electrophoresis nor DLS detected significant Octa changes after encapsulation (Supplementary Figs. 10 and 11). Next, we performed in situ SAXS measurements to analyze protein voxels. The form factor of an empty Octa (Fig. 2f and Supplementary Fig. 12) had the first two local maxima at the momentum transfer values of $q_1 = 0.022 \text{ \AA}^{-1}$ and $q_2 = 0.038 \text{ \AA}^{-1}$. Ferritin and apoferritin voxels exhibited an intensity reduction at q_1 and an increase at q_2 , suggesting co-localization of Octa and proteins. For quantitative understanding, we applied a SAXS model with rigid Octa constructed from twelve cylinders and protein in the center. Our fitting (see “Methods” section) resulted in a cylinder’s length of 27.8 nm, which agreed with the nominal design of 28.6 nm Octa edge and a protein voxel (Fig. 2f and Supplementary Fig. 13)^{33,61}. The deviations from the fitted results are likely due to the possible distortions of the octahedron and some fluctuations of its shape, which is also indicated by cryo-EM measurements, as described below.

To reveal the structural details in 3D and in real space, Octa and protein/Octa were further analyzed by single-particle reconstruction by cryo-EM imaging. Using reference-free 2D class averages (Supplementary Fig. 14), the 3D density maps of Octa with a resolution of ~22.9 Å were reconstructed, which revealed the octahedral frame with edge lengths of ~29 nm, which agreed with both our design and the SAXS results (Supplementary Fig. 13). Note that some distortion at the bundle connecting vertices was observed, likely due to internal stress. For cryo-EM imaging of protein/Octa, we selected apoferritin, of which its electron density was comparable to Octa. Figure 2g, h shows that the 2D class averages of raw particle images of apoferritin/Octa were nearly identical to those of Octa (Supplementary Fig. 14) except for the extra circular density at the frame’s center. Remarkably, apoferritin/Octa distinguished from Octa showing the additional spherical 3D density in the Octa’s cavity and that the crystal structure of apoferritin was docked well into the averaged spherical 3D densities, suggesting that apoferritin was proximate to the designed Octa’s center. A slightly off-centered positioning of apoferritin inside Octa was likely due to unformed DNA-protein linkages or minor distortions of Octa.

The structural stability of protein voxels allowed us to further use them as assembly “bricks” for creating targeted protein

organizations. First, we constructed single- and double-layered 2D lattices (Figs. 3 and 4), where Octa vertices were encoded with distinctive ssDNA, referred to as “colored” bonds^{29,62}. Here, the 2D single-layered lattices were built using two different Octa with each having four complementary encoded equilateral vertices, so-called “one-color” system (Fig. 3a and Supplementary Fig. 15). Furthermore, two lattice types were designed, where a full-filled lattice from protein voxels and a half-filled lattice using alternating protein voxels and empty voxels (Fig. 3a). A one-pot assembly procedure was applied, where a mixed solution of encoded Octa and protein was heated up to 48 °C and then slowly cooled to room temperature to ensure thermodynamically equilibrated structures for a protein encapsulation and lattice formation.

The as-formed single-layered full-filled lattices were visualized by negative-stained TEM imaging (Fig. 3 and Supplementary Figs. 16, 17). In situ SAXS analysis of the 2D empty and protein-filled voxel arrays revealed ~5 diffraction peaks (Fig. 3d and Supplementary Figs. 18, 19), indicating a square lattice with lattice constant $a_{\text{SL-Octa}} = 55 \text{ nm}$ for both cases. Co-localization of Octa and proteins was concluded from a reduced scattering intensity in the intermediate q range ($0.015\text{--}0.030 \text{ \AA}^{-1}$) and was attributed to the form factor of protein/Octa. Such results were supported by our model that took into account the form factors of protein and Octa and this type of 2D Bravais lattice. In the half-filled design (Fig. 3a), the lattice constant changed from $a_{\text{SL-Octa}}$ to $\sqrt{2}a_{\text{SL-Octa}}$ (Fig. 3d and Supplementary Figs. 18, 19), as expected.

In order to visualize the 2D lattice and ferritin positioning in real space in 3D, we used cryo-electron tomography (cryo-ET) and 3D reconstruction techniques. As shown in Supplementary Fig. 20, cryo-EM imaging of the lattice solutions embedded in vitreous ice, confirmed the micron-sized lattice domains, and distinguished the single-layered protein- and empty-voxel lattices by the dark spots from the ferritin core. Cryo-ET images were obtained from a series of tilt angles from -51° to $+51^\circ$ at a 3° increment. The representative tilt images (Supplementary Fig. 21) and correspondent 3D density maps (Fig. 3e, f) revealed encapsulated ferritins in the 2D lattice by the additional globular density. High-resolution 3D reconstruction was achieved by the individual particle electron tomography (IPET)⁶³ with missing-wedge correction techniques⁶⁴, by focusing on small selected areas of a lattice to avoid image distortion at a larger scale⁶⁵. Here, an area of the ferritin/Octa lattice was selected for serial refinement to obtain a final IPET 3D density map (Fig. 3 and Supplementary Fig. 22). Nearly all 12 DNA bundles of Octa and the encapsulated ferritins (black arrows in Supplementary Fig. 22d) could be resolved at a resolution of ~225 Å. Thus, local orders and a highly preserved connectivity of the single-layered lattice in each direction, with ferritins docked well into the framework were revealed, which agreed with our design and SAXS analysis (Fig. 3d). We note a distribution of orientations among octahedra in the single-layer lattice (Fig. 3e, f), which is likely due to 2D connectivity and flexibility of the inter-voxel motifs. This is further confirmed by comparison with the double layer as we discussed below. Such an orientational distributions can contribute to the reduction of SAXS peaks comparatively to the model (Fig. 3d).

To further demonstrate a versatility of our approach for protein lattice engineering, we created lattices by designing both the protein voxel and inter-voxel assembly to generate specific lattice symmetries. For protein voxels, by changing the ssDNA’s length and position, we shifted the protein from Octa’s center (or Off0) toward a vertex at two positions, defined as Off1 and Off2. As shown in Fig. 4a and Supplementary Fig. 7 and confirmed by

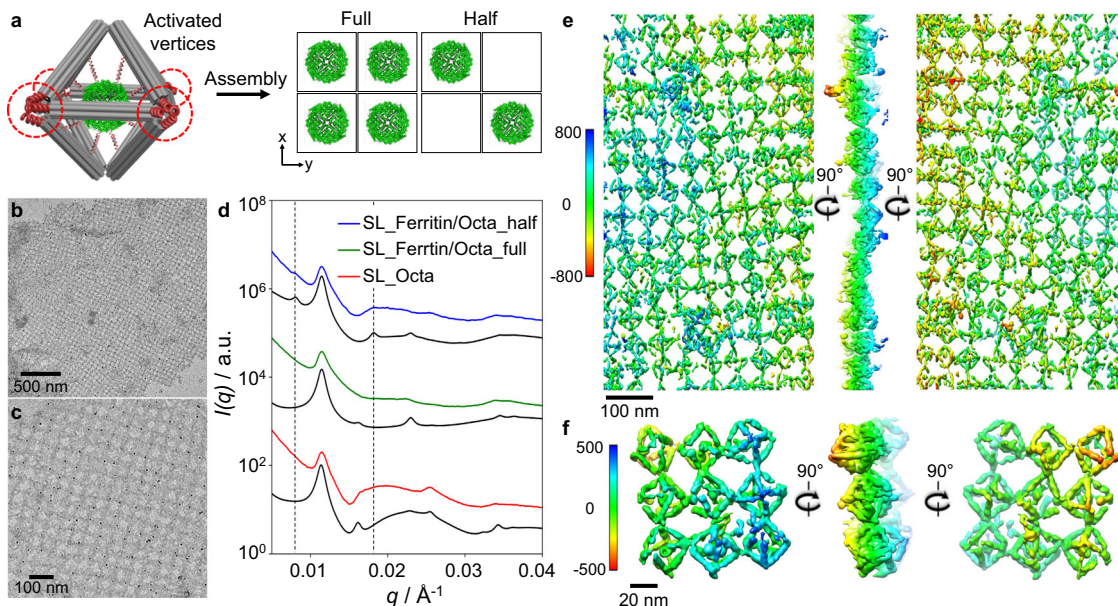


Fig. 3 Ferritin assembly in ordered 2D single-layered array. **a** Schematics showing a projected view of 2D single-layered (SL) protein/Octa lattices, where the in-plane vertices were encoded by one set of complementary DNA pairs (i.e., a one-color system). Ferritin was placed at the center of Octa for assembly into a fully integrated lattice, and a half-filled lattice by alternating the ferritin/Octa and empty Octa in the same lattice. **b, c** Negative-stained TEM images of SL ferritin/Octa lattices, where **c** shows a magnified image of the lattice. **d** SAXS data and analyses of SL ferritin/Octa lattices, in which the experimental data (colored lines) and the corresponding simulated results (black lines) were presented for Octa and the different types of ferritin/Octa lattices (measured and calculated intensity profiles were shifted vertically for clarity). **e, f** Cryo-ET 3D reconstruction of an SL ferritin/Octa lattice, where a series of tilted cryo-EM images were aligned and reconstructed in 3D without averaging using the IMOD and IPET software. The 3D density maps showed an overlay of the encapsulated ferritin with the SL lattice in one structure, indicating the overall conformation of the ferritin/Octa lattice. (**e**: selected lattice area and **f**: the representative views). The ferritin positions in **f** were indicated by the black arrows in Supplementary Fig. 22d. The color bars indicate Z height (unit: Å).

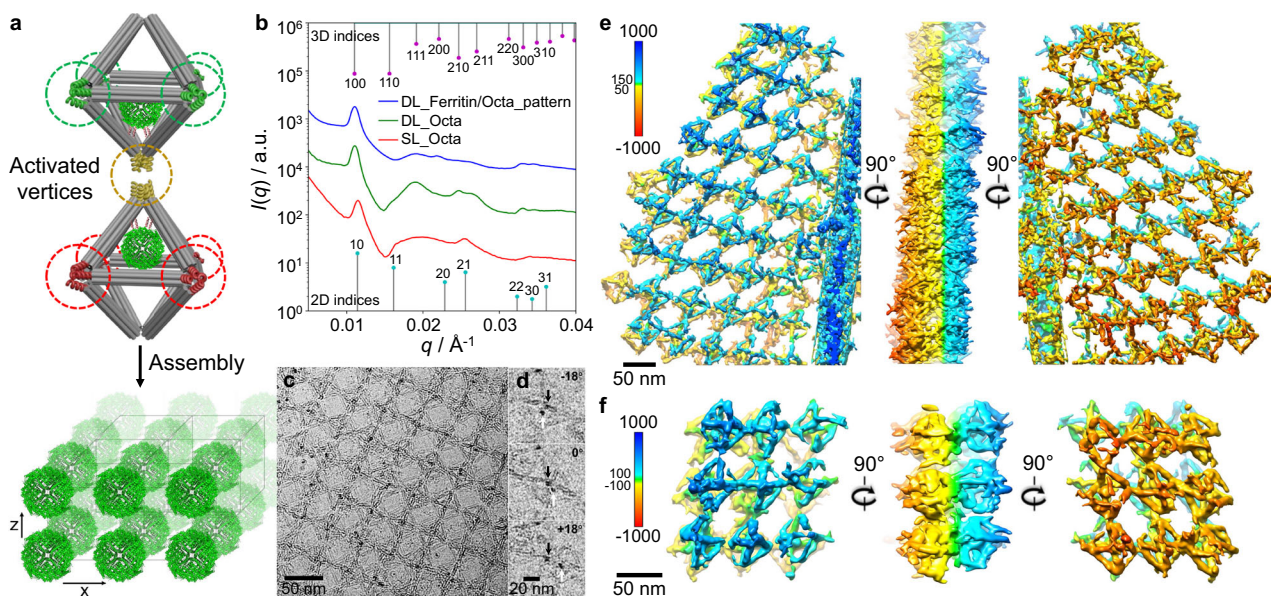


Fig. 4 Ferritin assembly in a double-layered lattice. **a** Schematic view showing a 2D double-layered (DL) protein/Octa lattice formed by a three-color vertex encoding system consisted of encoded Octa frames with five activate vertices and three sets of complementary DNA pairs (red, green, and yellow). Protein voxel with off-centered ferritin (Off2) was used as discussed in the text. **b** SAXS profiles (shifted vertically for clarity) of the DL empty Octa and ferritin/Octa lattices show co-localization of ferritin and the Octa lattice by the reduced intensities attributed to the ferritin core. The formation of a DL structure was supported by the emergence of broad peaks at the 3D indices of a simple cubic lattice, indicating a layer in the z direction. **c** A cryo-ET image of a DL lattices. **d** Representative cryo-ET images showing the two ferritins in the top and bottom layers at tilted angles (black and white arrows) in a DL lattice, which agreed with our design. **e, f** Cryo-ET 3D reconstruction of DL ferritin/Octa lattice without averaging. The 3D density maps showed the encapsulated ferritin overlaid well with the DL lattice (**e** selected lattice area and **f** representative views, see the text and “Methods” section for details). The ferritin positions in **f** were indicated by the black arrows in Supplementary Fig. 32d. The color bars indicate Z height (unit: Å).

TEM and in situ SAXS (Supplementary Figs. 23–25), proteins were shifted from the Off0 using 4 internal strands from the selected vertex, where the ssDNA on DNA bundles (m) was 15 nt for Off1 and 9 nt for Off2; both n and l remained the same as for Off0. The SAXS analysis indicated that the protein was shifted by 1.5 nm and 3.5 nm for the Off1 and Off2 designs, respectively. We utilized the off-center protein voxel (Off2), for creating a double-layered protein array with an unequal distance between proteins in the x - y and z directions (Fig. 4a). Our design comprised four distinct Octa and three distinct sets of complementary DNA pairs (i.e., a “three-color” system), two of which were utilized for in-plane (x - y) hybridization of vertices within each layer (Fig. 4a, green and red, Supplementary Fig. 26), and one (yellow) for connecting two layers in the out-of-plane (z) direction. Due to the off-centered protein in a voxel, this design encoded a lattice with an unequal distance between proteins in the x - y and z directions.

Negative-stained TEM imaging confirmed the lattice formation with micron-sized domains (Supplementary Figs. 27–29). In situ SAXS analysis revealed that the double-layered and single-layered lattices shared similar features, with 1st peak was attributed to the in-plane spacing, $a_{DL,Octa} \sim 57$ nm (Fig. 4b and Supplementary Fig. 30). An indication of out-of-plane structure ($q = 0.019$ and 0.027 \AA^{-1}), attributed to the (111) and (211) planes was observed, which could only occur when at least two layers in the z direction were present. The SAXS analysis showed that proteins did not affect the DNA lattice integrity, while proteins occupied positions prescribed by the Octa framework (Fig. 4b, Supplementary Fig. 30). We further visualized assembled arrays in 3D using cryo-ET, as discussed above (Fig. 4d and Supplementary Figs. 31, 32). The final 3D maps (Fig. 4e, f) were resolved at a resolution of 156 \AA (Fig. 4f and Supplementary Fig. 32) and confirmed the double-layered lattice, where the reconstructed array presented the top (blue) and bottom (orange) layers at 90° rotations. Octa connecting in the same plane by four vertices and with another layer via one vertex, as well as ferritin docking inside (black arrows in Supplementary Fig. 32d) agreed with our design and the SAXS results (Fig. 4b). A cryo-ET imaging reveals that a formed double-layer lattice (Fig. 4e, f) exhibits an improved orientational order over a single-layer lattice (Fig. 3e, f), which is attributed to an additional binding in z direction that stabilizes the octahedra orientations.

In the next step, we extended the presented protein assembly strategy for creating several types of designed 3D protein arrays. We programmed different color-encoded inter-vertex hybridizations of the protein voxels to achieve different 3D protein patterns, where four in-plane vertices bound to four x - y neighboring Octa and the out-of-plane vertices were engaged in layers in z direction. Specifically, a “one-color” system composed of two different Octa and one set of complementary DNA pairs (Fig. 5a and Supplementary Fig. 33), and a “four-color” system included four different Octa with four sets of complementary pairs (Fig. 5a and Supplementary Fig. 34). We designed three types of protein arrays: (i) a “full-filled” array that assembled one-colored protein voxels in a SC lattice (2 in Fig. 5a); (ii) a “half-filled” array that assembled alternating protein and empty one-colored voxels into a face-centered cubic (FCC) lattice (3 in Fig. 5a); and (iii) a “patterned” array that assembled the off-centered (Off2) protein voxels in the 3D lattice of commensurately stacked double-layers using a four-color scheme (4 in Fig. 5a). Similar to 2D lattices one-pot assembly was employed following several days of annealing and cooling.

First, we assembled and probed the one-color and four-color empty Octa 3D lattices (Fig. 5a), which shows a simple cubic (SC) lattice with the constants of 57.6 and 58.6 nm, respectively (Supplementary Figs. 35, 36 and 38)⁶⁶. For the full-filled protein

lattice (2 in Fig. 5a), SAXS revealed a high degree of long-range SC order (constant 58.3 nm), as indicated by at least 15 orders of resolution-limited Bragg peaks, and excellent agreement between the experimental and the modeled $I(q)$ profiles (Fig. 5b and Supplementary Fig. 36). Compared to the 3D apoferritin/Octa and empty Octa lattices, incorporation of ferritin into the 3D lattices reduced intensities at $q = 0.019$, 0.025 , and 0.027 \AA^{-1} , or the (111), (210), and (211) planes (Supplementary Figs. 37 and 38), due to its iron core.

Next, we realized 3D lattices with alternating “half-filled” and “patterned” designs, as shown in 3 and 4, respectively in Fig. 5a. In the half-filled array, every next-neighbor voxel in SC array was empty, thus, a face-centered cubic (FCC) was expected. Correspondingly, SAXS profile showed peak positions at ratios $q_n/q_1 = 1 : \sqrt{4/3} : \sqrt{8/3} : \sqrt{11/3} : 2 \dots$, indicating FCC lattice with a lattice constant of 115.9 nm. The SAXS modeling supported this conclusion (Fig. 5b and Supplementary Figs. 36–38).

Finally, we designed a 3D patterned lattice, in which a double-layer formed by protein voxels (Off2) were stacked in the z direction, facing each other similarly to the double-layer design. This arrangement would result in a lattice with a primitive tetragonal unit cell which was slightly altered from SC lattice due to only a few nm protein shift (Off2). Our SAXS experiment revealed a successful lattice formation. The detailed modeling, accounting for the ferritin shift, showed that relative peak intensities should be affected, as well as a small peak should appear at the low- q region at sufficiently large shifts (Supplementary Fig. 39). We indeed observed an intensity increase at $q = 0.024 \text{ \AA}^{-1}$ ((210) plane) and no low- q peak appearance, which suggests a protein shift < 3 nm in a tetragonal lattice.

Following the assembly studies, we investigated the biological activity of ferritin in the assembled SC lattice. Sodium ascorbate (SA) was used to reduce ferric hydroxide of the mineral core^{67,68} and facilitated an iron release and conversion of the 3D ferritin array to an apoferritin array (Fig. 6a). To promote this process, an acidic environment was created by the addition of ammonium acetate (NH_4Ac , 0.2 M, pH 5.5). A Ferrozine assay was first used to assess the release of iron ions from ferritin into solution, in which Fe^{3+} from the ferritin core was reduced by SA. The ferrous ions (Fe^{2+}) complexed with Ferrozine were detected by UV-vis absorbance at 562 nm for ferritin but not apoferritin (Supplementary Fig. 40). We note that some formation Ferrozine- Fe^{2+} complex was detected from the ferritin sample in the acidic environment without SA, but a $\sim 3\times$ increase in absorbance was observed with SA (Supplementary Fig. 40). A majority of proteins remained intact under SA/ NH_4Ac reduction, as supported by DLS and TEM (Supplementary Fig. 41). To investigate the core dissolution of encapsulated ferritins, a form factor of single ferritin/Octa was analyzed by in situ SAXS after 5 h treatment with SA. The recovery of the two maxima in a form factor of protein voxels at $q = 0.022$ and 0.038 \AA^{-1} indicated a reduced electron density of the iron core of the encapsulated ferritin, while TEM confirmed that proteins remained in Octa (Supplementary Fig. 42). Thus, we concluded that a ferritin voxel could be converted into an apoferritin voxel.

We applied a similar SA/ NH_4Ac reduction conversion approach to a 3D full-filled (SC) lattice (Fig. 6a). SAXS pattern, plotted as q_n/q_1 , exhibited a change in relative peak intensities (dashed vertical lines in Fig. 6b, Supplementary Fig. 43), including a suppression of 2nd peak and enhancements of 3rd and 4th peaks (Fig. 6c, d), resembling scattering pattern of the apoferritin lattice. These changes stabilized after 6 h, suggesting that the reduction reaction had reached equilibrium (Fig. 6d). Overall, the lattice integrity was preserved, while its slight compaction (4.8% lattice constant decrease) was attributed to the charge interactions

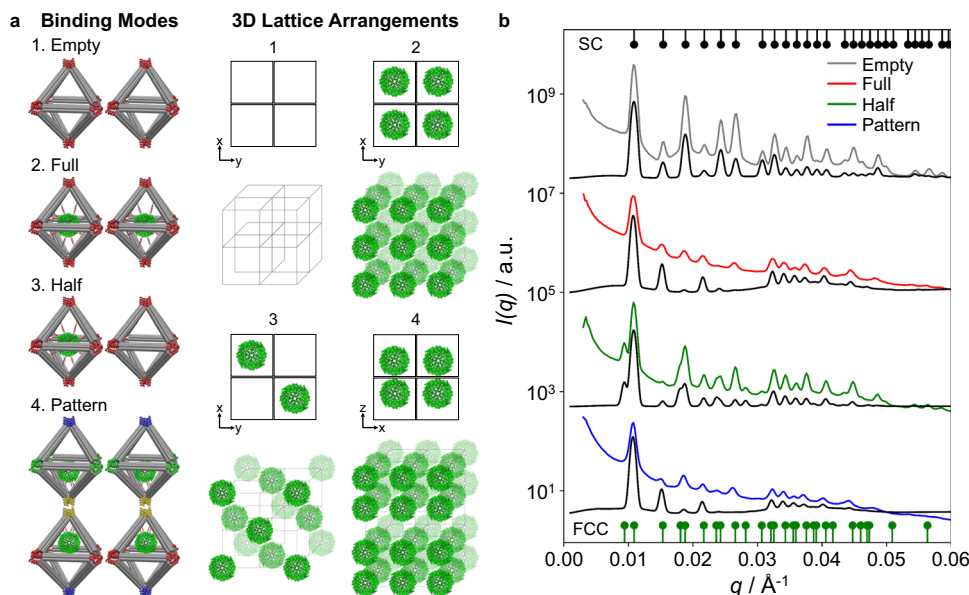


Fig. 5 Design of 3D designed ferritin arrays and their in situ SAXS analyses. **a** Schematic view showing the 3D protein/Octa lattices formed by encoded Octa voxel. Depending on the activated vertices and the encoding sequences which facilitated a variety of binding modes, four different types (i.e., empty, full-filled, half-filled, and pattern) of unit cells of the 3D Octa and ferritin/Octa lattices were designed, as presented by the 2D projections and 3D views. **b** Experimental (colored curves) and simulated (black curves) $I(q)$ profiles (shifted vertically for clarity) of the different types of 3D ferritin/Octa lattices. Gray (empty Octa, control) and red (full-filled ferritin/Octa) curves correspond to a simple cubic (SC) lattice, green (half-filled ferritin/Octa) curve relates to an face-centered cubic (FCC) lattice, and blue (pattern ferritin/Octa) curve corresponds to a tetragonal lattice, see text and “Methods” section for details. The 3D indices of a SC (bottom) and an FCC lattice (top) are indicated, respectively.

between NH_4^+ and negatively charged DNA backbone of Octa (Supplementary Fig. 43).

To estimate the degree of core reduction in the 3D ferritin array, SAXS profiles at different reaction times were compared with our models considering the size and electron density of the core-shell proteins (Supplementary Fig. 44). We simulated the biological core dissolution pathway^{67,68} by building three models that accounted for different mechanisms of iron core decrease: from the surface of the iron core (route 1), a uniform reduction of the core (route 2)⁶⁹, and from the center of the core (route 3) (Fig. 6e and Supplementary Fig. 45). SAXS modeling for route 1 (Fig. 6e–g), which is in excellent agreement with the experimental results (Fig. 6b–d), estimated an iron decrease in the assembled ferritins by 66%, as indicated by the intensity reduction at $q_2 = 0.0159 \text{ \AA}^{-1}$ and increase at $q_3 = 0.0195 \text{ \AA}^{-1}$ and $q_4 = 0.0225 \text{ \AA}^{-1}$ during the conversion (dashed lines in Fig. 6e).

We further considered other iron release mechanisms, and applied SAXS modeling to their evolutions. In the absence of SA, all three pathways showed an estimated 20–30% core reduction, likely due to a partial iron release from ferritin in the acidic environment (Supplementary Fig. 40). However, reduction of the ferritin cores was significantly increased to 60–75% in the presence of SA, and the three modeled pathways yielded close values, which was 75% for route 2 and 61% for route 3 from the SAXS experiment (Fig. 6e and Supplementary Figs. 46, 47). Our SAXS modeling of the three pathways also suggested core reduction was maximized at these values (i.e., 2nd peak reached a minimum, see Supplementary Figs. 45–47 for details), which is consistent with our time-dependent study (Fig. 6d). Thus, the study shows that ferritins organized in a 3D lattice are able to release a significant amount of iron ions.

Discussion

This work demonstrated an effective approach for the by-design assembly of 2D and 3D protein lattices with preserved biological

activity. In specific realization, we encapsulated ferritin, a biologically functional iron storage protein, inside octahedral DNA origamis (Octa), creating protein voxels with tailored internal structure and external bonds. Such voxels can be programmed to assemble into desired lattice symmetries through the specific control of their coordination. The assembly of 2D single-layer, double-layer, and 3D lattices was demonstrated in our study, as confirmed by cryo-EM 3D imaging and in situ scattering methods. In a 3D array, ferritin was densely packed with a local concentration $\sim 150\times$ higher than the free proteins in the same solution. The stability, integrity, and “transparency” for molecular transport of ferritin 3D lattices allow to convert them into apo-ferritin lattices, which accompanied by a release of micromolar level of iron ions. Our work offers a versatile approach for designing and assembling targeted protein-based designed nanomaterials, which present intriguing possibilities for biomaterials, bio-catalysis, nanomedicine, nanotechnology, and cell-free biology.

Methods

Preparation of octahedral DNA origamis (Octa). Octa was folded by mixing 20 nM of M13mp18 scaffold DNA and 100 nM of each staple oligonucleotides in TAE ($1\times$) buffer containing 12.5 mM MgCl_2 (TAE/ MgCl_2). The mixed solution was cooled from 90 °C to room temperature over 20 h to obtain target Octa. After synthesis, Octa were purified using the Amicon centrifugal filter units (100 kDa, Millipore Sigma) and centrifuged at 400 g and at 4 °C. Purification was repeated 6 times by adding fresh TAE/ MgCl_2 buffer in each cycle. Octa design and sequences are provided in Supplementary Fig. 1 and Supplementary Data 1–3.

Protein modification and encapsulation in single Octa. DNA grafting of ferritin and apoferritin was performed first by mixing the proteins (10 μM) with 0.75 mM azido-dPEG₈-NHS ester in PBS ($1\times$, pH 7.4) buffer and reacted for 3 h at room temperature or overnight (>12 h) at 4 °C. The azide-activated proteins were purified by Amicon centrifugal filter units (50 kDa, Millipore Sigma) and centrifuged at 3000 \times g and 4 °C for 9 times. Next, 0.35 mM of DBCO-modified ssDNA (TATGAAGTGATGGATGAT/3DBCON/) was added to the azide-activated

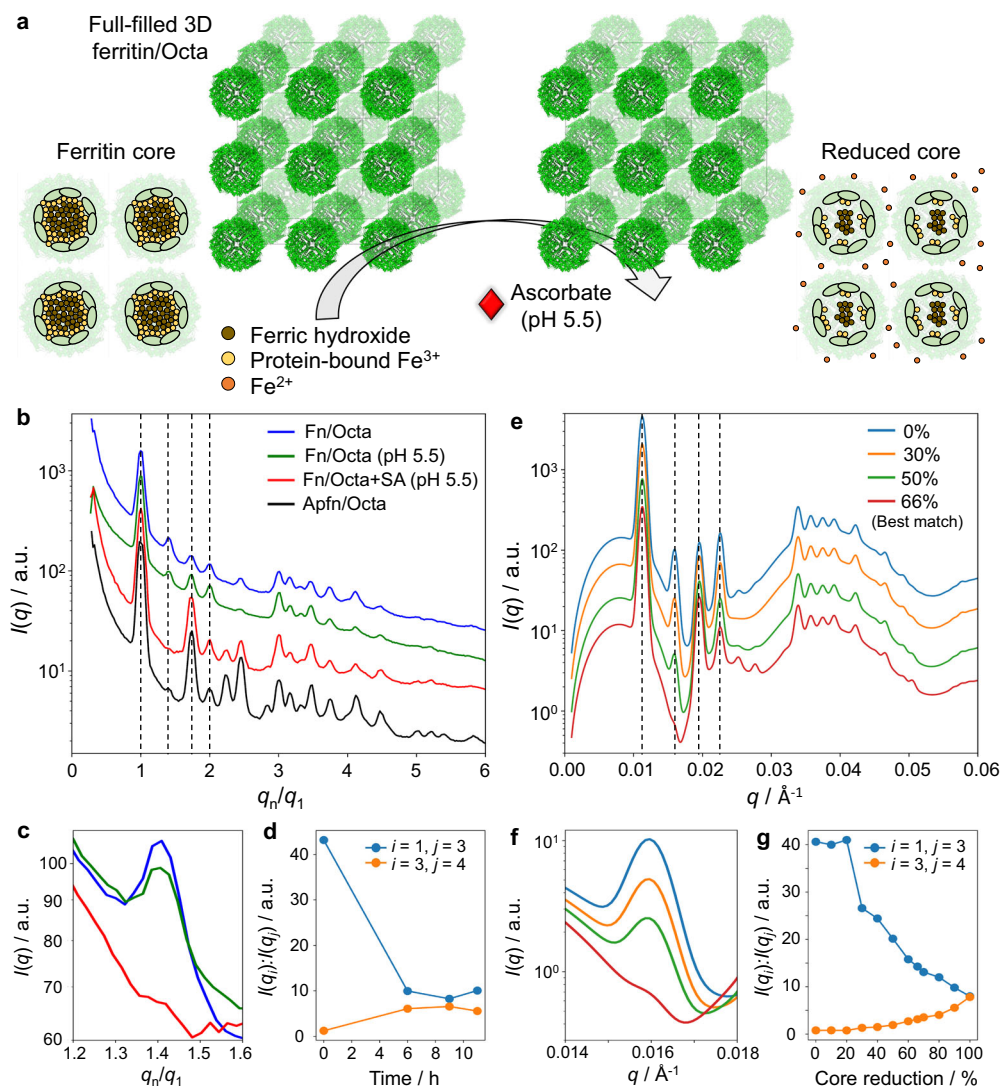


Fig. 6 Conversion of ordered 3D (SC) ferritin array into an apoferritin array. **a** Schematic view showing the conversion of a 3D ferritin into apoferritin array by reduction using sodium ascorbate (SA), see text for details. **b** In situ SAXS analysis showing the conversion of 3D ferritin/Octa lattice (Fn/Octa, blue) into an apoferritin/Octa (Apfn/Octa) lattice after 9 h incubation with SA (red) solution containing ammonium acetate (NH₄Ac, pH 5.5), and controls, Fn/Octa in NH₄Ac (green) and a native Apfn/Octa lattice (black). Peak positions were normalized by the center of the 1st peak. The peaks that changed their relative intensities during conversion were shown by the dashed lines. Intensity profiles were shifted by a factor two for clarity. **c** The changes in the intensity of the 2nd SAXS peak (corresponded colors in **b**). **d** Analysis of the time-dependent study (Supplementary Fig. 43) showing relative peaks intensities between the 3rd and 4th (orange), and the 1st and 3rd (blue) peaks, indicating that the reduction process completed after 6 h. **e** Conversion of the ferritin array was analyzed by SAXS modeling (route 1 is shown, see text for details; intensities were shifted vertically for clarity by factor two), which indicated about 66% reduction of ferritin array. **f** SAXS modeling and analysis of the 2nd peak in **c** agreed with the experimental results. **g** Estimated degrees of core reduction based on SAXS modeling (see “Methods” section and Supplementary Figs. 44 and 45). Routes 2 and 3 for core dissolution pathways (Supplementary Figs. 46f and 47f), resulted in close values in the range of 60–75% of reduced cores.

proteins (10 μM) in PBS and reacted overnight at 4 °C. The DNA grafted proteins were purified by filter units (100 kDa) and centrifuged at 3000 \times g and 4 °C for 9 times. The protein products were concentrated to 10 μM and stored at 4 °C. UV-vis was used to estimate protein concentration and the number of ssDNA on protein surfaces (about 6–7 ssDNA per ferritin), see Supplementary Fig. 4. To encapsulate protein in single Octa frames, Octa was mixed with the proteins (typically 40 nM for 30 nM Octa) in the TAE/MgCl₂ buffer and the mixed solution was heated up to 48 °C and cooled to room temperature over 40–60 h. Note that a lower starting temperature and shorter cooling time at higher temperatures should be considered depending on the protein stability.

Negative-stained TEM imaging. In brief, Octa and protein/Octa (5 μL , 5–10 nM) solutions were dropped on a carbon film for 2 min and the residual liquid was removed with a piece of filter paper. After that, the grid was washed with 5 μL of deionized water followed by staining with 5 μL of 2 wt % uranyl acetate for 10 s. The excess liquid was removed with filter papers. TEM imaging was performed on a JEOL 1400 TEM, operating at 120 kV. The yields of protein encapsulation were

obtained by direct counts from the TEM images. Among 394 counted apoferritin/Octa, 275 were well encapsulated and 119 were empty, yielding encapsulation of 69.8%; for ferritin/Octa, among 398 counted particles, 313 were well encapsulated and 85 were empty, yielding encapsulation of 78.6%.

Small-angle X-ray scattering (SAXS)

Data acquisition and processing. Solution scattering data of free proteins, single Octa, and single protein/Octa was collected at the Life Sciences X-ray Scattering beamline (LiX, 16-ID) at the National Synchrotron Light Source II (NSLS-II), Brookhaven National Laboratory (BNL). Protein samples (0.5–20 mg/mL) were prepared in PBS and Octa samples (10–50 nM) were prepared in the TAE/MgCl₂ buffer and loaded to the SAXS flow cells. The corresponded buffers were used as a reference and were subtracted from the samples. Scattering data of Octa and protein/Octa lattices were collected at the Complex Materials Scattering (CMS, 11-BM) beamline at the NSLS-II at BNL. The samples (typically 30 nM) were loaded into quartz capillary tubes and probed at the bottom of the capillary where samples precipitated. The 2D scattering images were converted into 1D scattering intensity

profiles through azimuthal integration. All 1D data were subtracted to scattering intensity from the pure buffer before analysis.

SAXS modeling. SAXS modeling was primarily performed using the ScatterSim software package^{61,66}, a python library for simulating 1D curves for the clusters and superlattices built from arbitrary anisotropic nanoscale objects. Detailed instrumentation, operation, and modeling are provided in the Supplementary Information.

Cryogenic electron microscopy (cryo-EM)

Sample preparation and imaging. Ultrathin carbon (<3 nm) grids on lacey carbon support films (Ted Pella, Inc. #01824) were treated for 30 s in Fischione Nanoclean 1070 (70% power) with a mixture of Argon (75%) and Oxygen (25%). Cryo-EM samples were prepared in Vitrobot (Mark IV) at 19 °C (Octa) or 4 °C (apoferritin/Octa) with settings: relative humidity 100%, wait time 180 s, blot time 2 s, and blot force 4. Octa or apoferritin/Octa (3 µL) solution was incubated with the glow-discharged grids, blotted with filter paper, and then plunged into liquid ethane pre-cooled by liquid nitrogen. Prior to imaging, samples were transferred to a Gatan 626 cryo-specimen holder in liquid nitrogen and then inserted into the microscope. The specimen temperature was maintained at -170 °C during data collection. Cryo-EM imaging was performed on a Titan Halo TEM operating at 300 kV. Movies were recorded in the low-dose mode at ×28,500 magnifications on a Gatan K2 (1.15 Å/pix, 10 e⁻/Å²/s, 0.2 s/frame, 6 s total) or K3 (1.055 Å/pix, 20 e⁻/Å²/s, 0.05 s/frame, 3 s total) camera. All movies were saved in tif-compressed mode with dark gain correction only.

Image processing and 3D reconstruction. All data processing and reconstruction were performed in RELION^{70,71}, including motion correction, CTF estimation, particle picking. All image processing and 3D reconstruction were done on a 4-GPU Exact Linux workstation or a 2-GPU Dell Linux workstation. 3D density map was displayed and manipulated in the UCSF Chimera package (10). We note that Octa using a single-stranded DNA scaffold to connect adjacent edges (six-helix bundle) might potentially contribute to the flexibility of the structure at each vertex. Such flexibility may affect or eliminate the octahedral symmetry and might result in a slightly off-centered position of apoferritin inside Octa, as shown in the reference-free 2D class images (Fig. 2g). Thus, we imposed no symmetry (C1 symmetry) throughout the entire data processing and 3D reconstruction. Detailed analyses and reconstruction procedures are provided in the Supplementary Information.

Cryo-electron tomography (cryo-ET)

Sample preparation and imaging. Cryo-ET samples of single- and double-layered Octa and protein/Octa lattices were prepared on lacey carbon film grids (Cu-200LC, Electron Microscopy Sciences, and Cu-200LN, Pacific Grid-Tech) using the Leica EM GP plunge freezer (Leica, Inc.) at 90% humidity and 4 °C. In brief, lattice solutions (4 µL) were incubated with glow-discharged grids and rapidly plunged into liquid ethane after blotting. Samples were screened by Zeiss Libra 120 Plus TEM (Carl Zeiss SMT GmbH) with in-column energy filter and a 4 k × 4 k Gatan UltraScan 4000 CCD camera, and operating at 120 kV and a low-dose condition. High-resolution tilt series were acquired by a Titan Krios G2 TEM (ThermoFisher Scientific) with a Gatan energy filter (Gatan, Inc.), operating at 300 kV. Micrographs were recorded on a Gatan K3 direct electron detector operated in super-resolution mode at a nominal magnification of 53 K (1.46 Å/pixel) with defocus -3 µm using SerialEM⁷². Non-tilt micrographs were acquired with 3.0 s exposure time, 0.15 s each frame, at a dose rate of ~8 e⁻/Å²/s. Tilt series were collected from -51° to +51° at a 3° increment, starting at +21°, with 1.0 s exposure time, 0.15 s each frame, at a dose rate of ~8 e⁻/Å²/s.

Image processing and 3D reconstruction. Anisotropic image motion of each frame of image stack in super-resolution mode (0.73 Å/pixel) was corrected by MotionCor2⁷³. All tilt series were binned by two times (1.46 Å/pixel) and aligned by IMOD⁷⁴. 3D density maps of the whole micrograph were aligned and reconstructed by IMOD, after the tilt series were binned eight times (11.68 Å/pixel). For high-resolution 3D structure, a tilt series of a focused area with ~336 × 336 nm², i.e. 288 pixel × 11.68 Å/pixel, was windowed and extracted from the tilt series following the IPET reconstruction protocol⁶⁵. All 3D maps were low-pass filtered to 80 Å using ENAN software⁷⁵ and displayed in the UCSF Chimera package⁷⁶. Detailed analyses and reconstruction procedures are provided in the Supplementary Information.

Data availability

The data supporting the findings of this study are available within this article and its Supplementary Information or from the corresponding author upon reasonable request. The Supplementary Information includes materials, supplementary figures, and detailed experimental methods, including gel electrophoresis, dynamic light scattering, ferrozine assay, cryo-EM imaging, single-particle reconstruction, individual particle electron tomography, small-angle X-ray scattering, and modeling.

Code availability

The scripts used in SAXS analysis and modeling are included in the ScatterSim software package (<https://github.com/CFN-softbio/ScatterSim>), a Python package available for download through GitHub or from the corresponding author upon reasonable request.

Received: 23 January 2021; Accepted: 13 May 2021;

Published online: 17 June 2021

References

- Hamley, I. W. Protein assemblies: nature-inspired and designed nanostructures. *Biomacromolecules* **20**, 1829–1848 (2019).
- Korpi, A., Anaya-Plaza, E., Välimäki, S. & Kostiaainen, M. Highly ordered protein cage assemblies: A toolkit for new materials. *WIREs Nanomed. Nanobiotechnol.* **12**, e1578–e1578 (2020).
- Yang, G., Wu, L., Chen, G. & Jiang, M. Precise protein assembly of array structures. *Chem. Commun.* **52**, 10595–10605 (2016).
- Churchfield, L. A. & Tezcan, F. A. Design and construction of functional supramolecular metalloprotein assemblies. *Acc. Chem. Res.* **52**, 345–355 (2019).
- Dale, G. E., Oefner, C. & D'Arcy, A. The protein as a variable in protein crystallization. *J. Struct. Biol.* **142**, 88–97 (2003).
- Shaw, A. et al. Binding to nanopatterned antigens is dominated by the spatial tolerance of antibodies. *Nat. Nanotechnol.* **14**, 184–190 (2019).
- Levy, E. D., Erba, E. B., Robinson, C. V. & Teichmann, S. A. Assembly reflects evolution of protein complexes. *Nature* **453**, 1262–1265 (2008).
- Chiesa, G., Kiriakov, S. & Khalil, A. S. Protein assembly systems in natural and synthetic biology. *BMC Biol.* **18**, 35–35 (2020).
- Reed, E. H., Schuster, B. S., Good, M. C. & Hammer, D. A. SPLIT: stable protein coacervation using a light induced transition. *ACS Synth. Biol.* **9**, 500–507 (2020).
- Nikolova, M. P. & Chavali, M. S. Recent advances in biomaterials for 3D scaffolds: a review. *Bioact. Mater.* **4**, 271–292 (2019).
- Sharma, K., Mujawar, M. A. & Kaushik, A. State-of-art functional biomaterials for tissue engineering. *Front. Mater.* **6**, 172–172 (2019).
- Wilner, O. I. et al. Enzyme cascades activated on topologically programmed DNA scaffolds. *Nat. Nanotechnol.* **4**, 249–254 (2009).
- Ellis, G. A. et al. Artificial multienzyme scaffolds: pursuing in vitro substrate channeling with an overview of current progress. *ACS Catal.* **9**, 10812–10869 (2019).
- Mitchell, P. A perspective on protein microarrays. *Nat. Biotechnol.* **20**, 225–229 (2002).
- Polka, J. K., Hays, S. G. & Silver, P. A. Building spatial synthetic biology with compartments, scaffolds, and communities. *Cold Spring Harb. Perspect. Biol.* **8**, a024018 (2016).
- Pyles, H., Zhang, S., De Yoreo, J. J. & Baker, D. Controlling protein assembly on inorganic crystals through designed protein interfaces. *Nature* **571**, 251–256 (2019).
- Sinclair, J. C., Davies, K. M., Vénien-Bryan, C. & Noble, M. E. M. Generation of protein lattices by fusing proteins with matching rotational symmetry. *Nat. Nanotechnol.* **6**, 558–562 (2011).
- Suzuki, Y. et al. Self-assembly of coherently dynamic, auxetic, two-dimensional protein crystals. *Nature* **533**, 369–373 (2016).
- Lai, Y.-T. et al. Structure of a designed protein cage that self-assembles into a highly porous cube. *Nat. Chem.* **6**, 1065–1071 (2014).
- Korpi, A. et al. Self-assembly of electrostatic cocrystals from supercharged fusion peptides and protein cages. *ACS Macro Lett.* **7**, 318–323 (2018).
- Seeman, N. C. Nucleic acid junctions and lattices. *J. Theor. Biol.* **99**, 237–247 (1982).
- Chen, J. & Seeman, N. C. Synthesis from DNA of a molecule with the connectivity of a cube. *Nature* **350**, 631–633 (1991).
- Rothmund, P. W. K. & Folding, D. N. A. to create nanoscale shapes and patterns. *Nature* **440**, 297–297 (2006).
- Tian, C. et al. Directed self-assembly of DNA tiles into complex nanocages. *Angew. Chem. Int. Ed.* **53**, 8041–8044 (2014).
- Benson, E. et al. DNA rendering of polyhedral meshes at the nanoscale. *Nature* **523**, 441–441 (2015).
- Douglas, S. M. et al. Self-assembly of DNA into nanoscale three-dimensional shapes. *Nature* **459**, 414–414 (2009).
- Wagenbauer, K. F., Sigl, C. & Dietz, H. Gigadalton-scale shape-programmable DNA assemblies. *Nature* **552**, 78–83 (2017).
- Monferrer, A., Zhang, D., Lushnikov, A. J. & Hermann, T. Versatile kit of robust nanoshapes self-assembling from RNA and DNA modules. *Nat. Commun.* **10**, 608 (2019).

29. Liu, W., Halverson, J., Tian, Y., Tkachenko, A. V. & Gang, O. Self-organized architectures from assorted DNA-framed nanoparticles. *Nat. Chem.* **8**, 867–873 (2016).
30. Liu, W., Zhong, H., Wang, R. & Seeman, N. C. Crystalline two-dimensional DNA-origami arrays. *Angew. Chem. Int. Ed.* **50**, 264–267 (2011).
31. Winfree, E., Liu, F., Wenzler, L. A. & Seeman, N. C. Design and self-assembly of two-dimensional DNA crystals. *Nature* **394**, 539–544 (1998).
32. Zheng, J. et al. From molecular to macroscopic via the rational design of a self-assembled 3D DNA crystal. *Nature* **461**, 74–77 (2009).
33. Tian, Y. et al. Ordered three-dimensional nanomaterials using DNA-prescribed and valence-controlled material voxels. *Nat. Mater.* **19**, 789–796 (2020).
34. Hong, F. et al. Layered-crossover tiles with precisely tunable angles for 2D and 3D DNA crystal engineering. *J. Am. Chem. Soc.* **140**, 14670–14676 (2018).
35. Simmons, C. R. et al. Tuning the cavity size and chirality of self-assembling 3D DNA crystals. *J. Am. Chem. Soc.* **139**, 11254–11260 (2017).
36. Zhang, T. et al. 3D DNA origami crystals. *Adv. Mater.* **30**, 1800273–1800273 (2018).
37. Boerneke, M. A., Dibrov, S. M. & Hermann, T. Crystal-structure-guided design of self-assembling RNA nanotriangles. *Angew. Chem. Int. Ed.* **55**, 4097–4100 (2016).
38. Nykpanchuk, D., Maye, M. M., van der Lelie, D. & Gang, O. DNA-guided crystallization of colloidal nanoparticles. *Nature* **451**, 549–552 (2008).
39. Park, S. Y. et al. DNA-programmable nanoparticle crystallization. *Nature* **451**, 553–556 (2008).
40. Tian, Y. et al. Prescribed nanoparticle cluster architectures and low-dimensional arrays built using octahedral DNA origami frames. *Nat. Nanotechnol.* **10**, 637–637 (2015).
41. Macfarlane, R. J. et al. Nanoparticle superlattice engineering with DNA. *Science* **334**, 204–208 (2011).
42. Tian, Y. et al. Lattice engineering through nanoparticle–DNA frameworks. *Nat. Mater.* **15**, 654–654 (2016).
43. Liu, W. Y. et al. Diamond family of nanoparticle superlattices. *Science* **351**, 582–586 (2016).
44. Sun, S. et al. Valence-programmable nanoparticle architectures. *Nat. Commun.* **11**, 2279–2279 (2020).
45. Fu, J., Liu, M., Liu, Y., Woodbury, N. W. & Yan, H. Interenzyme substrate diffusion for an enzyme cascade organized on spatially addressable DNA nanostructures. *J. Am. Chem. Soc.* **134**, 5516–5519 (2012).
46. Ke, G. et al. Directional regulation of enzyme pathways through the control of substrate channeling on a DNA origami scaffold. *Angew. Chem. Int. Ed.* **55**, 7483–7486 (2016).
47. Dobrovolskaia, M. A. & Bathe, M. Opportunities and challenges for the clinical translation of structured DNA assemblies as gene therapeutic delivery and vaccine vectors. *WIREs Nanomed. Nanobiotechnol.* e1657, <https://doi.org/10.1002/wnan.1657> (2020).
48. Wang, S.-T. et al. DNA origami protection and molecular interfacing through engineered sequence-defined peptides. *Proc. Natl Acad. Sci. USA* **117**, 6339–6348 (2020).
49. Ke, W. et al. RNA–DNA fibers and polygons with controlled immunorecognition activate RNAi, FRET and transcriptional regulation of NF- κ B in human cells. *Nucleic Acids Res.* **47**, 1350–1361 (2019).
50. Zhao, Y.-X. et al. DNA origami delivery system for cancer therapy with tunable release properties. *ACS Nano* **6**, 8684–8691 (2012).
51. Bastings, M. M. C. et al. Modulation of the cellular uptake of DNA origami through control over mass and shape. *Nano Lett.* **18**, 3557–3564 (2018).
52. Aksel, T., Yu, Z., Cheng, Y. & Douglas, S. M. Molecular goniometers for single-particle cryo-electron microscopy of DNA-binding proteins. *Nat. Biotechnol.* <https://doi.org/10.1038/s41587-020-0716-8> (2020).
53. Martin, T. G. et al. Design of a molecular support for cryo-EM structure determination. *Proc. Natl Acad. Sci. USA* **113**, E7456 (2016).
54. Veneziano, R. et al. Role of nanoscale antigen organization on B-cell activation probed using DNA origami. *Nat. Nanotechnol.* **15**, 716–723 (2020).
55. Funke, J. J. et al. Uncovering the forces between nucleosomes using DNA origami. *Sci. Adv.* **2**, e1600974 (2016).
56. Zhou, K., Ke, Y. & Wang, Q. Selective in situ assembly of viral protein onto DNA origami. *J. Am. Chem. Soc.* **140**, 8074–8077 (2018).
57. Brodin, J. D., Auyeung, E. & Mirkin, C. A. DNA-mediated engineering of multicomponent enzyme crystals. *Proc. Natl Acad. Sci. USA* **112**, 4564–4569 (2015).
58. Kim, M. et al. pH-dependent structures of ferritin and apoferritin in solution: disassembly and reassembly. *Biomacromolecules* **12**, 1629–1640 (2011).
59. Granier, T., Gallois, B., Dautant, A., Langlois d'Estaintot, B. & Précigoux, G. Comparison of the structures of the cubic and tetragonal forms of horse-spleen apoferritin. *Acta Crystallogr. Sect. D* **53**, 580–587 (1997).
60. Zhao, Z. et al. Nanocaged enzymes with enhanced catalytic activity and increased stability against protease digestion. *Nat. Commun.* **7**, 10619 (2016).
61. Yager, K. G., Zhang, Y., Lu, F. & Gang, O. Periodic lattices of arbitrary nano-objects: modeling and applications for self-assembled systems. *J. Appl. Crystallogr.* **47**, 118–129 (2014).
62. Lin, Z. et al. Engineering organization of DNA nano-chambers through dimensionally controlled and multi-sequence encoded differentiated bonds. *J. Am. Chem. Soc.* **142**, 17531–17542 (2020).
63. Lei, D. et al. Three-dimensional structural dynamics of DNA origami Bennett linkages using individual-particle electron tomography. *Nat. Commun.* **9**, 592–592 (2018).
64. Zhai, X. et al. LoTToR: an algorithm for missing-wedge correction of the low-tilt tomographic 3D reconstruction of a single-molecule structure. *Sci. Rep.* **10**, 10489 (2020).
65. Zhang, L. & Ren, G. IPET and FETR: experimental approach for studying molecular structure dynamics by cryo-electron tomography of a single-molecule structure. *PLoS ONE* **7**, 1–19 (2012).
66. Yager, K. G. ScatterSim. <https://github.com/CFN-softbio/ScatterSim> (2017).
67. Honarmand Ebrahimi, K., Hagedoorn, P.-L. & Hagen, W. R. Unity in the biochemistry of the iron-storage proteins ferritin and bacterioferritin. *Chem. Rev.* **115**, 295–326 (2015).
68. Pan, Y.-H. et al. 3D morphology of the human hepatic ferritin mineral core: New evidence for a subunit structure revealed by single particle analysis of HAADF-STEM images. *J. Struct. Biol.* **166**, 22–31 (2009).
69. Harrison, P. M., Hoy, T. G., Macara, I. G. & Hoare, R. J. Ferritin iron uptake and release. Structure–function relationships. *Biochem. J.* **143**, 445–451 (1974).
70. Zivanov, J. et al. New tools for automated high-resolution cryo-EM structure determination in RELION-3. *Elife* **7**, <https://doi.org/10.7554/eLife.42166> (2018).
71. Scheres, S. H. W. RELION: Implementation of a Bayesian approach to cryo-EM structure determination. *J. Struct. Biol.* **180**, 519–530 (2012).
72. Mastronarde, D. N. SerialEM: a program for automated tilt series acquisition on tecnai microscopes using prediction of specimen position. *Microsc. Microanal.* **9**, 1182–1183 (2003).
73. Zheng, S. Q. et al. MotionCor2: anisotropic correction of beam-induced motion for improved cryo-electron microscopy. *Nat. Methods* **14**, 331–332 (2017).
74. Kremer, J. R., Mastronarde, D. N. & McIntosh, J. R. Computer visualization of three-dimensional image data using IMOD. *J. Struct. Biol.* **116**, 71–76 (1996).
75. Ludtke, S. J., Baldwin, P. R. & Chiu, W. EMAN: semiautomated software for high-resolution single-particle reconstructions. *J. Struct. Biol.* **128**, 82–97 (1999).
76. Pettersen, E. F. et al. UCSF Chimera—a visualization system for exploratory research and analysis. *J. Comput. Chem.* **25**, 1605–1612 (2004).

Acknowledgements

We thank the support from the Center for Functional Nanomaterials at BNL, the Molecular Foundry at LBL, the BNL Laboratory Directed Research and Development grant, and the Office of Science, Office of Basic Energy Sciences, of the U.S. Department of Energy under Contracts No. DE-SC0012704 and No. DE-AC02-05CH11231. LiX beamline is part of the Life Science Biomedical Technology Research resource, co-funded by the National Institute of General Medical Sciences (NIGMS) under grant P41 GM111244 and by the DOE Office of Biological and Environmental Research under grant KP1605010, with additional support from NIH under grant S10 OD012331. G.R. and J.L. are partially supported by the NIH NHLBI (R01HL115153), NIDDK (R01DK042667) and NIMH (R01MH077303). The operation of NSLS-II is supported by U.S. Department of Energy, Office of Basic Energy Sciences, under contract No. DE-SC0012704. O.G. and B.M. are partially supported by the National Science Foundation under Grant No 1905920 and by the US Department of Energy, Office of Basic Energy Sciences, Grant DE-SC0008772.

Author contributions

S.-T.W. and O.G. conceived and designed the experiments. S.-T.W. performed protein modification, origami preparation, and the assembly experiments. S.-T.W. performed gel electrophoresis, DLS, negative-stained EM imaging, and SAXS experiments of the protein encapsulated origamis and the assembled lattice. B.M. and H.Z. contributed to computational modeling and fitting of the SAXS data. B.M., H.Z., D.M., J.B., and L.B. helped with SAXS experiments. J.L. and G.R. contributed to cryo-ET imaging and tomography 3D reconstruction. T.W. contributed to cryo-EM imaging and single-particle reconstruction. W.L. and Q.L. helped with protein selection, modification, and characterization. S.-T.W. and O.G. wrote the paper. O.G. supervised the project. All authors discussed the results and commented on the manuscript.

Competing interests

The authors declare no competing interests.

Additional information

Supplementary information The online version contains supplementary material available at <https://doi.org/10.1038/s41467-021-23966-4>.

Correspondence and requests for materials should be addressed to O.G.

Peer review information *Nature Communications* thanks the anonymous reviewers for their contribution to the peer review of this work.

Reprints and permission information is available at <http://www.nature.com/reprints>

Publisher's note Springer Nature remains neutral with regard to jurisdictional claims in published maps and institutional affiliations.



Open Access This article is licensed under a Creative Commons Attribution 4.0 International License, which permits use, sharing, adaptation, distribution and reproduction in any medium or format, as long as you give appropriate credit to the original author(s) and the source, provide a link to the Creative Commons license, and indicate if changes were made. The images or other third party material in this article are included in the article's Creative Commons license, unless indicated otherwise in a credit line to the material. If material is not included in the article's Creative Commons license and your intended use is not permitted by statutory regulation or exceeds the permitted use, you will need to obtain permission directly from the copyright holder. To view a copy of this license, visit <http://creativecommons.org/licenses/by/4.0/>.

© The Author(s) 2021

Supplementary Information

Designed and Biologically Active Protein Lattices

Shih-Ting Wang¹, Brian Minevich², Jianfang Liu³, Honghu Zhang¹, Dmytro Nykypanchuk¹, James Byrnes⁴, Wu Liu⁵, Lev Bershadsky¹, Qun Liu⁵, Tong Wang⁶, Gang Ren³ and Oleg Gang^{1,2,7*}

¹Center for Functional Nanomaterials, Brookhaven National Laboratory, Brookhaven Avenue, Upton, New York, 11973, United States

²Department of Chemical Engineering, Columbia University, New York City, New York, 10027, United States

³The Molecular Foundry, Lawrence Berkeley National Laboratory, 1 Cyclotron Road, Berkeley, California, 94720, United States

⁴Energy Sciences Directorate/Photon Science Division, NSLS II, Brookhaven National Laboratory, Upton, New York, 11973, United States

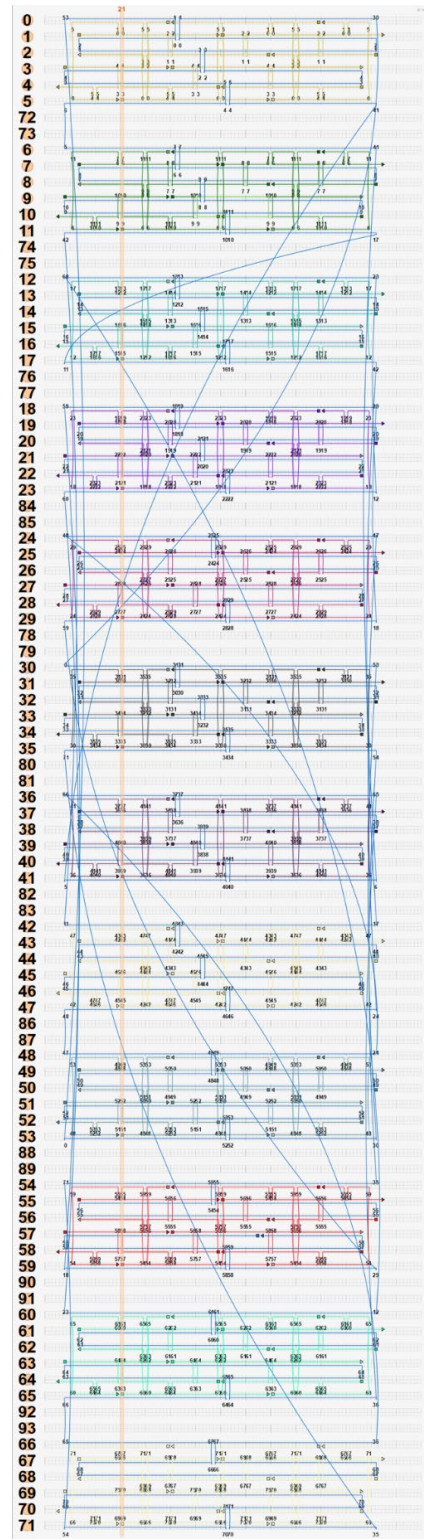
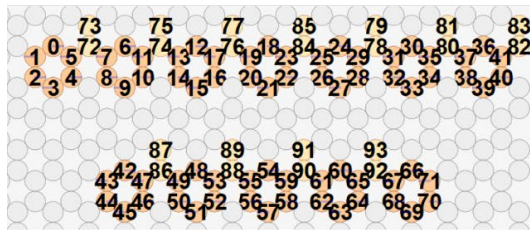
⁵Biology Department, Brookhaven National Laboratory, Bell Avenue, Upton, New York, 11973, United States

⁶Advanced Science Research Center at the Graduate Center of the City University of New York, New York City, New York, 10031, United States

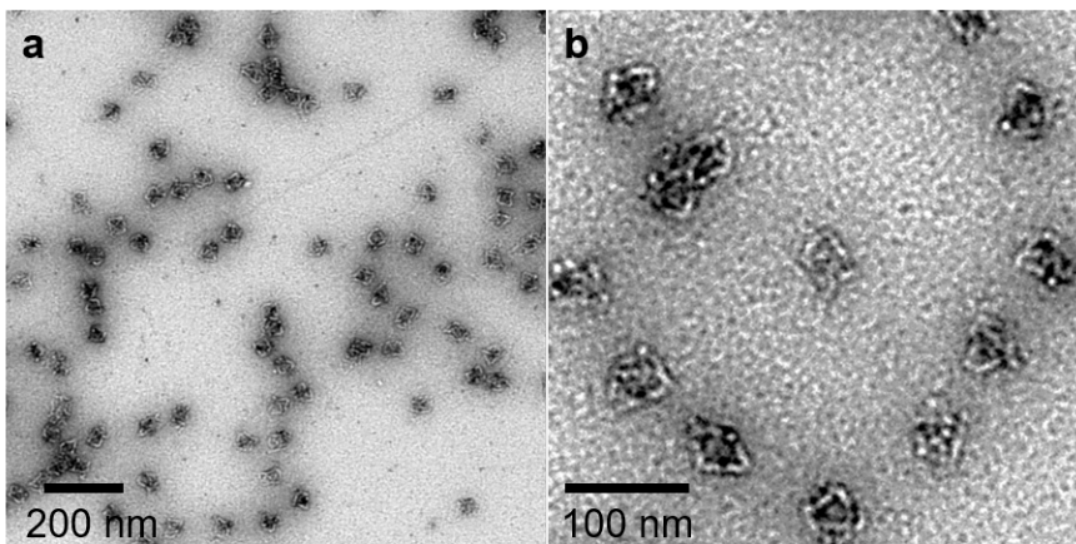
⁷Department of Applied Physics and Applied Mathematics, Columbia University, New York, NY, 10027, United States

**E-mail: og2226@columbia.edu*

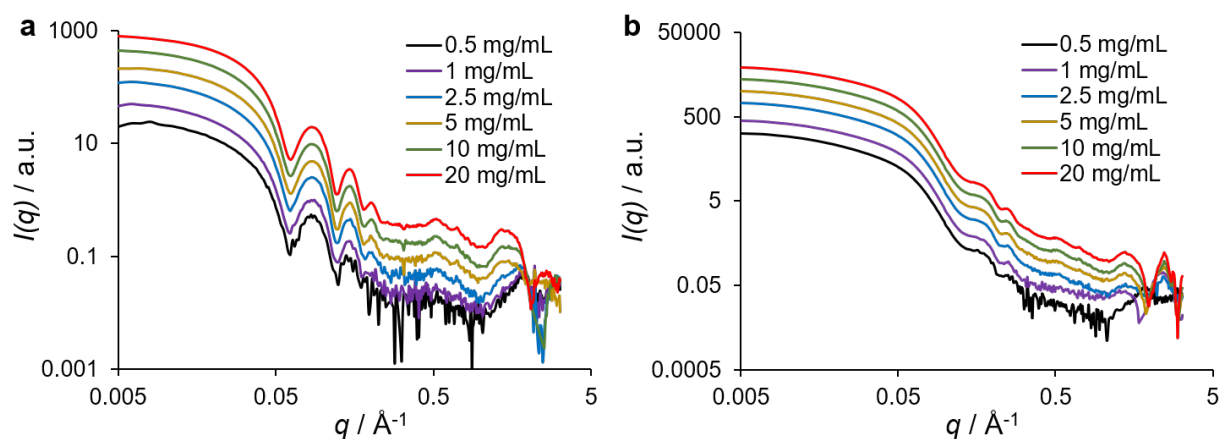
Supplementary Figures



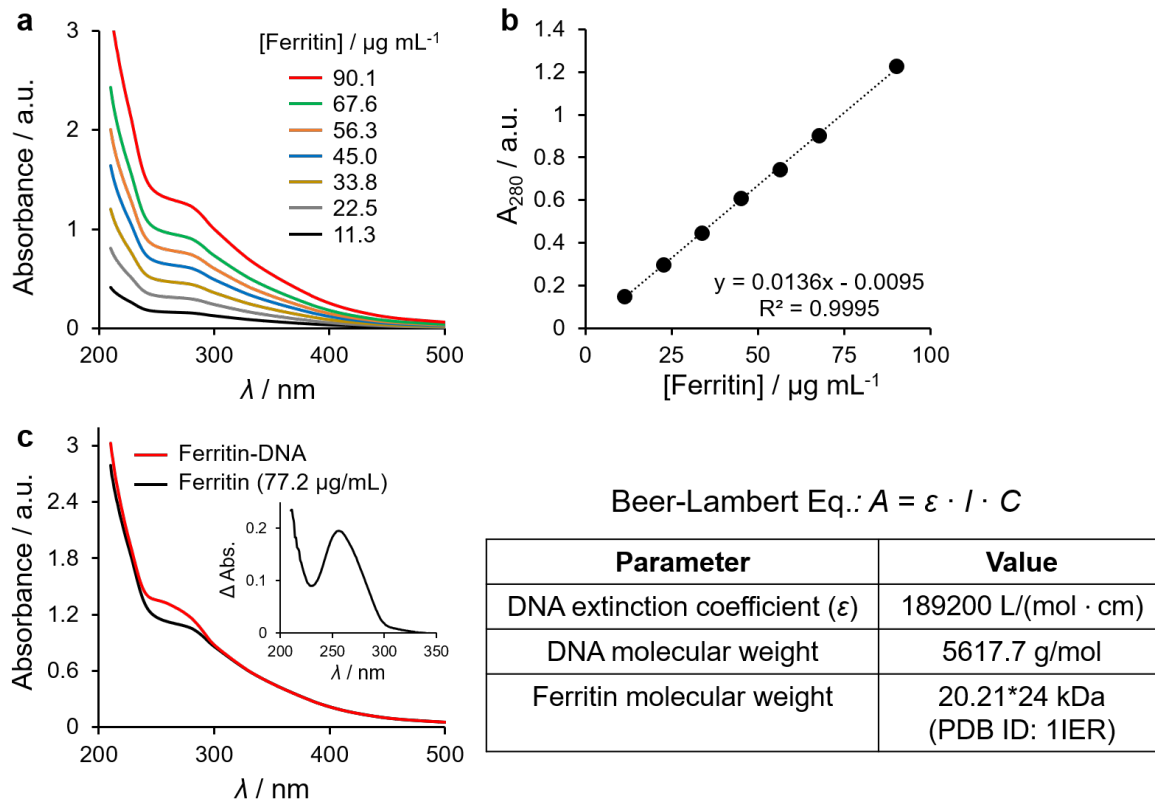
Supplementary Figure 1. Octa design in caDNAno (<https://cadnano.org>). Octa sequences are provided in Supplementary Data 1. The DNA sequences added to Octa for generating 2D and 3D lattices are provided in Supplementary Data 2 and 3, respectively.



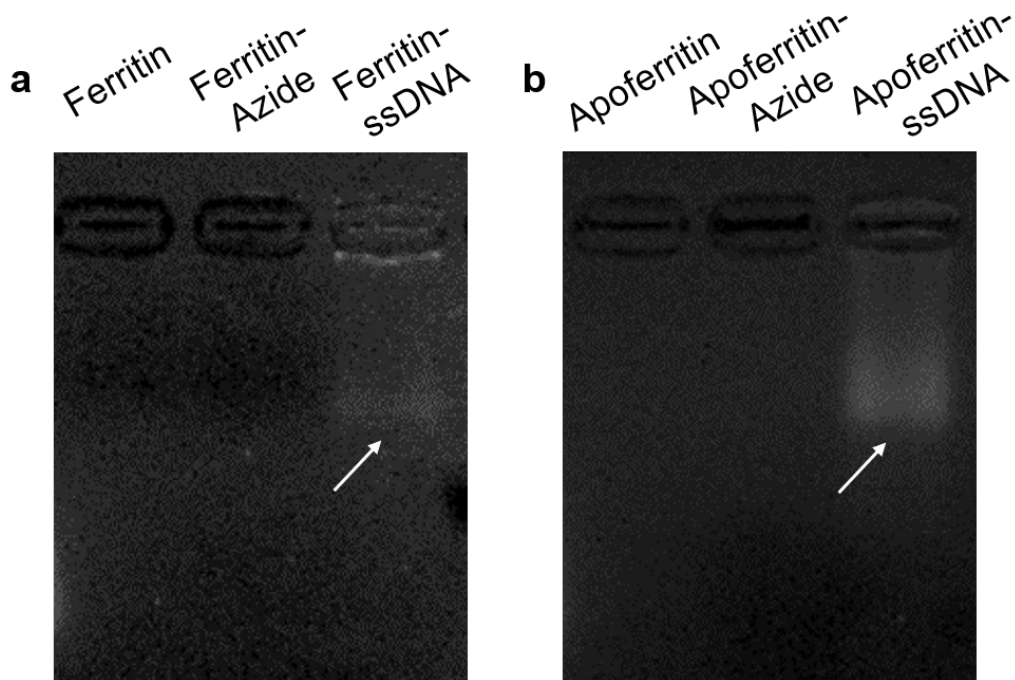
Supplementary Figure 2. Negative-stained TEM images of the octahedral DNA origami (Octa). b is a magnified image of the Octa structure.



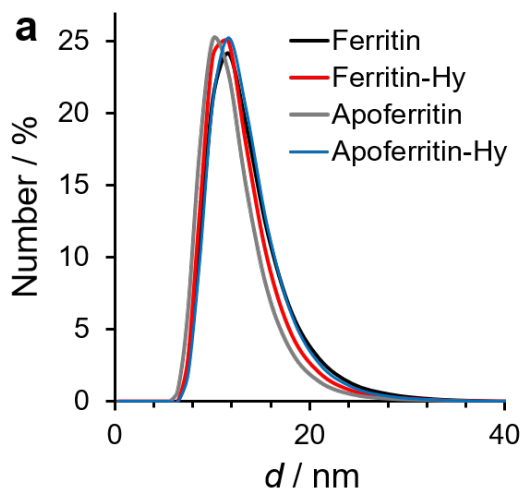
Supplementary Figure 3. SAXS intensity profiles of different concentrations of a, apoferritin and b, ferritin in PBS buffer.



Supplementary Figure 4. UV-vis quantification of protein concentration and ssDNA grafting on protein surfaces. In a and b, UV-vis spectra of a range of known ferritin concentrations in PBS were measured where the absorbance at 280 nm (A_{280}) exhibited a linear relation. The standard spectra (example in c) were compared with those of ferritin-DNA and to obtain the absorption of ssDNA at 260 nm by subtraction. Using the Beer-Lambert equation and the known parameters, about 6–7 ssDNA per ferritin was estimated based on three independent measurements.



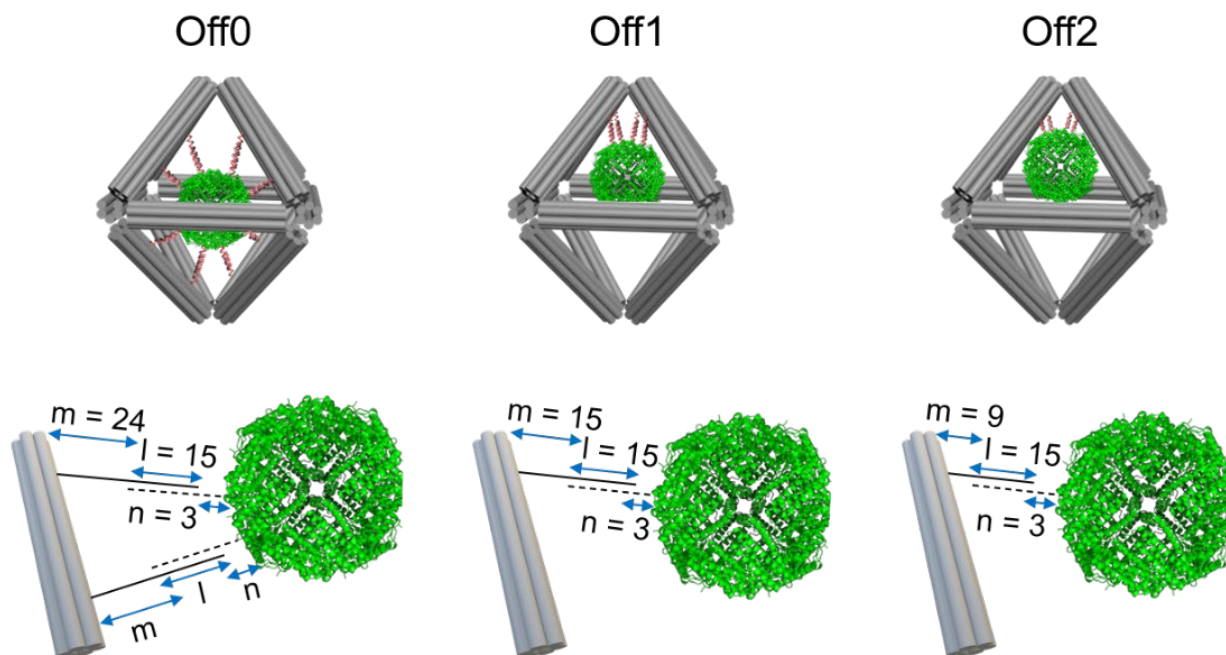
Supplementary Figure 5. AGE analyses of the two-step modification of a, ferritin and b, apoferritin. Protein surfaces were first activated with azide through the NHS-amine reaction and followed by conjugation of the DBCO-modified ssDNA *via* click chemistry. The white arrows pointed out the bands of the ssDNA-modified proteins. AGE was performed with 4 wt% agarose (medium EEO) at 80 V.



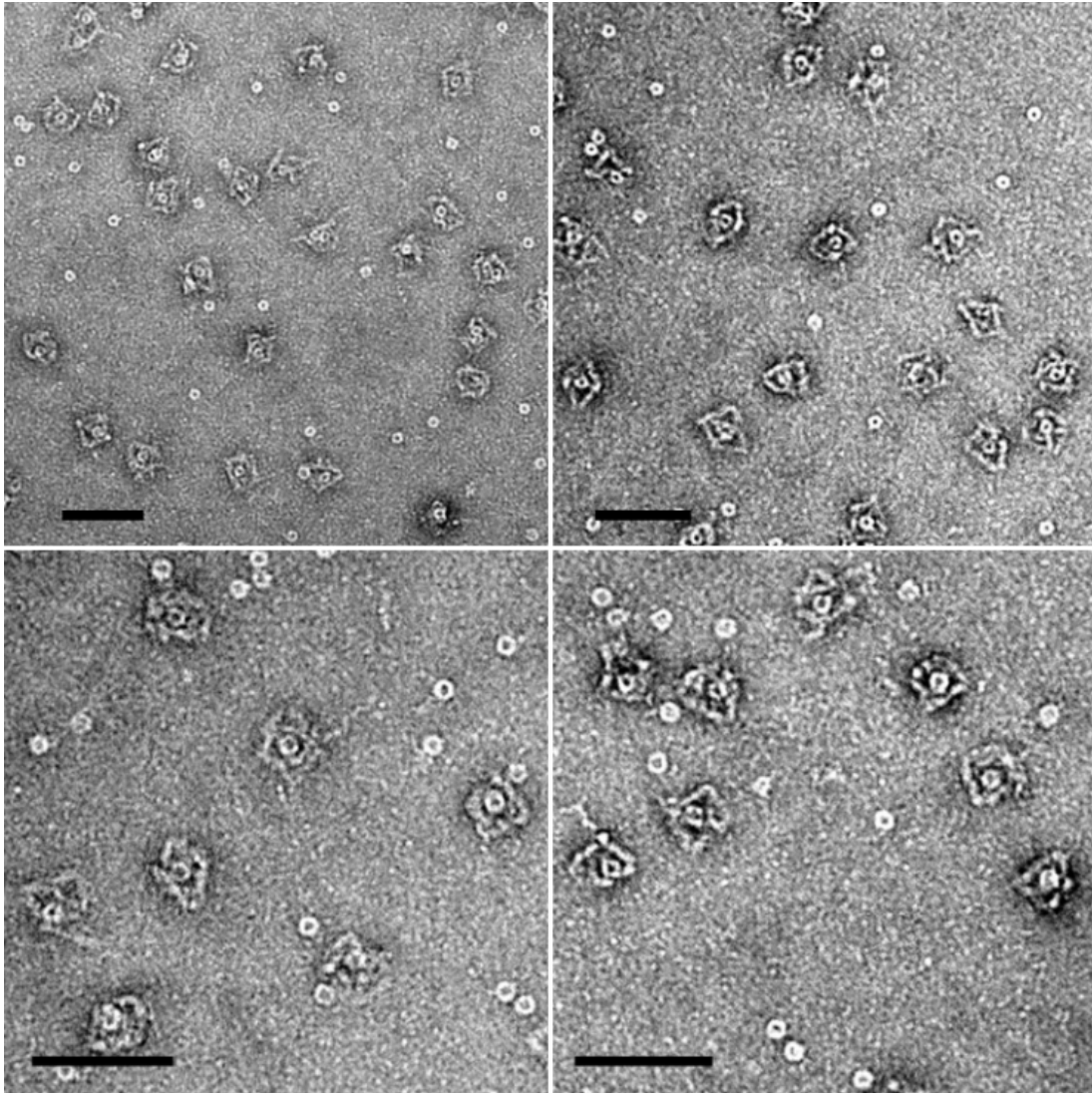
b

Sample	d (avg.) / nm
Ferritin	12.7 ± 0.7
Ferritin-Hy	12.2 ± 0.7
Apoferritin	11.5 ± 0.7
Apoferritin-Hy	12.7 ± 0.7

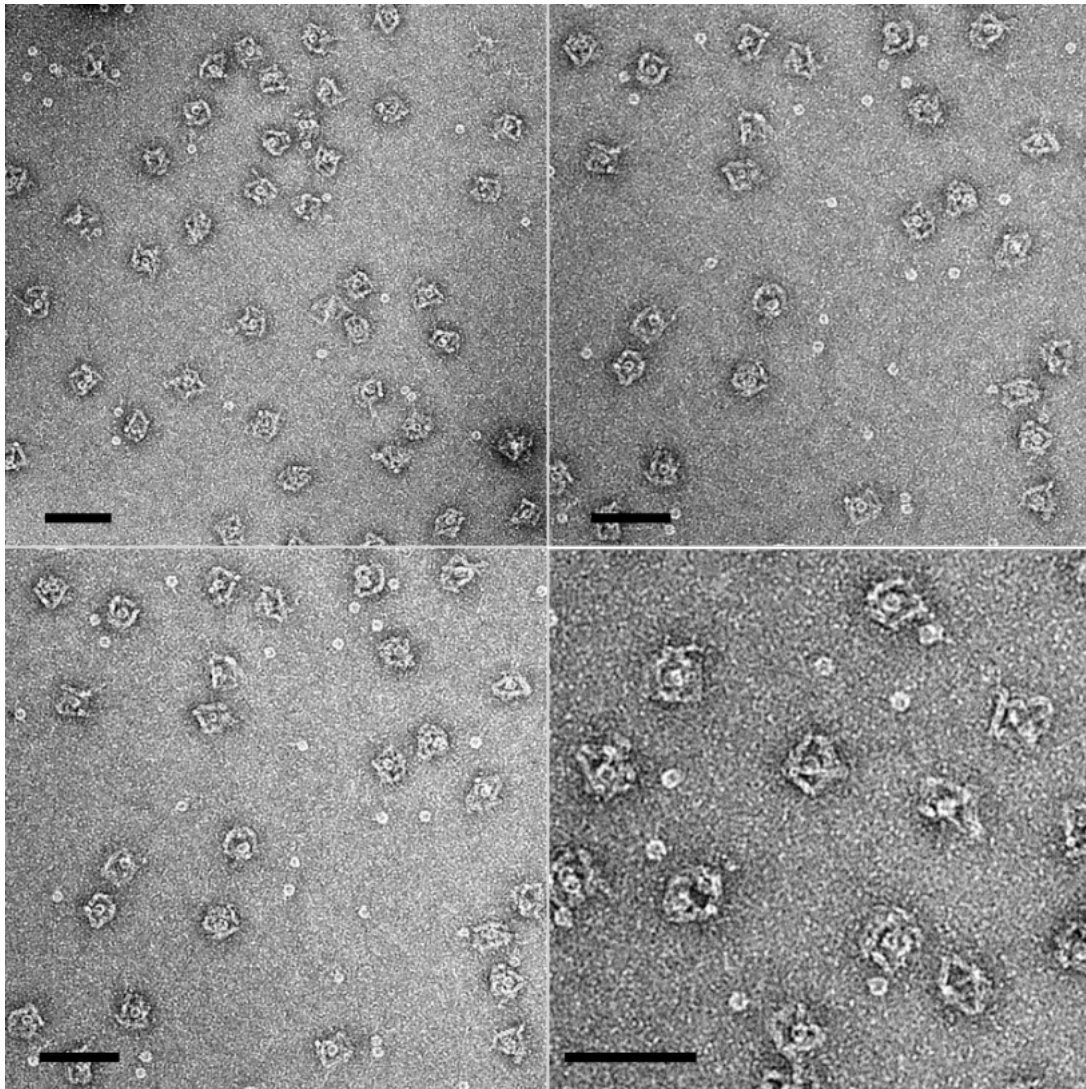
Supplementary Figure 6. a, DLS of ferritin, apoferritin and the ssDNA-modified proteins and b, a table showing the average sizes of the protein samples. The protein samples (100 nM) were diluted in PBS buffer and equilibrated for 120 s prior to measurement.



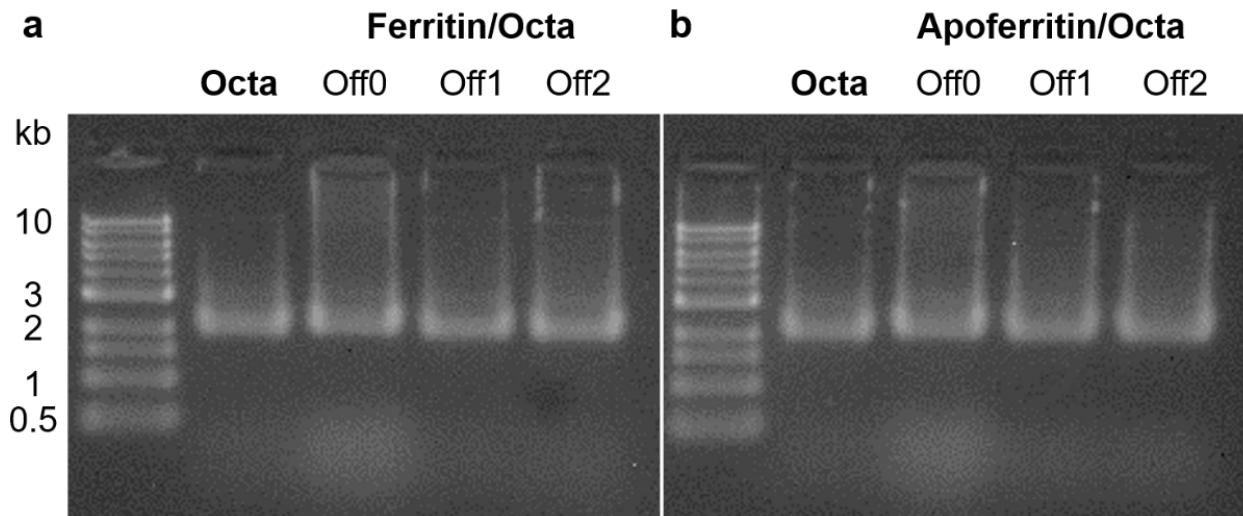
Supplementary Figure 7. Schematic view showing the lengths of DNA linking motifs used for protein encapsulation and to place the proteins (ferritin PDB ID: 1IER) at different positions inside the Octa structure. In the centered design (Off0), eight DNA linkers from the four select in-plane bundles were used; In the off-centered designs (Off1 and Off2), the four ssDNA linkers were extended from the same positions of the four select bundles converged at one vertex, and these strand positions (OC-staples-111 and 115, see Supplementary Data 1) were also used in Off0. m is the extended ssDNA from the bundle, n is the extended ssDNA from the protein, and l is the complementary bases that hybridize between the strands on Octa and protein.



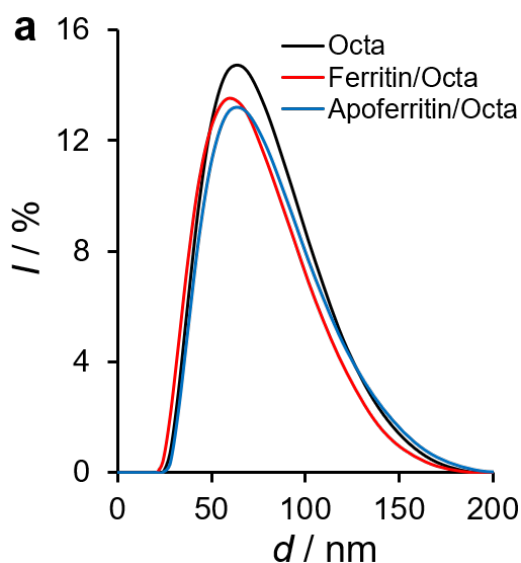
Supplementary Figure 8. Negative-stained TEM images of ferritin encapsulated inside Octa (scale bars: 100 nm).



Supplementary Figure 9. Negative-stained TEM images of apoferritin encapsulated inside Octa (scale bars: 100 nm).



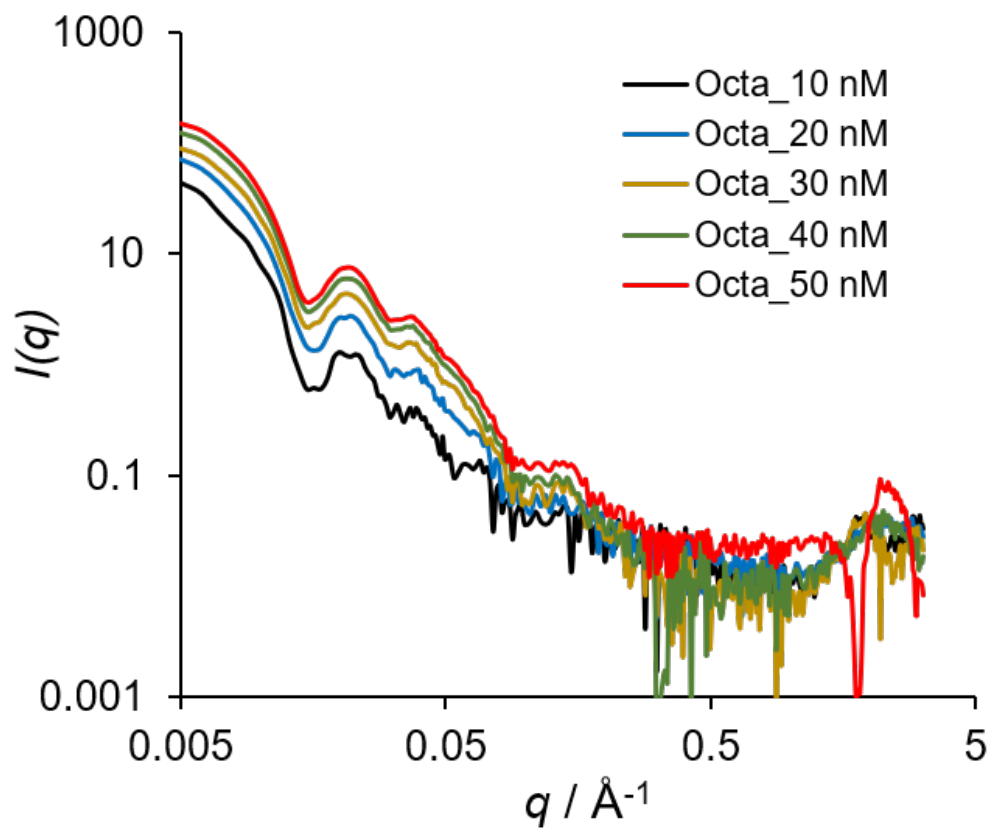
Supplementary Figure 10. AGE of a, ferritin/Octa (10 nM) and b, apoferritin/Octa (10 nM), where the encapsulated proteins were prescribed at different positions (center: Off0 and off-center: Off1 and Off2) inside the Octa structure. The small change of the electrophoretic mobility after protein encapsulation was likely due to the higher net charge and size of Octa compared to the proteins.



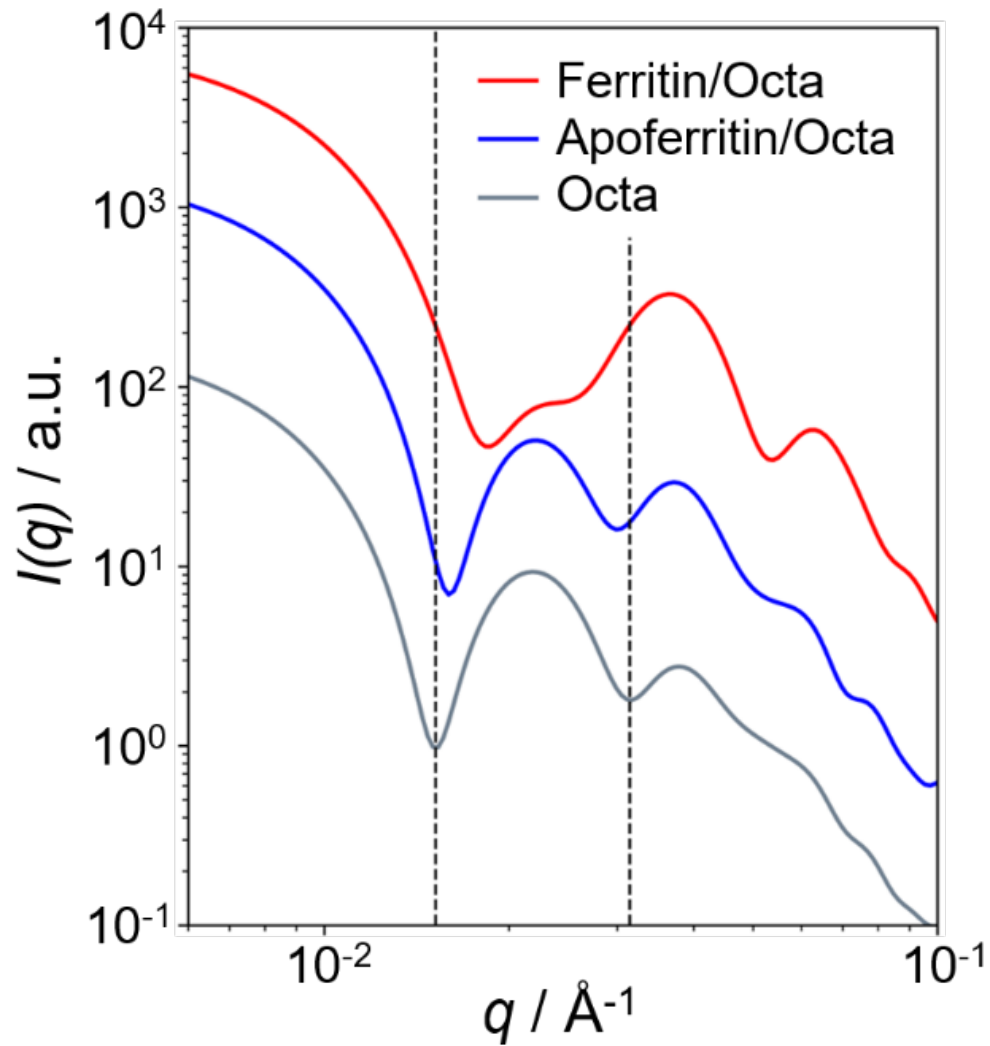
b

Sample	d (avg.) / nm
Octa	67.8 ± 5.3
Ferritin/Octa	60.3 ± 0.7
Apoferritin/Octa	75.2 ± 2.4

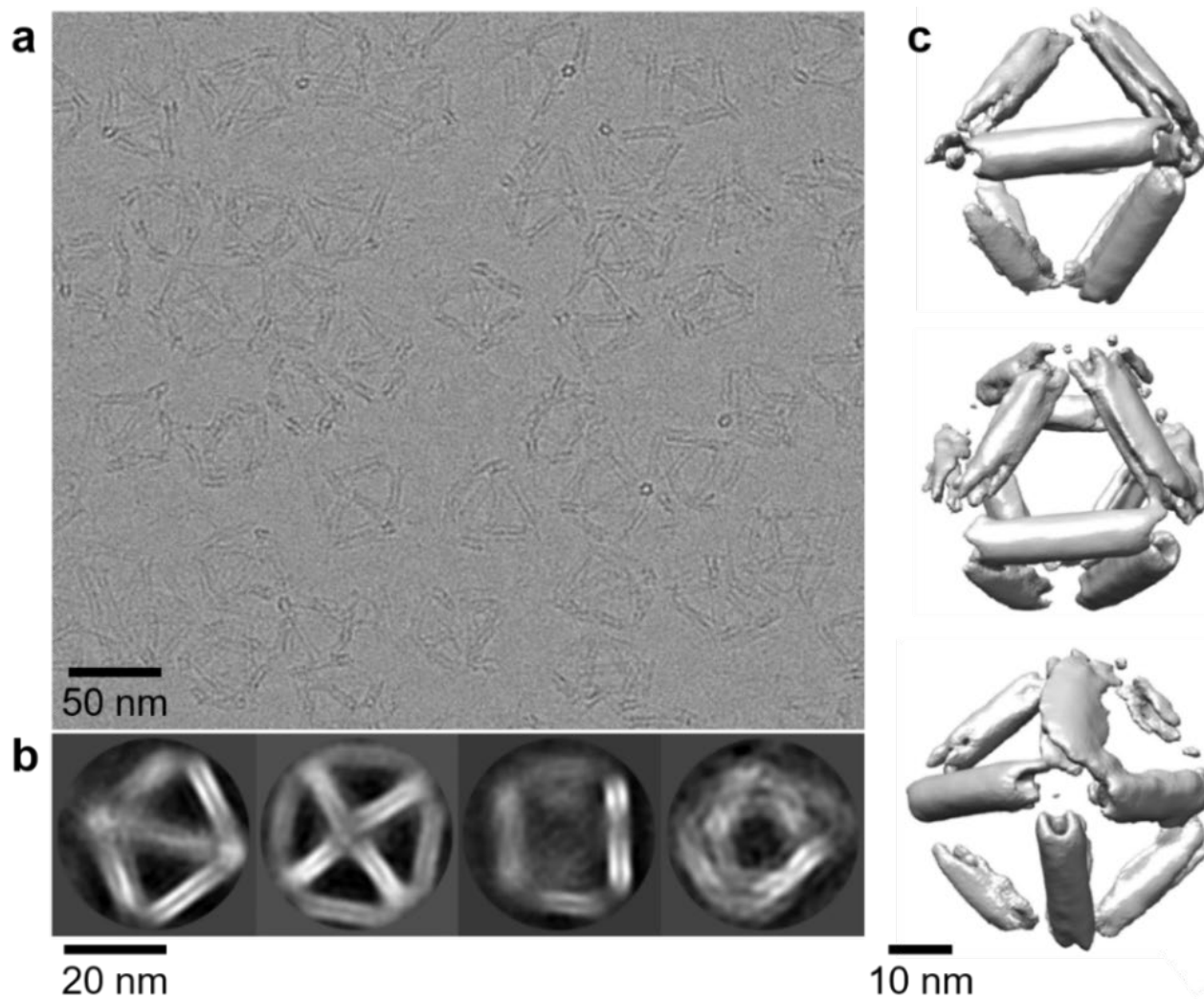
Supplementary Figure 11. a, DLS of Octa, ferritin/Octa and apoferritin/Octa, and b, a table showing the average sizes of the protein samples. The Octa samples were diluted to 5 nM in TAE (1X) buffer containing 12.5 mM MgCl₂ and equilibrated for 120 s prior to measurement.



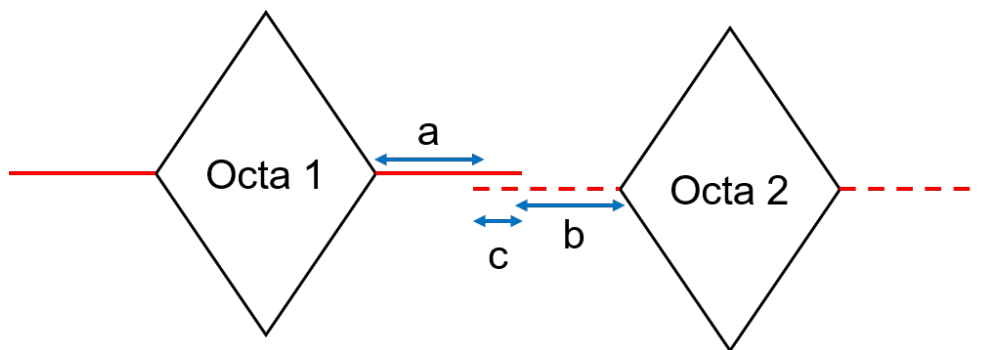
Supplementary Figure 12. SAXS intensity profiles of different concentrations of Octa in TAE (1X) buffer containing 12.5 mM MgCl_2 .



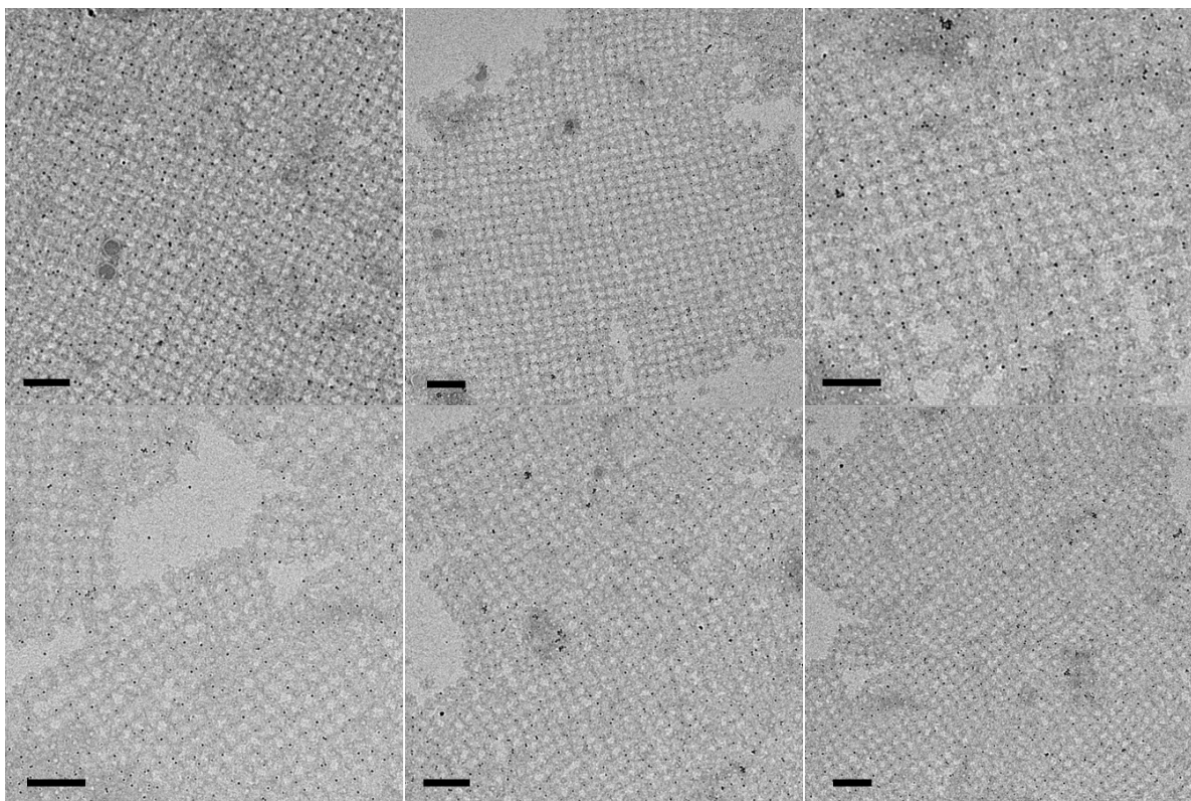
Supplementary Figure 13. SAXS analysis showing the simulated SAXS data of single empty Octa, ferritin/Octa and apoferritin/Octa, in which the scattering profiles showed a similar trend to the results obtained experimentally (Fig. 2f). In these simulated results, proteins were assumed to be 100% encapsulated inside Octa.



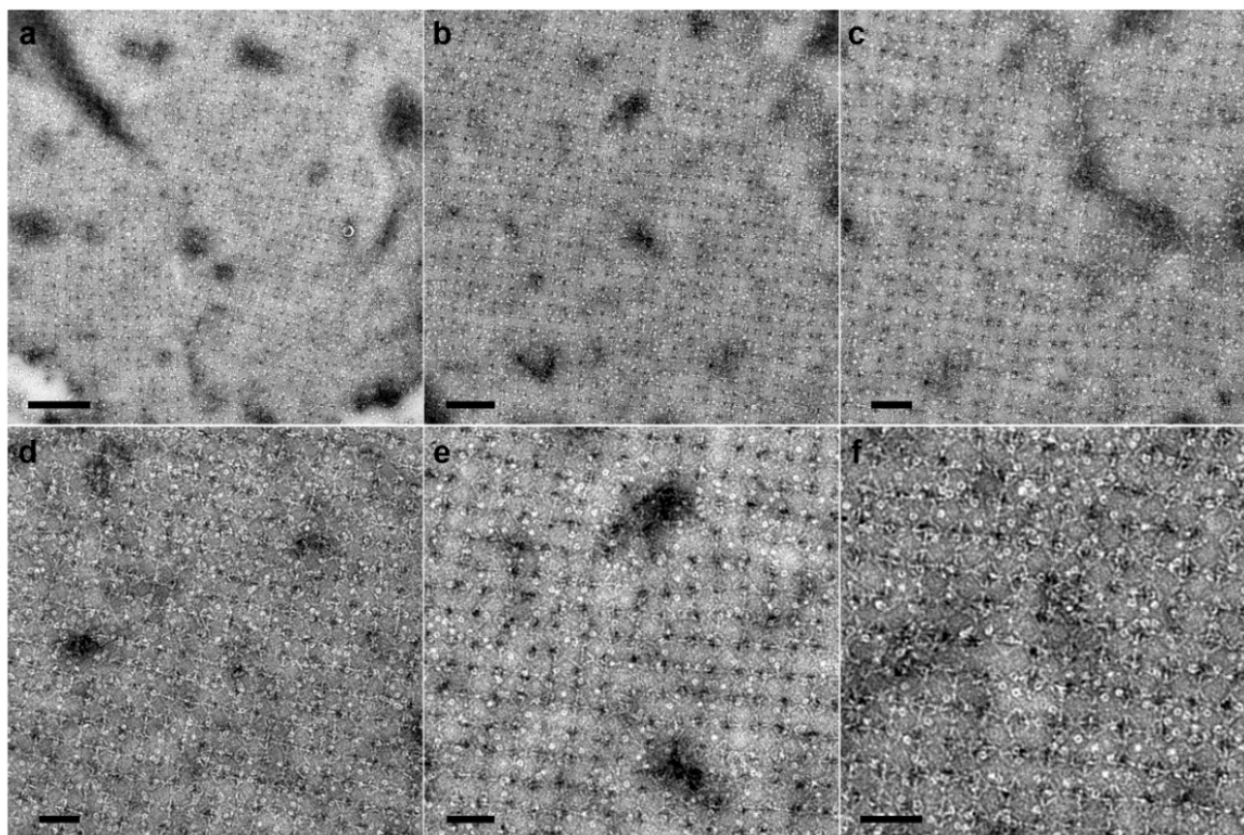
Supplementary Figure 14. Cryo-EM and single particle reconstruction of the structure of empty Octa. a, A cryo-EM micrograph after motion correction. b, Reference-free 2D class averages showing the representative views of Octa. c, 3D density maps of Octa viewed from the two-fold (left), three-fold (middle) and four-fold (right).



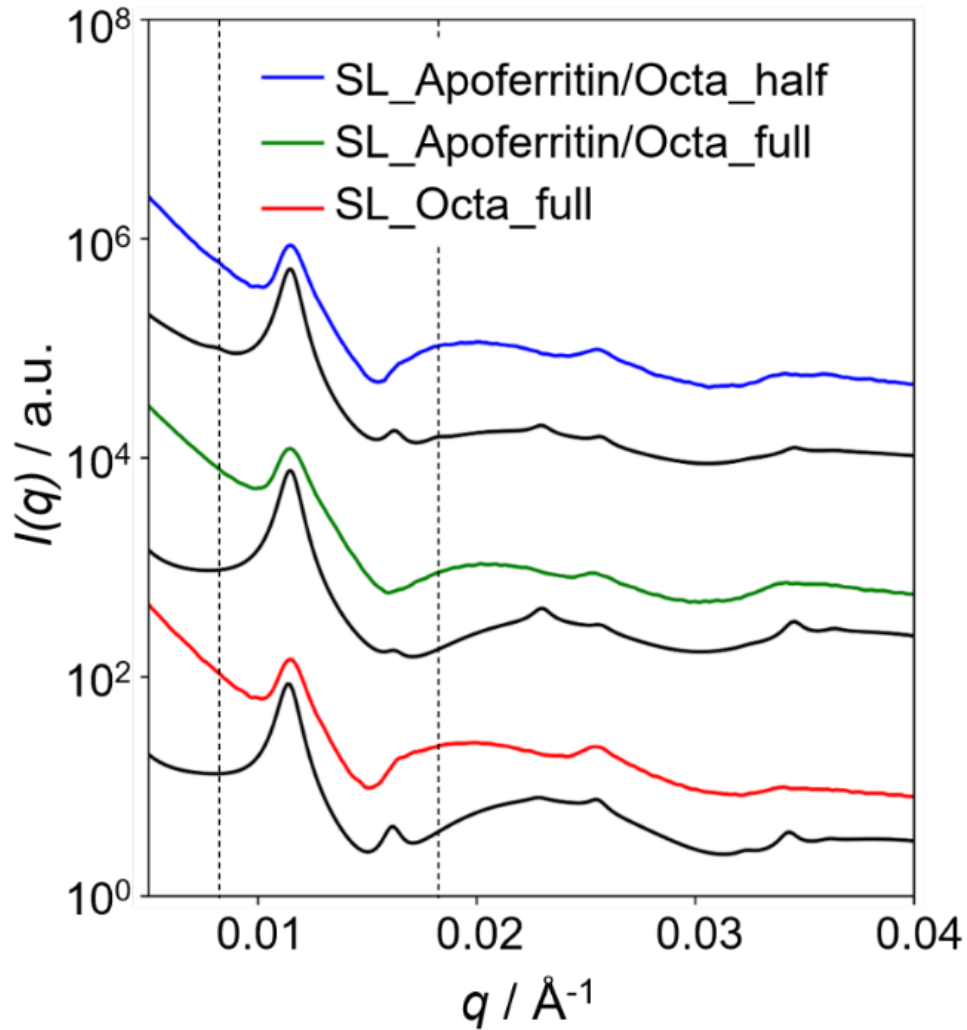
Supplementary Figure 15. Schematic view showing the inter-vertex linking motifs used for generating the 2D single-layered Octa and protein/Octa lattices in Fig. 3. The red solid lines and dashed lines extended from two Octa represent the in-plane complementary DNA pair in the one-colored system. a ($=22$) is a poly T part from Octa 1 vertex, b ($=22$) is the poly T part from the Octa 2 vertex, and c ($=8$) is composed of complementary bases that hybridize between strands.



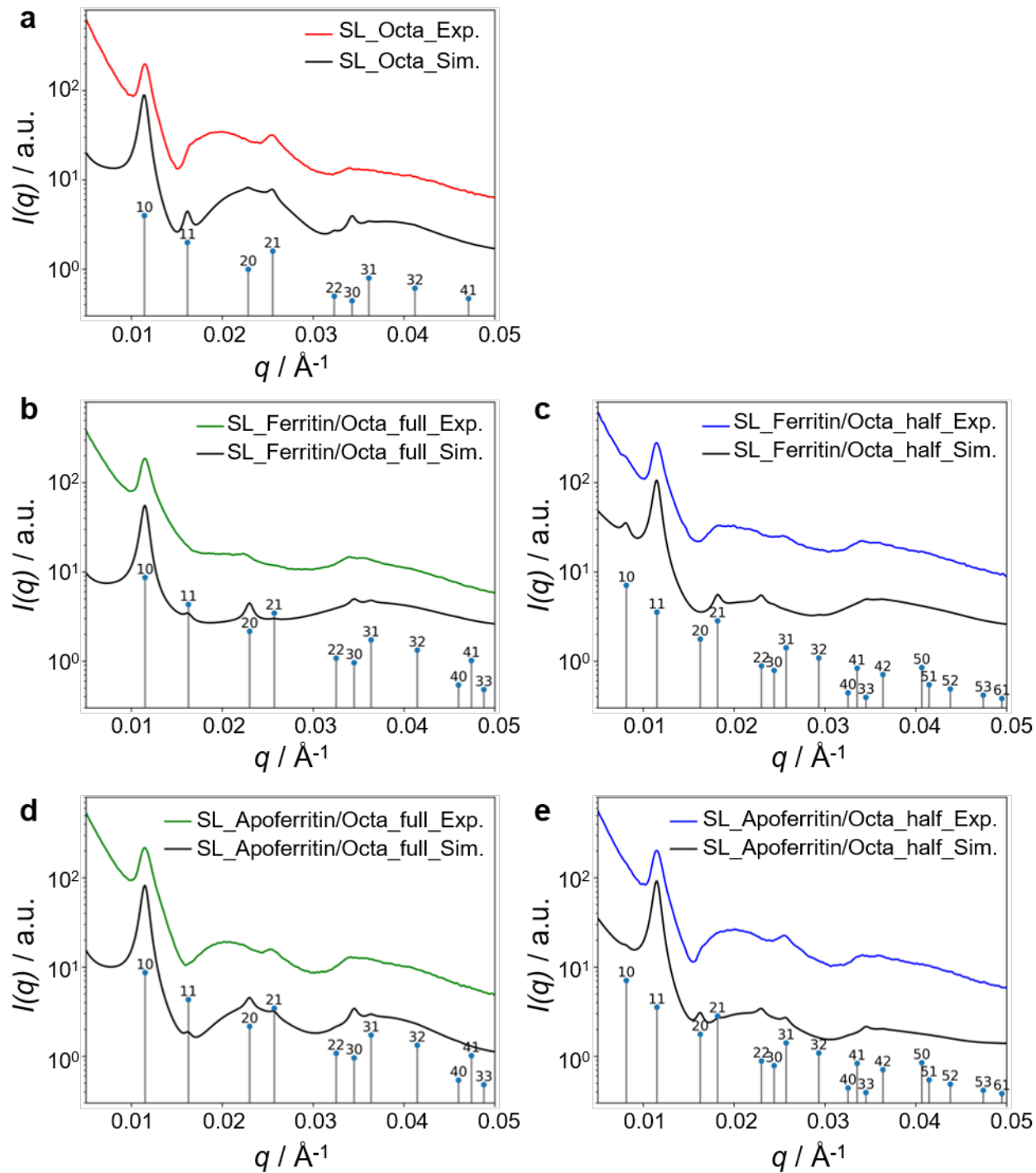
Supplementary Figure 16. Negative-stained TEM images of the 2D single-layered ferritin/Octa lattices. The globular structures (black) are ferritins (scale bars: 200 nm).



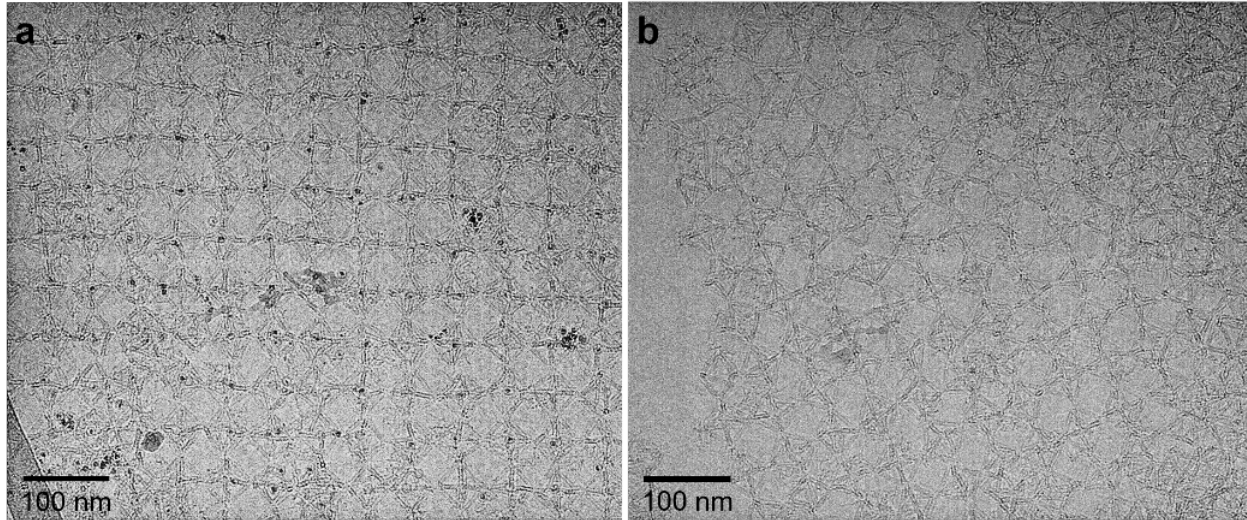
Supplementary Figure 17. Negative-stained TEM images of the 2D single-layered apoferritin/Octa lattices (scale bars: a-c, 200 nm and d-f, 100 nm).



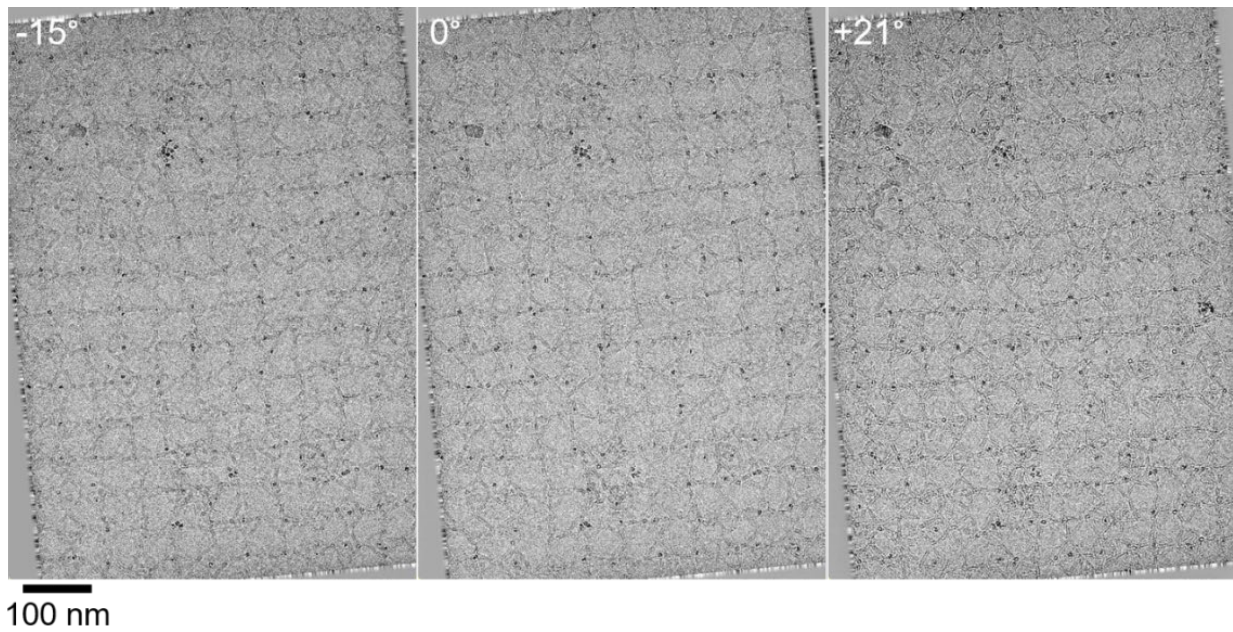
Supplementary Figure 18. SAXS analyses showing experimental data (colored lines) and simulated results (black lines) of the 2D single-layered empty Octa, full-filled apoferritin/Octa, and half-filled apoferritin/Octa.



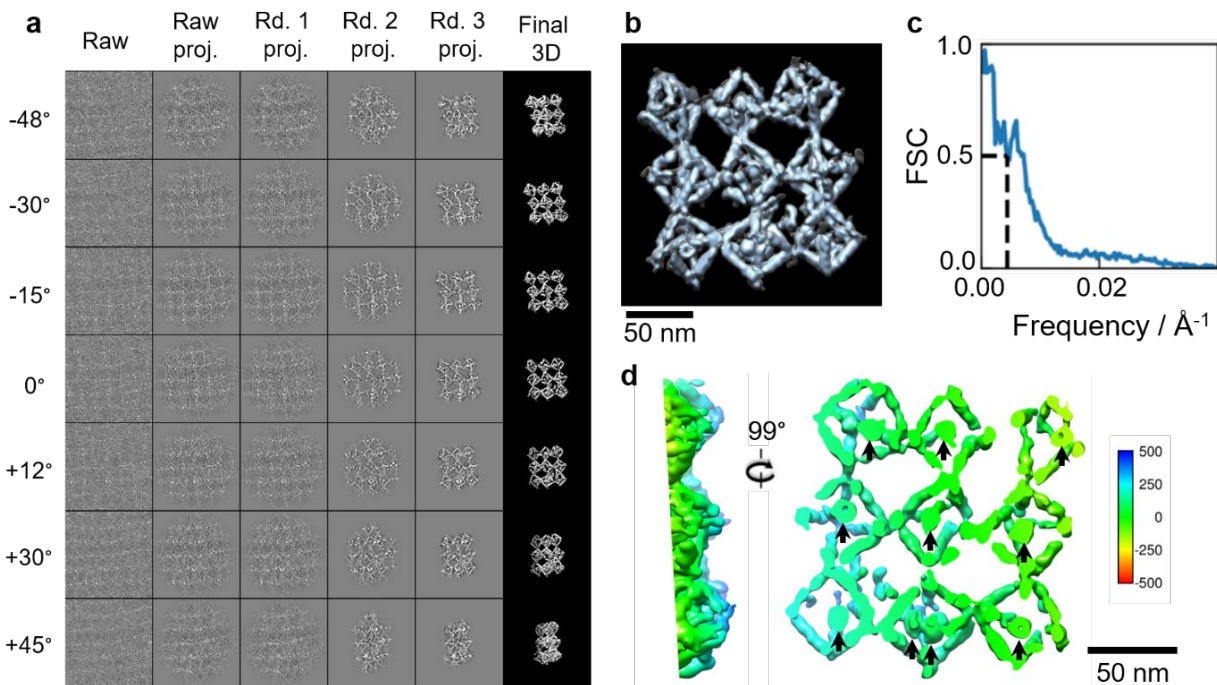
Supplementary Figure 19. SAXS analyses showing the experimental data (colored lines) and simulated results (black lines) of the 2D single-layered a, empty Octa, b, full-filled ferritin/Octa, c half-filled ferritin/Octa, d, full-filled apoferritin/Octa and e, half-filled apoferritin/Octa. For each simulated curve, indices of the corresponding scattering peaks are shown.



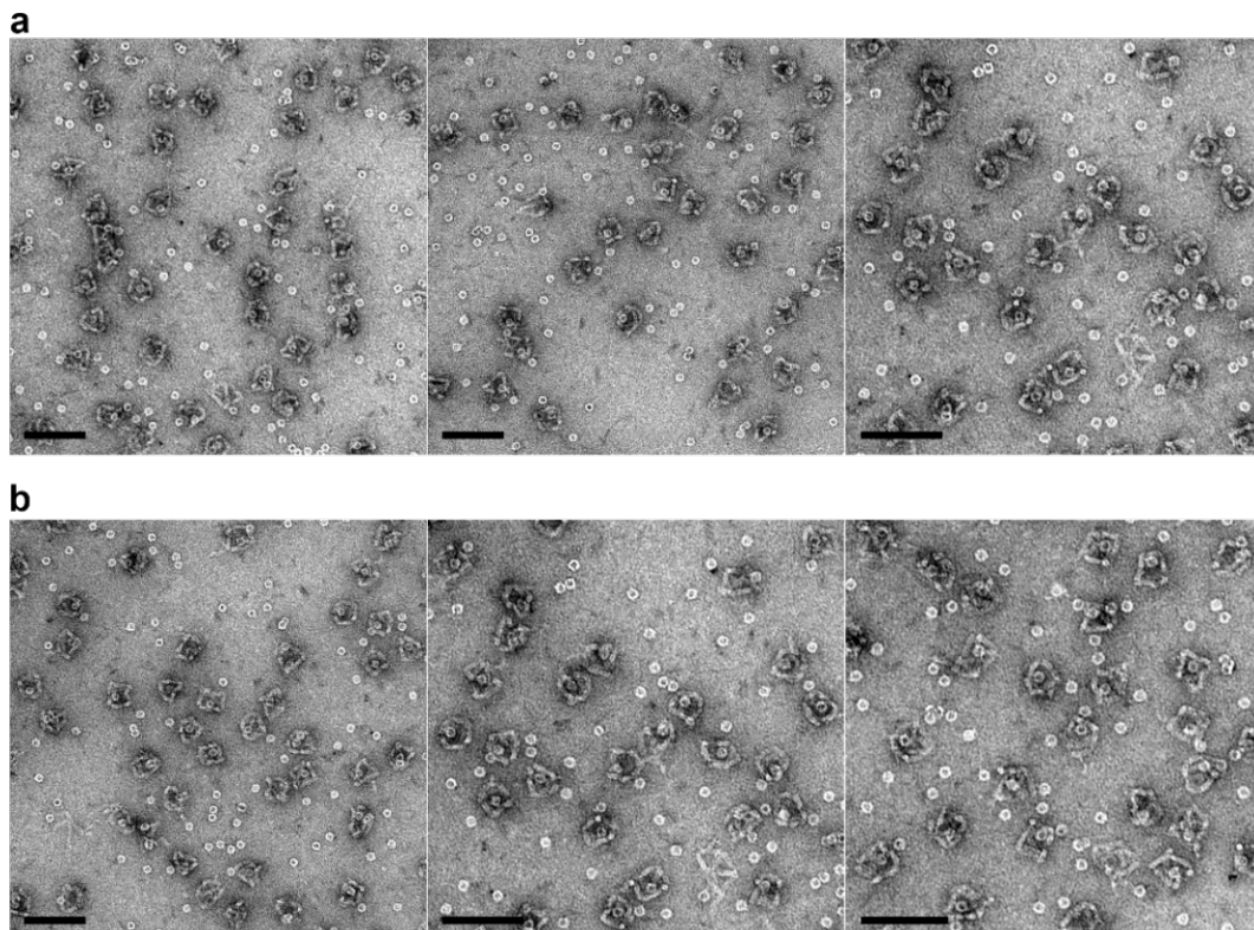
Supplementary Figure 20. Cryo-EM images of 2D single-layered a, ferritin/Octa lattices and b, empty Octa.



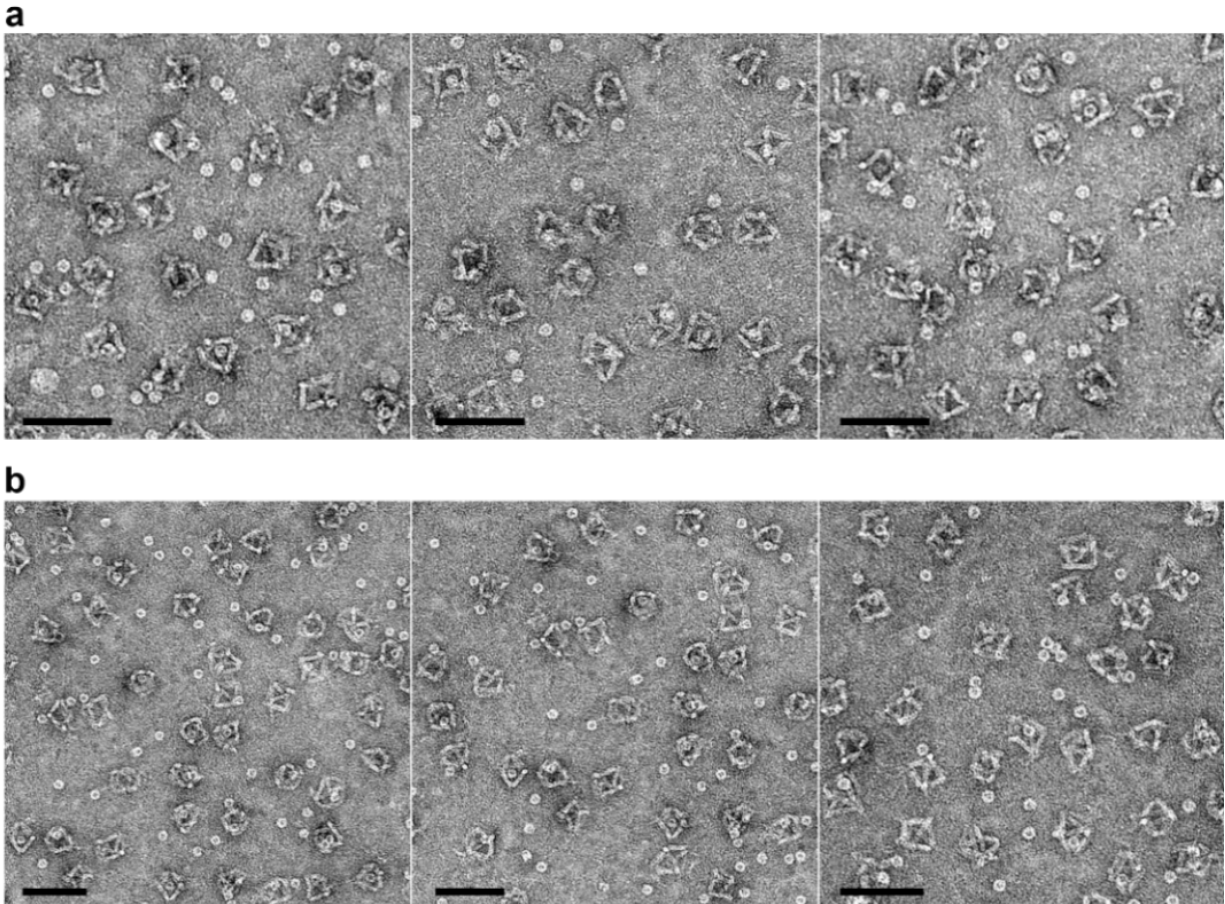
Supplementary Figure 21. Representative images of Cryo-ET tilt series of the single-layered 2D ferritin/Octa lattice. The single-layered lattice structure and the integration of ferritin into the structure were confirmed at the selected tilted angles.



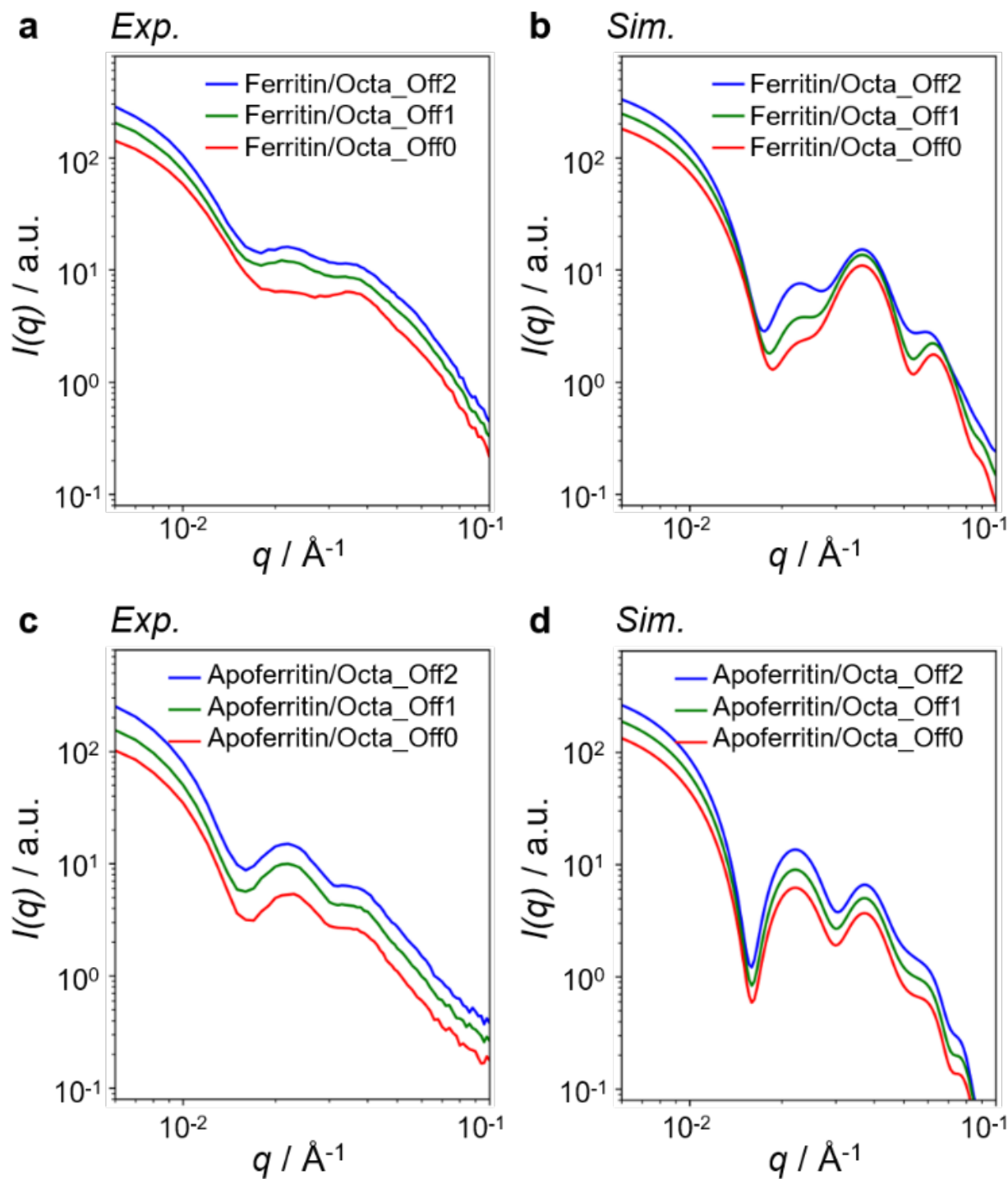
Supplementary Figure 22. IPET 3D reconstruction processes of the single-layered ferritin/Octa lattice. a, Seven representative tilt images of the select area of a ferritin/Octa lattice. Nine single ferritin/Octa in the select area are displayed in the first column from the left. Using IPET, the tilt images are aligned to a common center *via* iterative refinements. The projections of raw, intermediate and final 3D reconstructions at the corresponding tilt angles are displayed in the next five columns. b, The final 3D density map. c, FSC analyses showing the resolution of the final 3D density map, which was estimated to be ~ 225 Å. d, A colormap for Fig. 3f showing the overlay of the encapsulated ferritin with the single-layered lattice in one structure. The black arrows indicate the protein positions in each Octa in the lattice. The color bars indicate Z height (unit: Å).



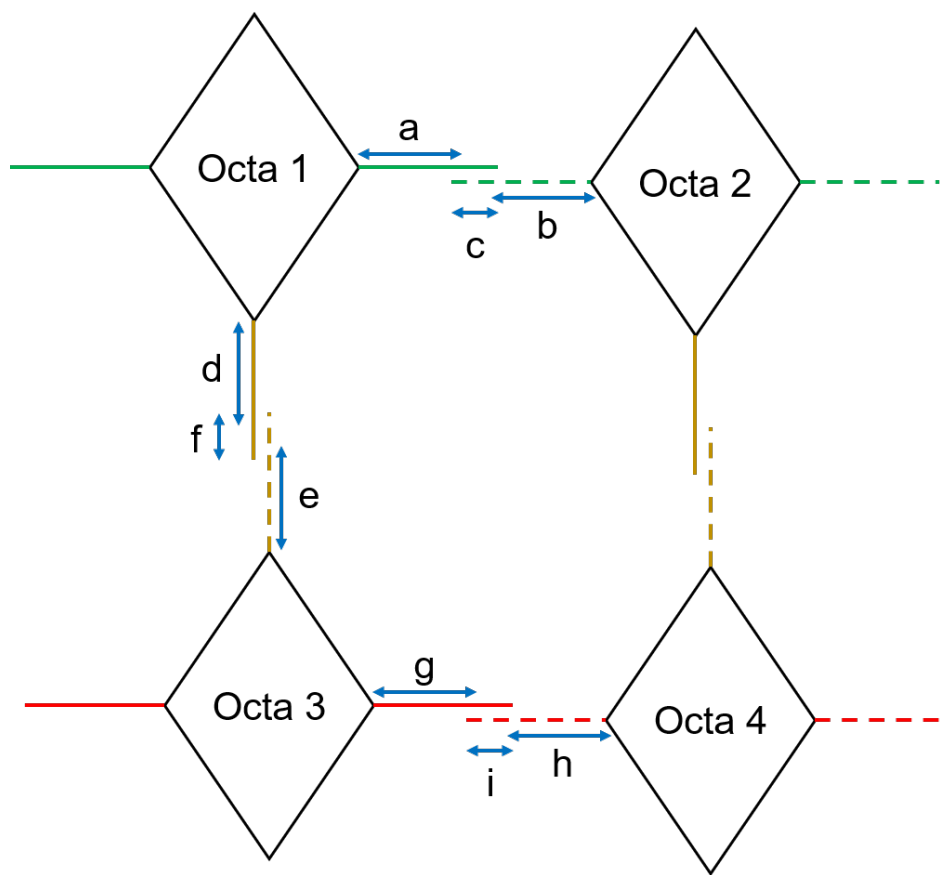
Supplementary Figure 23. Negative-stained TEM images of ferritin encapsulation at the off-centered positions inside Octa (a, ferritin/Octa_Off1; b, apoferritin/Octa_Off2). Scale bars: 100 nm.



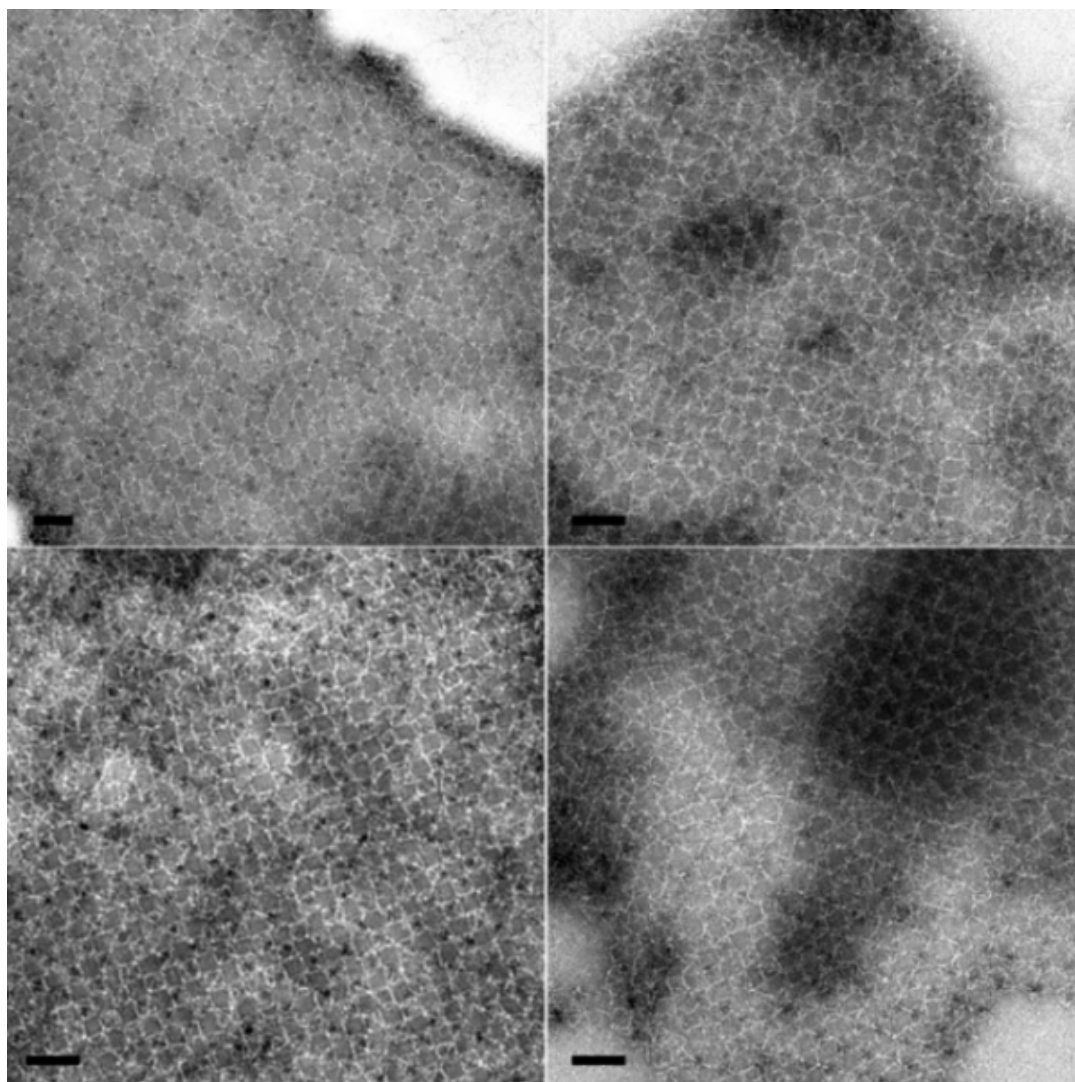
Supplementary Figure 24. Negative-stained TEM images of apoferritin encapsulation at the off-centered positions inside Octa (a, apoferritin/Octa_Off1; b, apoferritin/Octa_Off2). Scale bars: 100 nm.



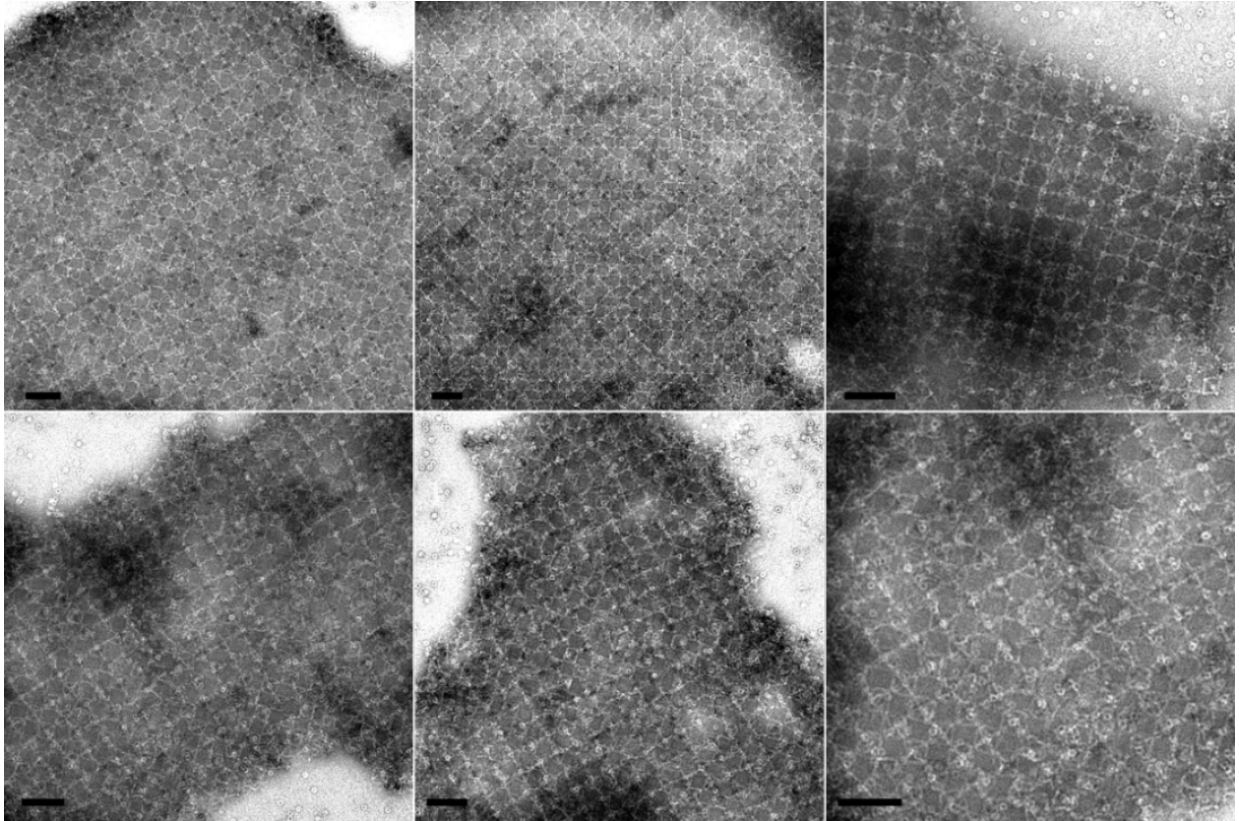
Supplementary Figure 25. SAXS analyses of a, b, single ferritin/Octa and c, d, single apoferritin/Octa, where the proteins were positioned at the center (Off0) or off-center (Off1 and Off2, Supplementary Fig. 7) inside Octa. a, c show the experimental data, and b, d are the simulated results. In these simulated results, proteins were assumed to be 100% encapsulated inside Octa. The plots in each panel are vertically shifted for display purpose.



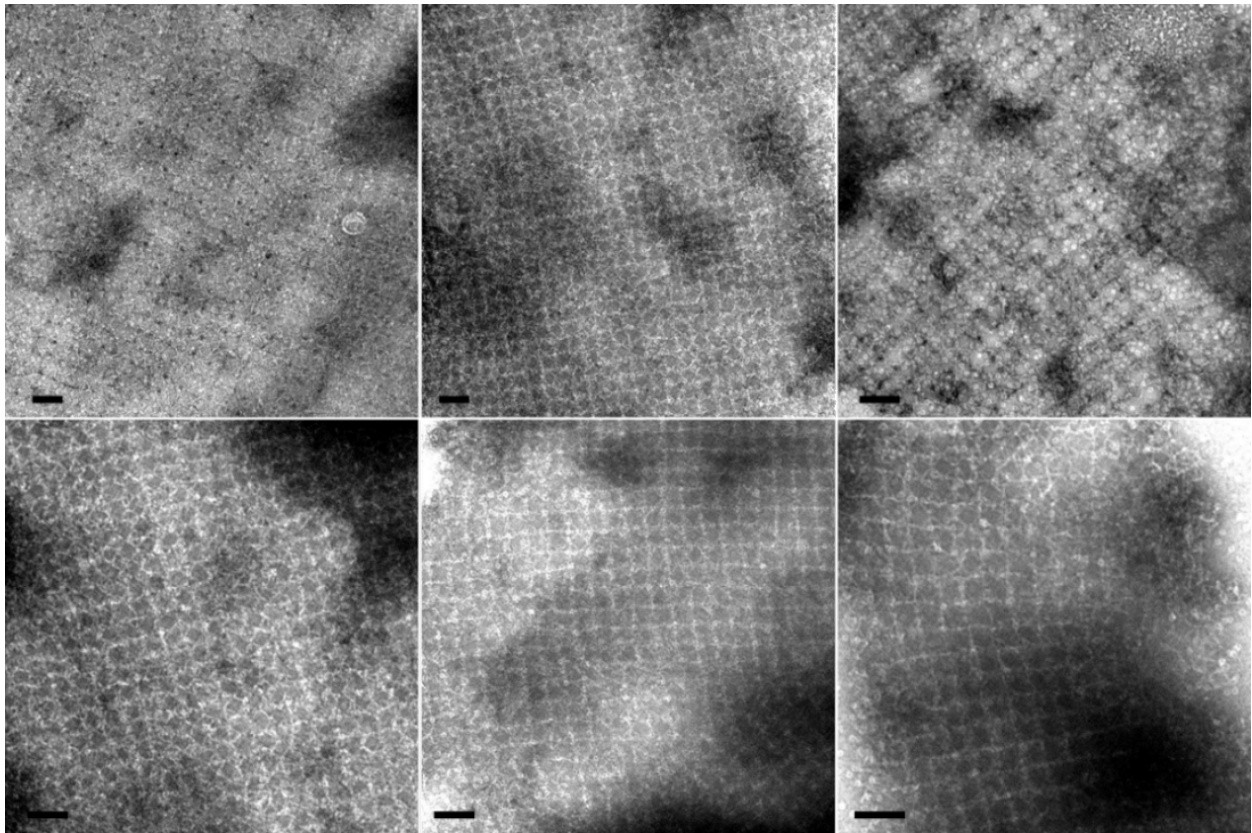
Supplementary Figure 26. Schematic view showing the inter-vertex linking motifs used for generating the 2D double-layered Octa and protein/Octa lattices in Fig. 4. The solid lines and dashed lines with matching colors extended from two Octa represent three sets (two in-plane and one out-of-plane) of the complementary DNA pairs in the three-colored vertex encoding system. a, b, d, e, g, h (=22) are the poly T parts from Octa vertices, and c, f and i (=8 or 12) are composed of different complementary bases that hybridize between strands.



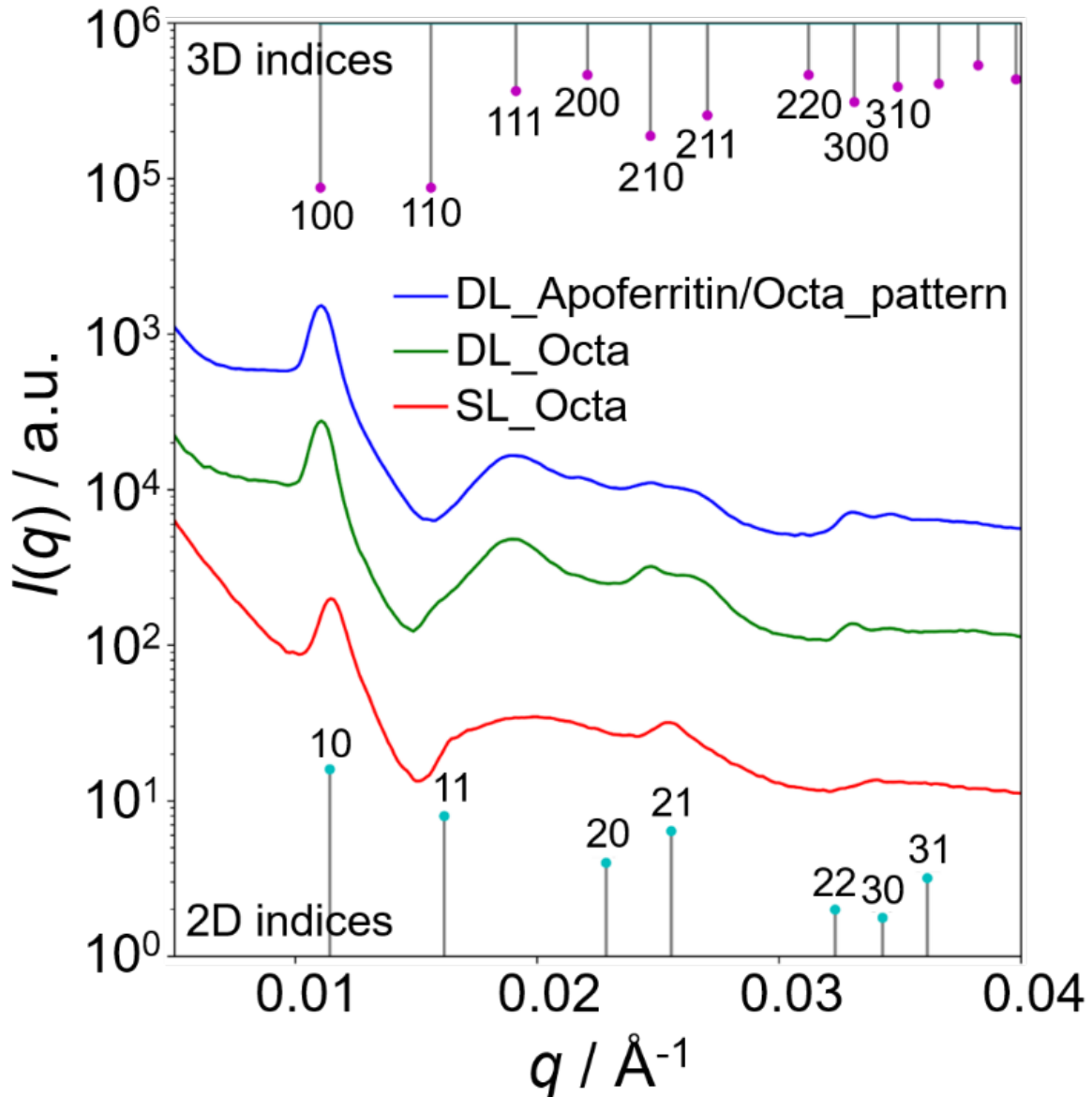
Supplementary Figure 27. Negative-stained TEM images of 2D double-layered Octa lattice (scale bars: 100 nm).



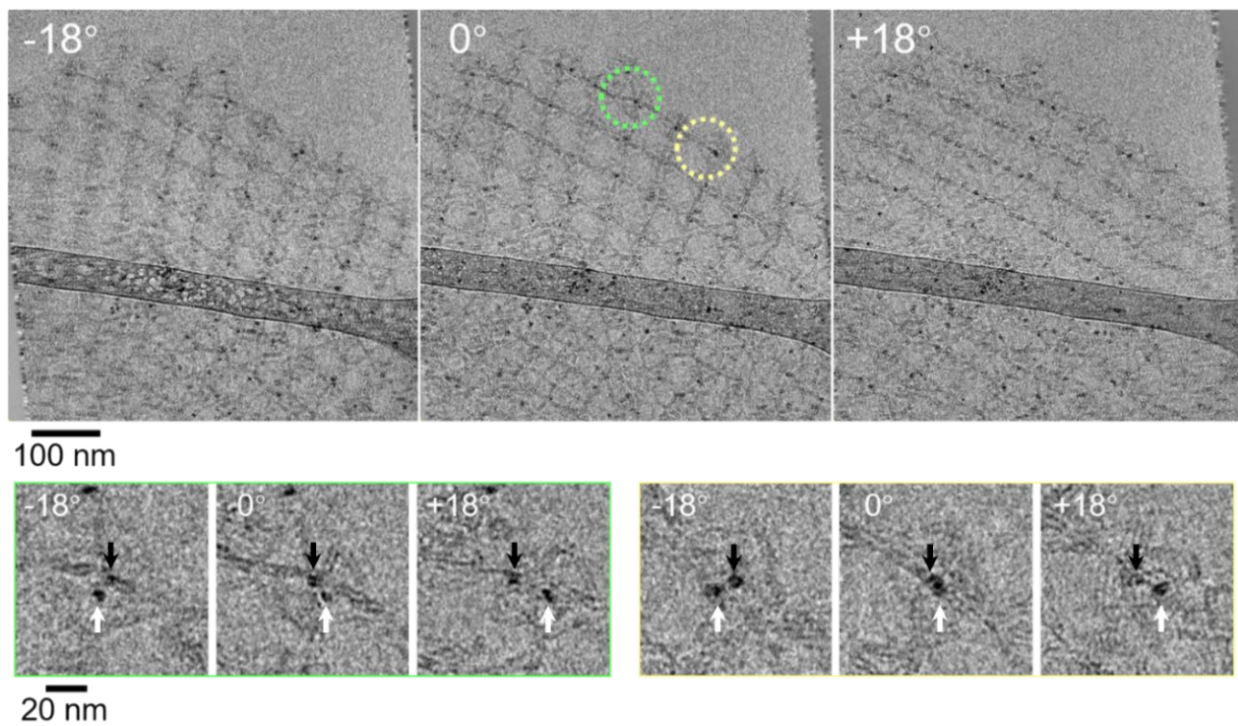
Supplementary Figure 28. Negative-stained TEM images of 2D double-layered ferritin/Octa lattice (scale bars: 100 nm).



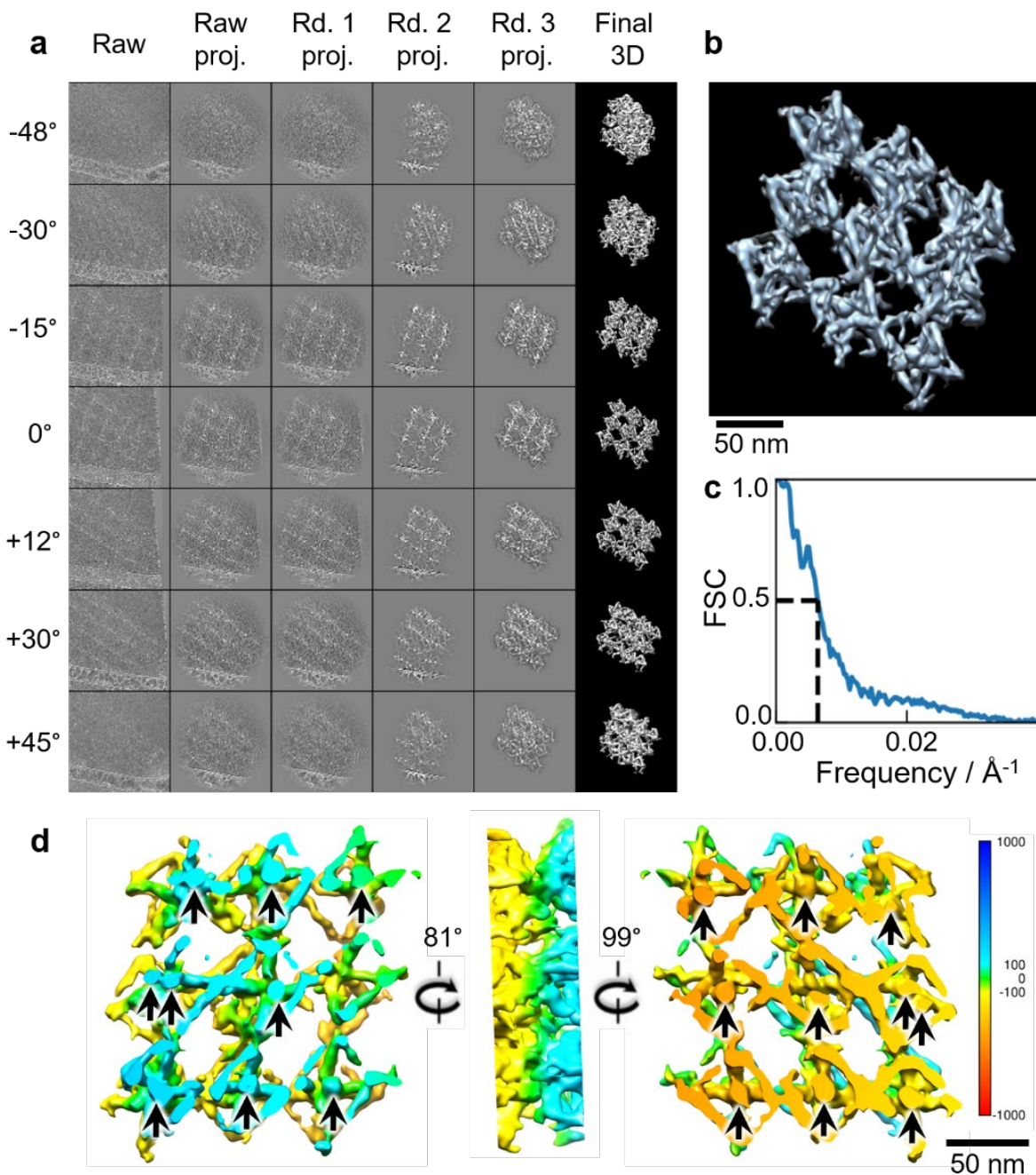
Supplementary Figure 29. Negative-stained TEM images of the 2D double-layered apoferritin/Octa lattice (scale bars: 100 nm).



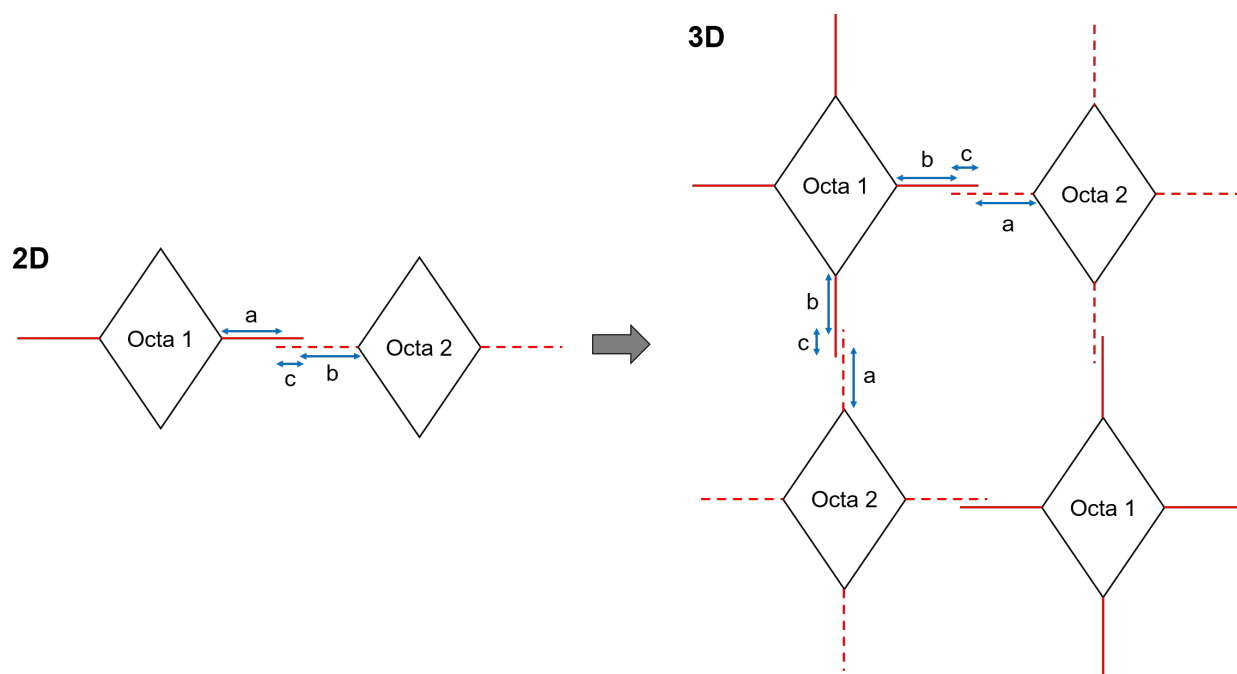
Supplementary Figure 30. SAXS profiles of the 2D double-layered empty Octa and apoferritin/Octa lattices show co-localization of apoferritin and the Octa lattice. Compared to the double-layered ferritin/Octa sample in Fig. 4b, the smaller change in the scattering intensity of apoferritin/Octa relative to an empty Octa lattice was understood by the close electron densities of hollow protein shell and Octa. Compared to a single-layered lattice, formation of a double-layered structure was supported by the emergence of broad peaks at the correspondent 3D indices of a simple cubic lattice, suggesting the presence of an additional layer in the z direction.



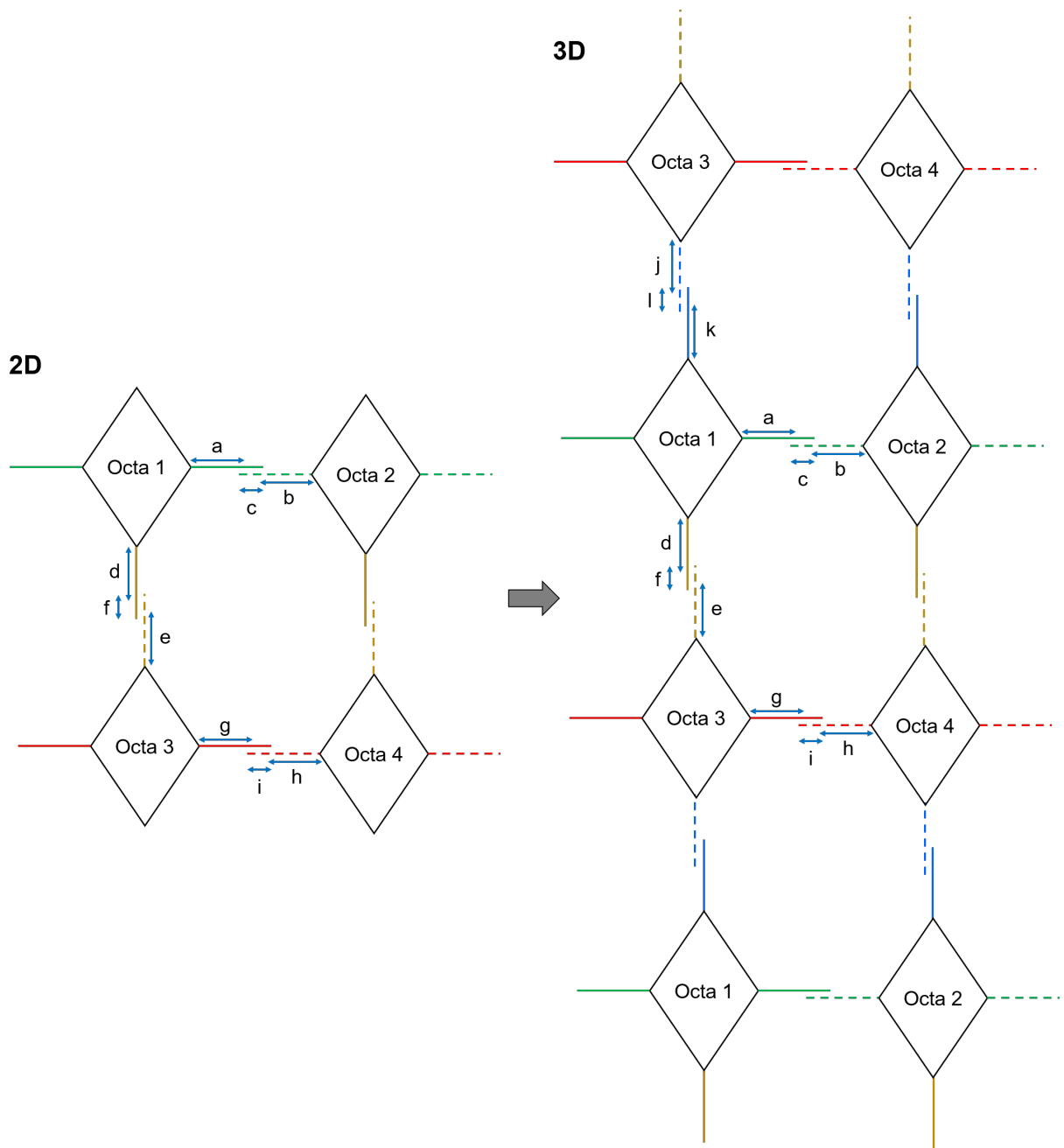
Supplementary Figure 31. Representative tilt images of Cryo-ET of the 2D double-layered ferritin/Octa lattice. The presence of two ferritins at the top and bottom layers was confirmed at tilted angles, which agreed with our design. Magnified images at the circled locations were shown at the bottom and were used in Fig. 4d. The two ferritins at the top and bottom layers were shown at tilted angles and pointed out by the black and white arrows.



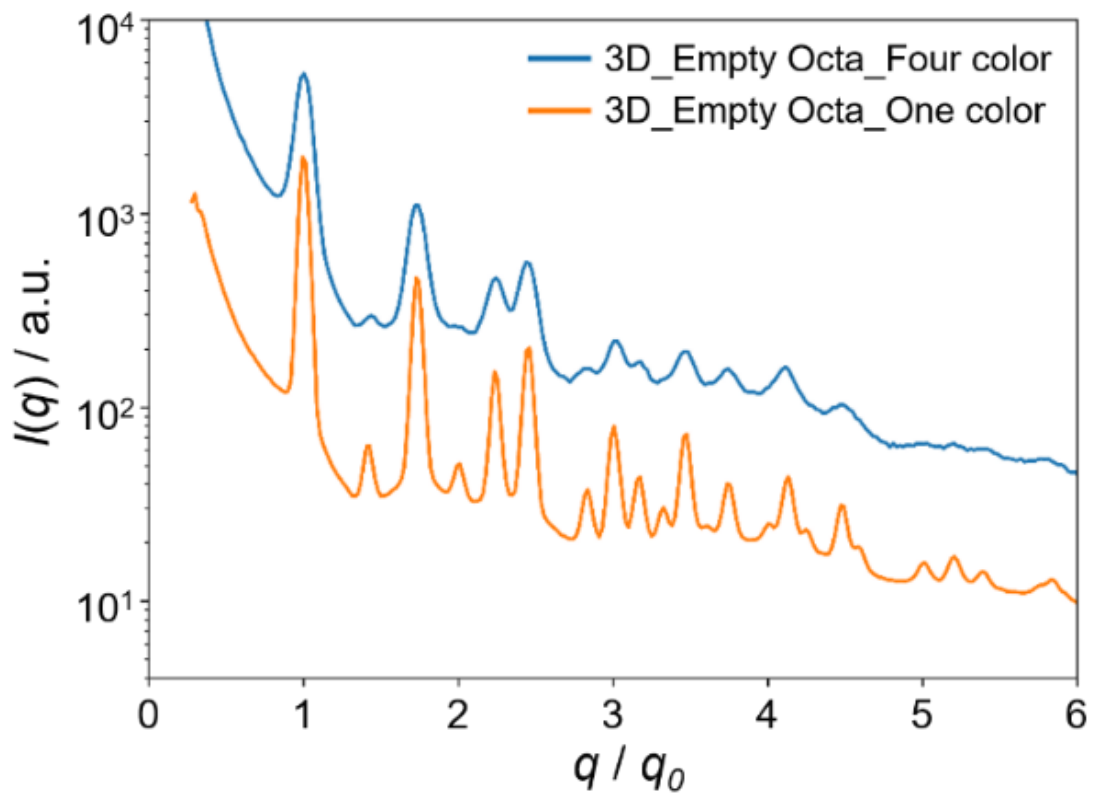
Supplementary Figure 32. IPET 3D reconstruction processes of the double-layered ferritin/Octa lattice. a, Seven representative tilt images of the select area of the ferritin/Octa lattice. The eighteen single ferritin/Octa from the top and bottom layers in the select area are displayed in the first column from the left. Using IPET, the tilt mages are aligned to a common center *via* iterative refinements. The projections of raw, intermediate and final 3D reconstructions at the corresponding tilt angles are displayed in the next five columns. b, The final 3D density map. c, FSC analyses showing the resolution of the final 3D density map, which was estimated as 156 Å. d, A colormap for Fig. 4f showing the overlay of the encapsulated ferritin with the double-layered lattice in one structure. The black arrows indicate the protein positions in each Octa in the lattice. The color bars indicate Z height (unit: Å).



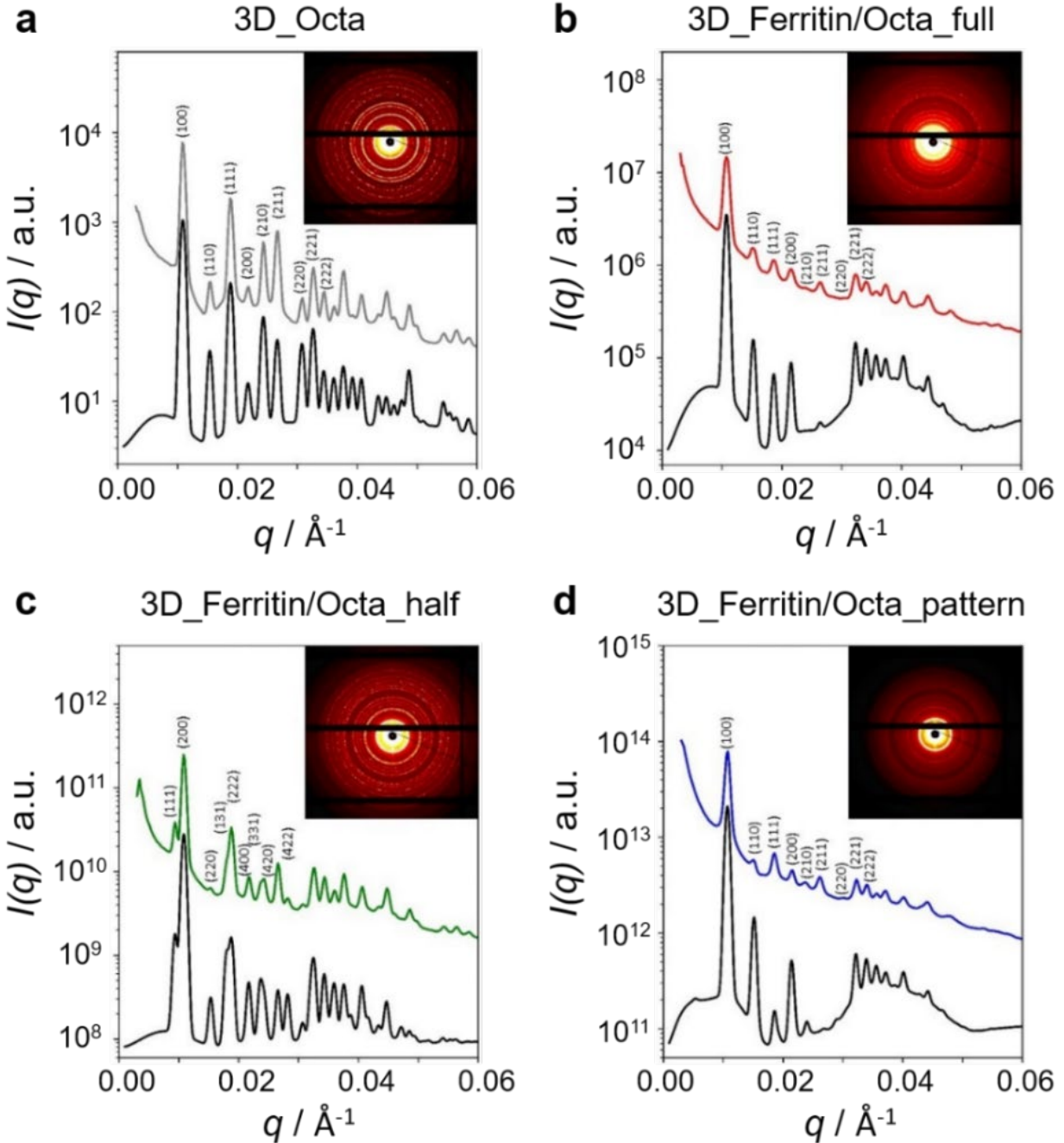
Supplementary Figure 33. Schematic view showing the inter-vertex linking motifs used for the 3D assembly of the Octa lattices and protein/Octa lattices in Fig. 5. The one-colored 3D system is extended from the 2D system in Fig. 3 and Supplementary Fig. 15, in which the red solid lines and dashed lines represented the one set of complementary DNA pairs used in this system. a and b (=22) are the poly T parts from the Octa vertices, and c (=8) is composed of complementary bases that hybridize between strands.



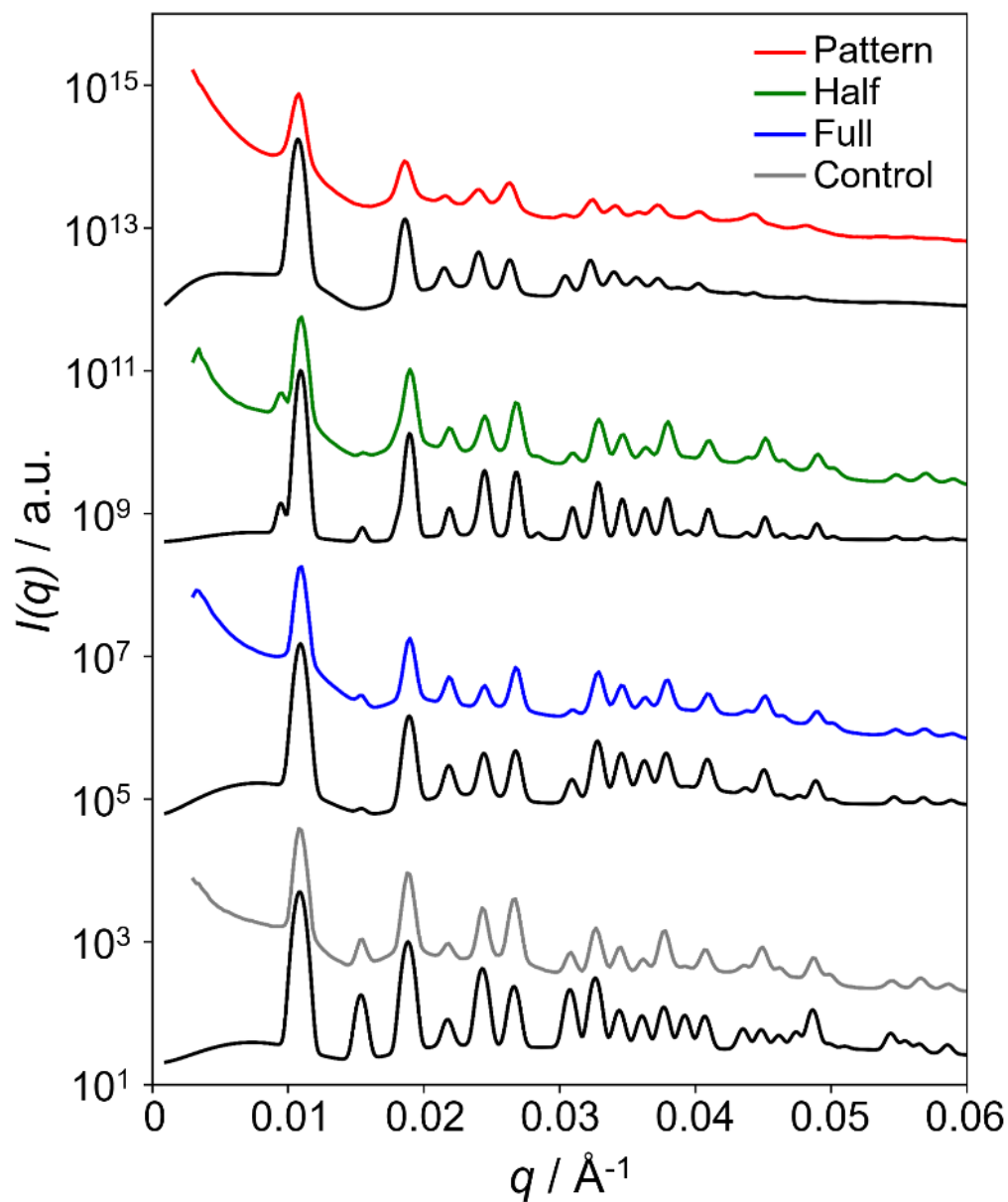
Supplementary Figure 34. Schematic view showing the inter-vertex linking motifs used for the 3D assembly of the Octa lattices and protein/Octa lattices in Fig. 5. The four-colored 3D system is extended from the 2D system in Fig. 4 and Supplementary Fig. 26, in which the solid lines and dashed lines with matching colors extended from the Octa vertices represented the four sets of complementary DNA pairs used in this system. a, b, d, e, g, h, i, k (=22) are the poly T parts from the Octa vertices, and c, e, i and l (=8 or 12) are composed of different complementary bases that hybridize between strands.



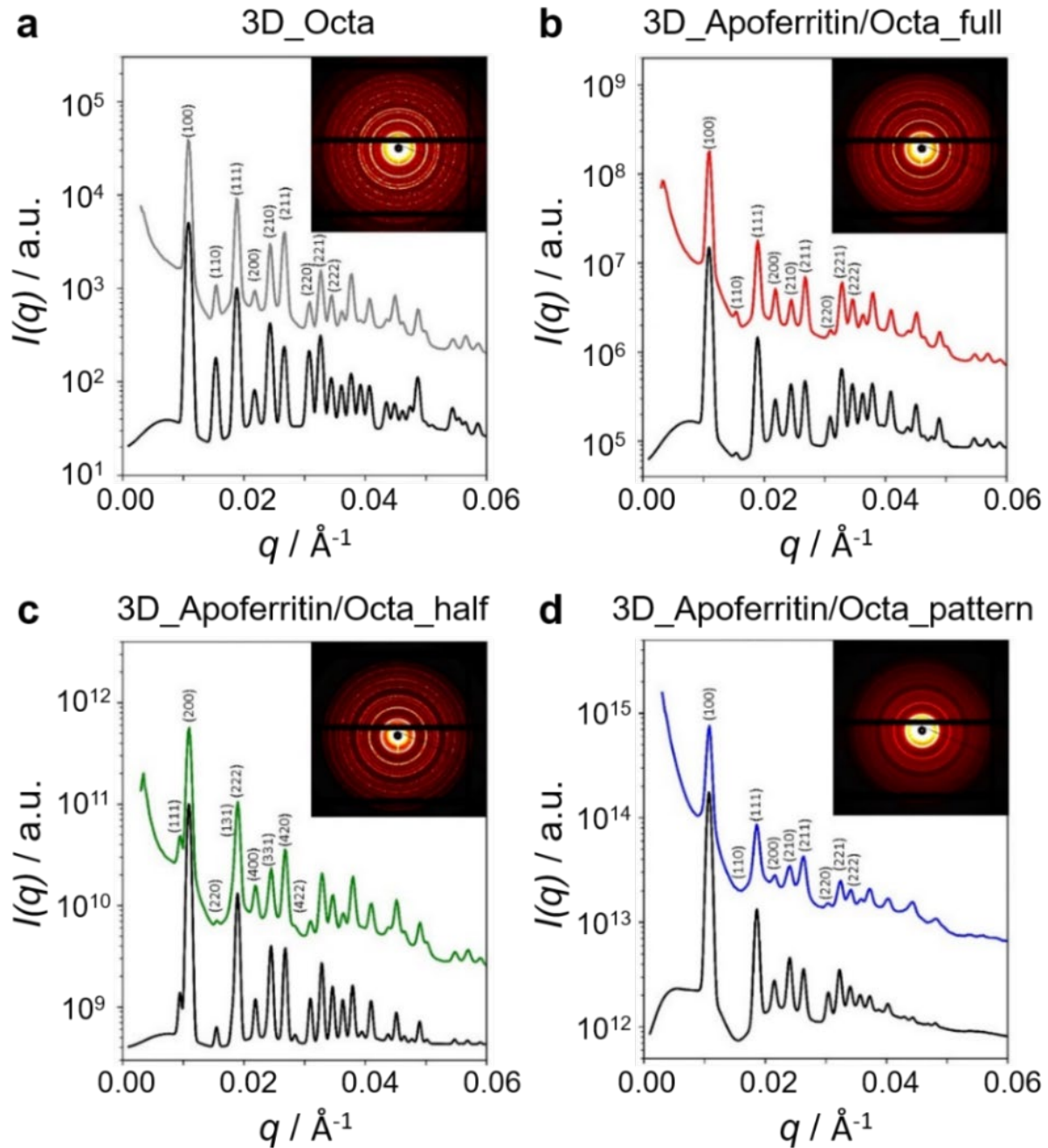
Supplementary Figure 35. Experimental SAXS data of the 3D empty Octa lattice designed with one color (orange curve) and with four colors (blue curve).



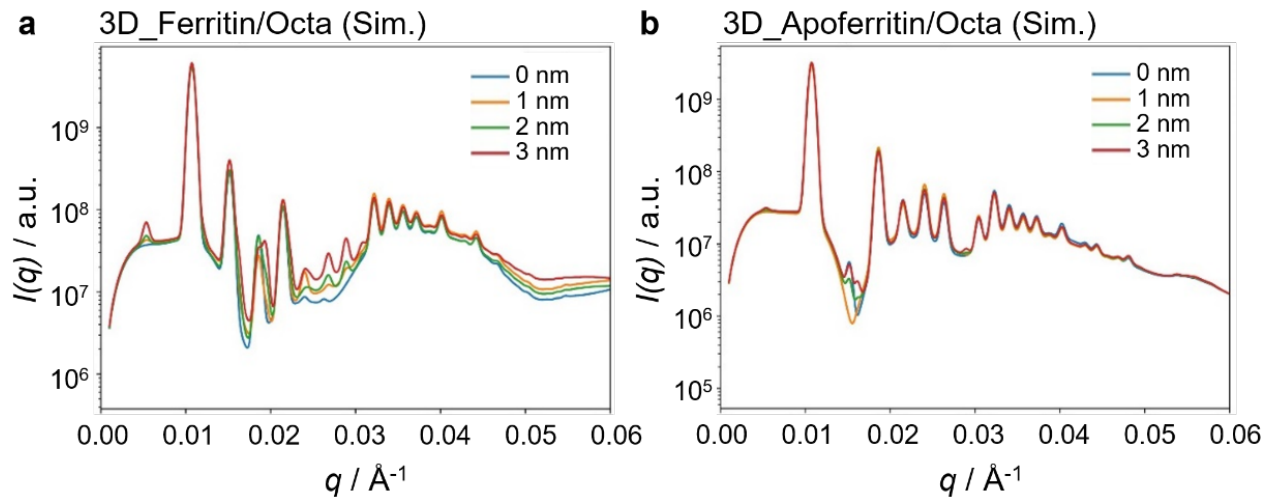
Supplementary Figure 36. Experimental (colored curves) and simulated (black curves) $I(q)$ profiles of the vertex driven Octa frameworks for ferritin assembly shown individually. a, Empty Octa and b, full-filled ferritin/Octa (b) relate to a simple cubic (SC) lattice, where ferritin attenuated the intensity by the stronger scattering at the iron core; c, half-filled ferritin/Octa relates to a face-centered cubic (FCC) lattice; and d, pattern ferritin/Octa relates to a SC lattice with a primitive tetragonal unit cell. Bragg reflections are indicated and the 2D SAXS patterns are shown (upper right inset) for each sample.



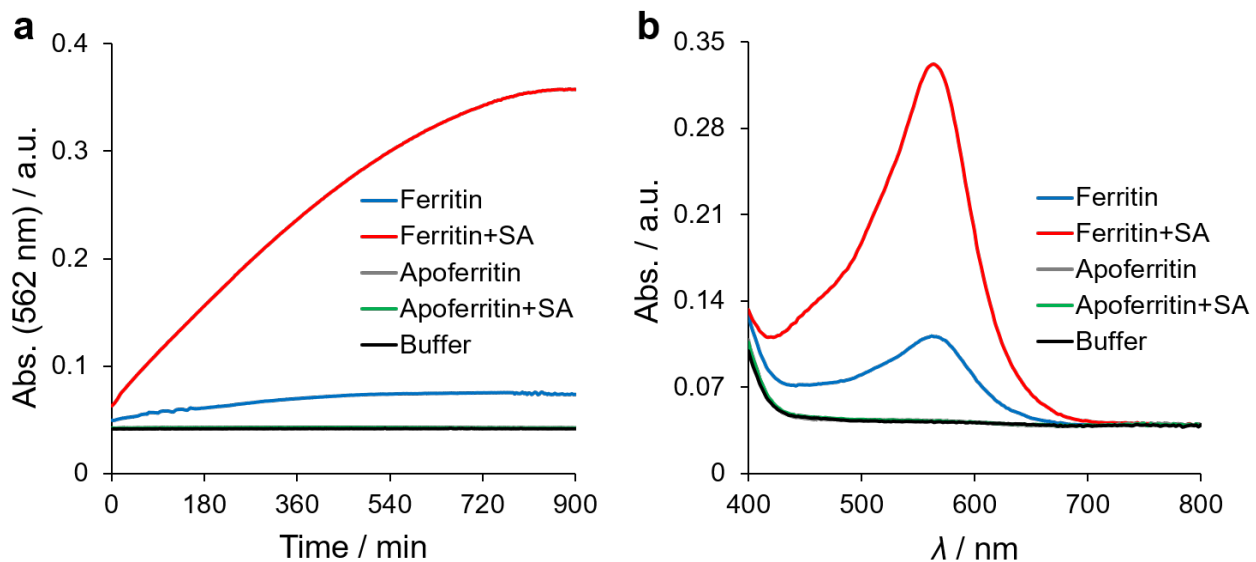
Supplementary Figure 37. SAXS analysis of 3D apoferritin/Octa lattices formed by encoded Octa frameworks. Experimental (colored curves) and simulated (black curves) $I(q)$ profiles of the different types of 3D apoferritin/Octa lattices, in which grey (empty Octa) and blue (full-filled apoferritin/Octa) relate to an SC lattice, green (half-filled apoferritin/Octa) relates to an FCC lattice; and red (pattern apoferritin/Octa) relates to a primitive tetragonal unit cell.



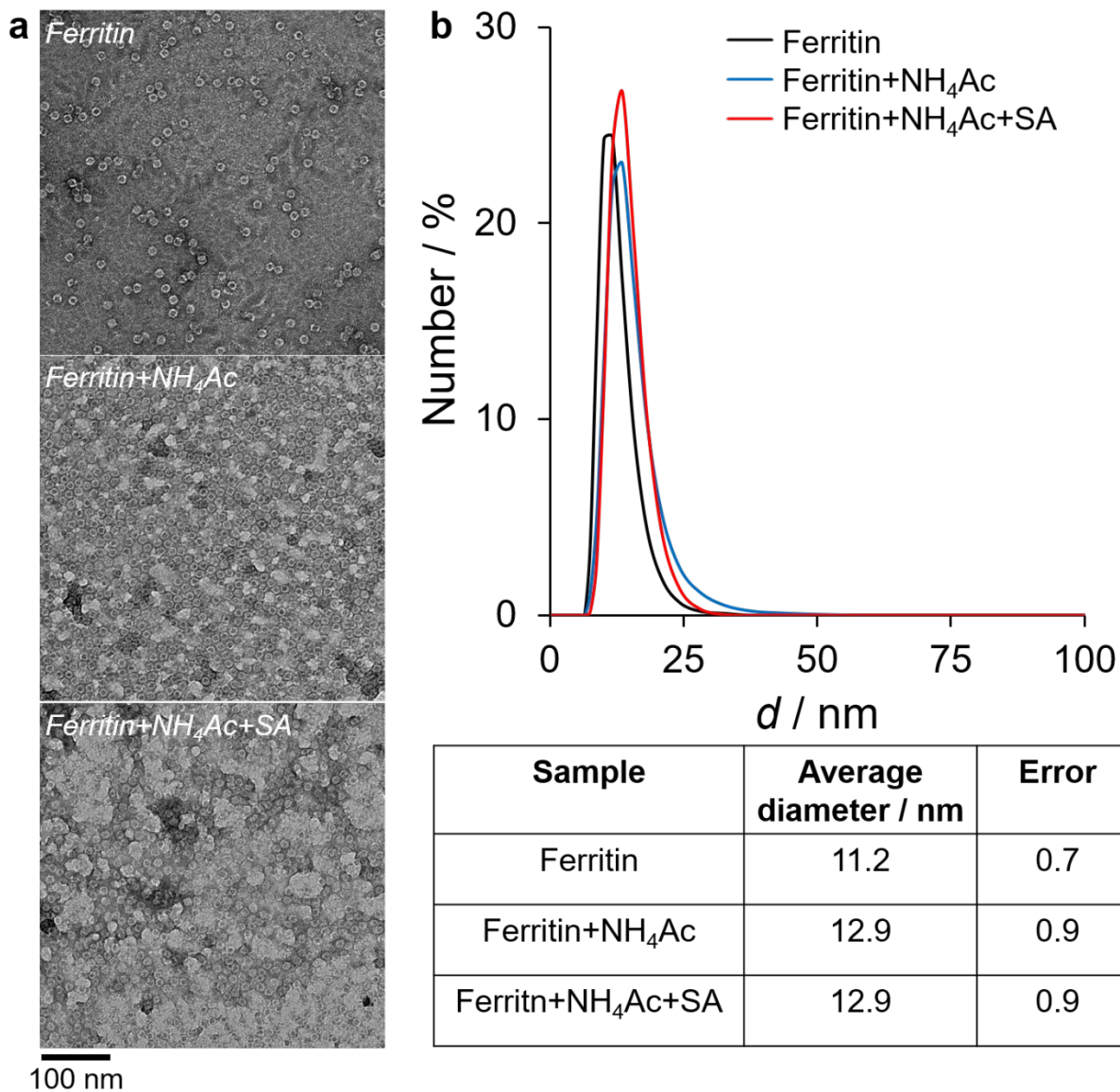
Supplementary Figure 38. Experimental (colored curves) and simulated (black curves) $I(q)$ profiles of the vertex driven Octa frameworks for apoferritin assembly shown individually. a, Empty Octa and b, full-filled apoferritin/Octa relate to a simple cubic (SC) lattice, where ferritin attenuated the intensity by the stronger scattering at the iron core; c, half-filled apoferritin/Octa relates to a face-centered cubic (FCC) lattice; and d, pattern apoferritin/Octa relates to a SC lattice with a primitive tetragonal unit cell. Bragg reflections are indicated and the 2D SAXS patterns are shown (upper right insets) for each sample.



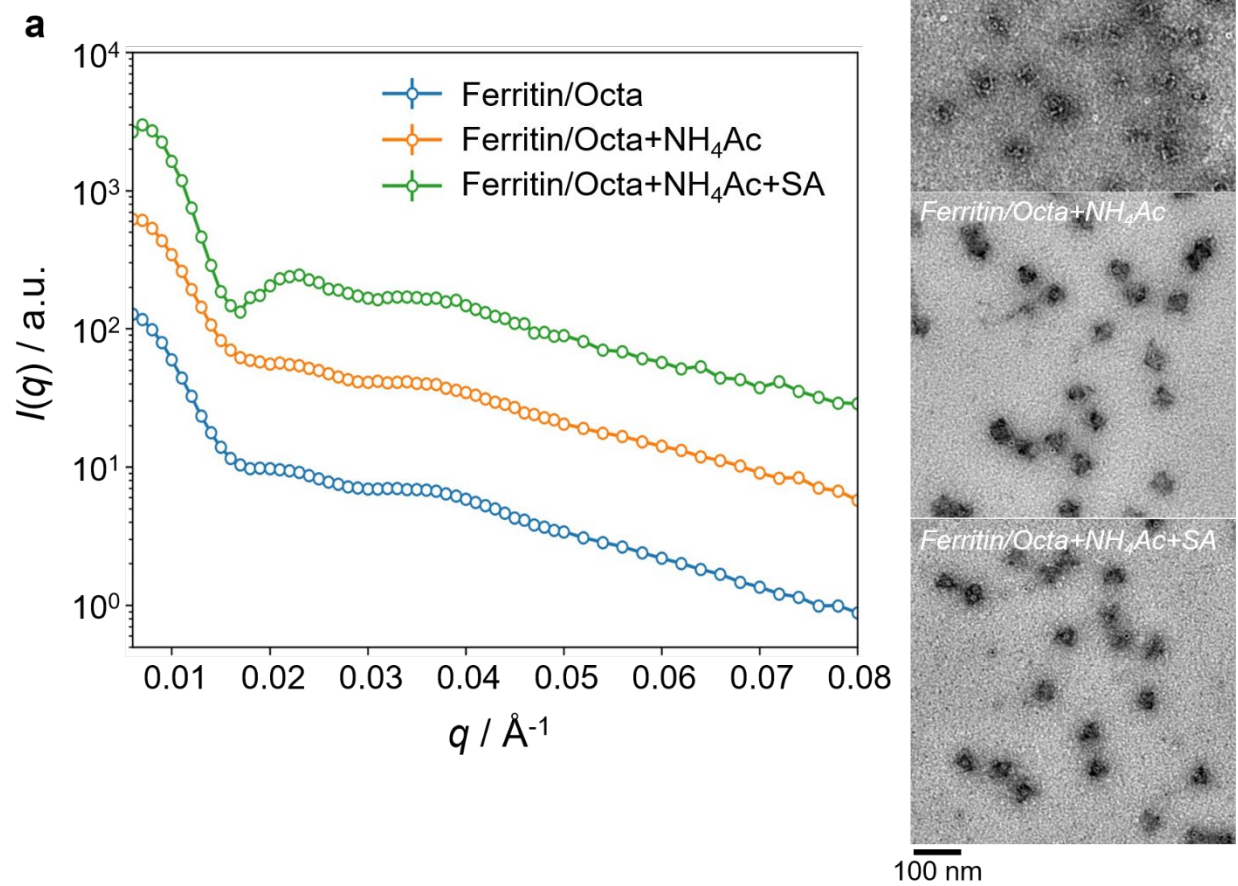
Supplementary Figure 39. Modelling showing the change of SAXS profiles by shifting (by a shown distance for correspondingly colored curves) the protein position from the center of Octa in a 3D lattice: a, shift of ferritin and b, shift of apoferritin.



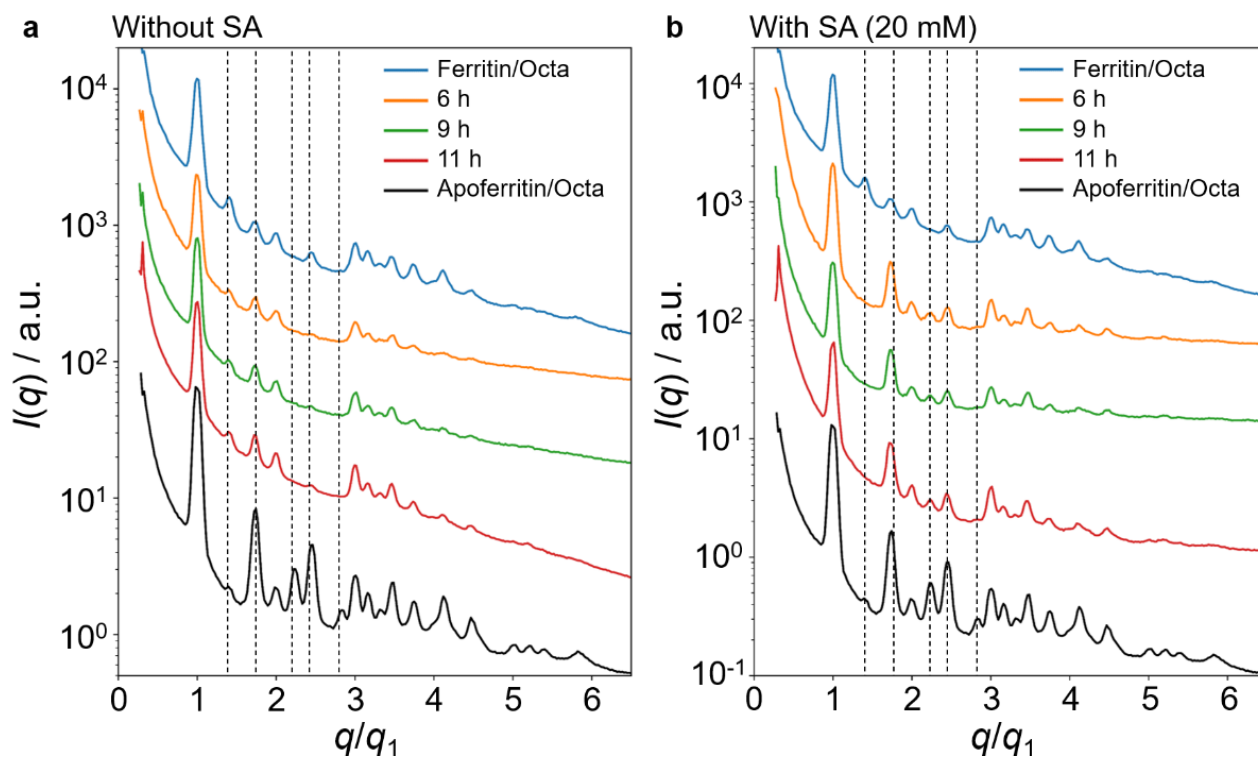
Supplementary Figure 40. a, Kinetic assays and b, absorption spectra of ferritin (50 nM) and apoferritin (50 nM) in the absence or presence of sodium ascorbate (SA, 2.5 mM). SA reduces the Fe^{3+} in ferritin and the released Fe^{2+} in solution forms a complex with ferrozine (2.5 mM), of which the Fe^{2+} -ferrozine complex shows an absorbance at 562 nm. The buffer solution contains 90% PBS buffer (pH 7.4) and 10 v/v% ammonium acetate solution (pH 5.5).



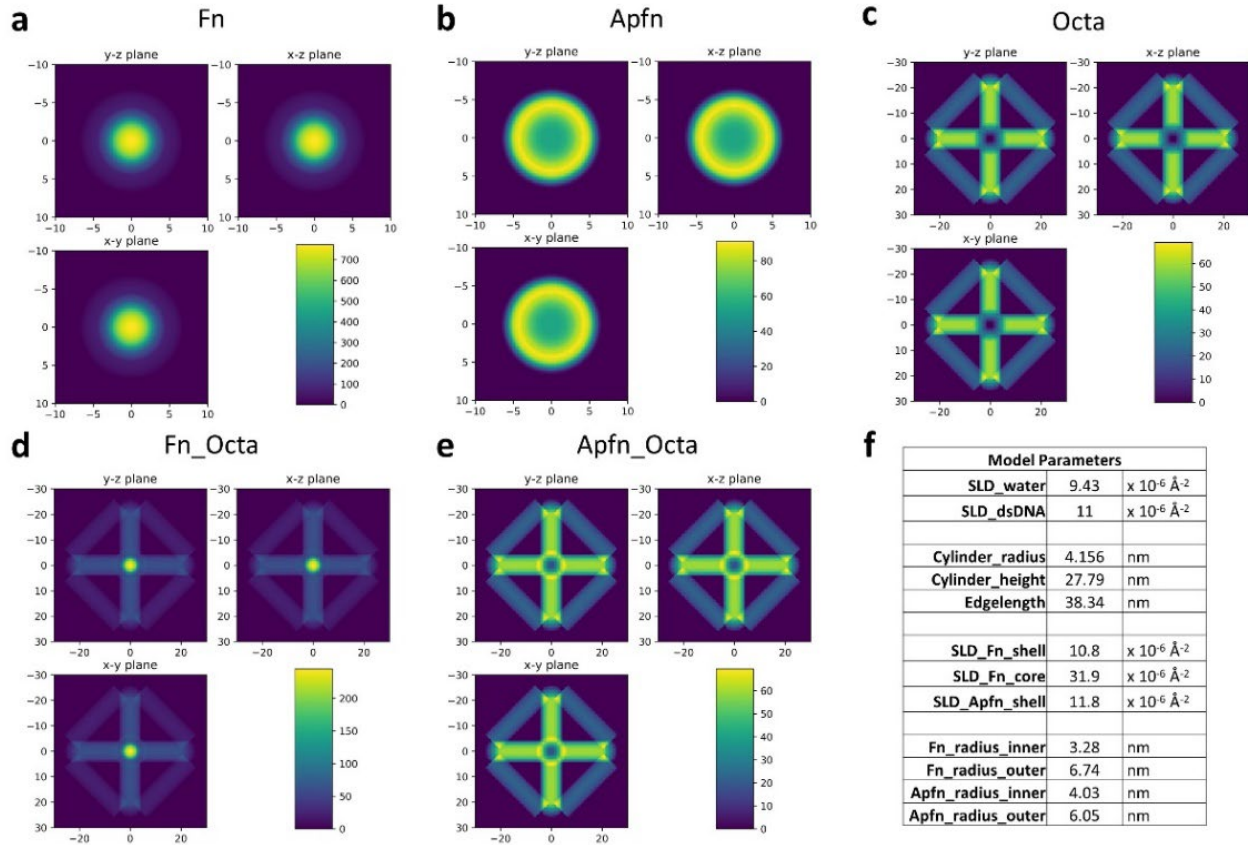
Supplementary Figure 41. a, TEM images and b, DLS ($n=3$) of free ferritin ($\sim 2 \mu\text{M}$) in PBS buffer (pH 7.4) and in the presence of sodium ascorbate (SA, 20 mM) and 10 v/v% of the ammonium acetate (NH₄Ac, pH 5.5) solution.



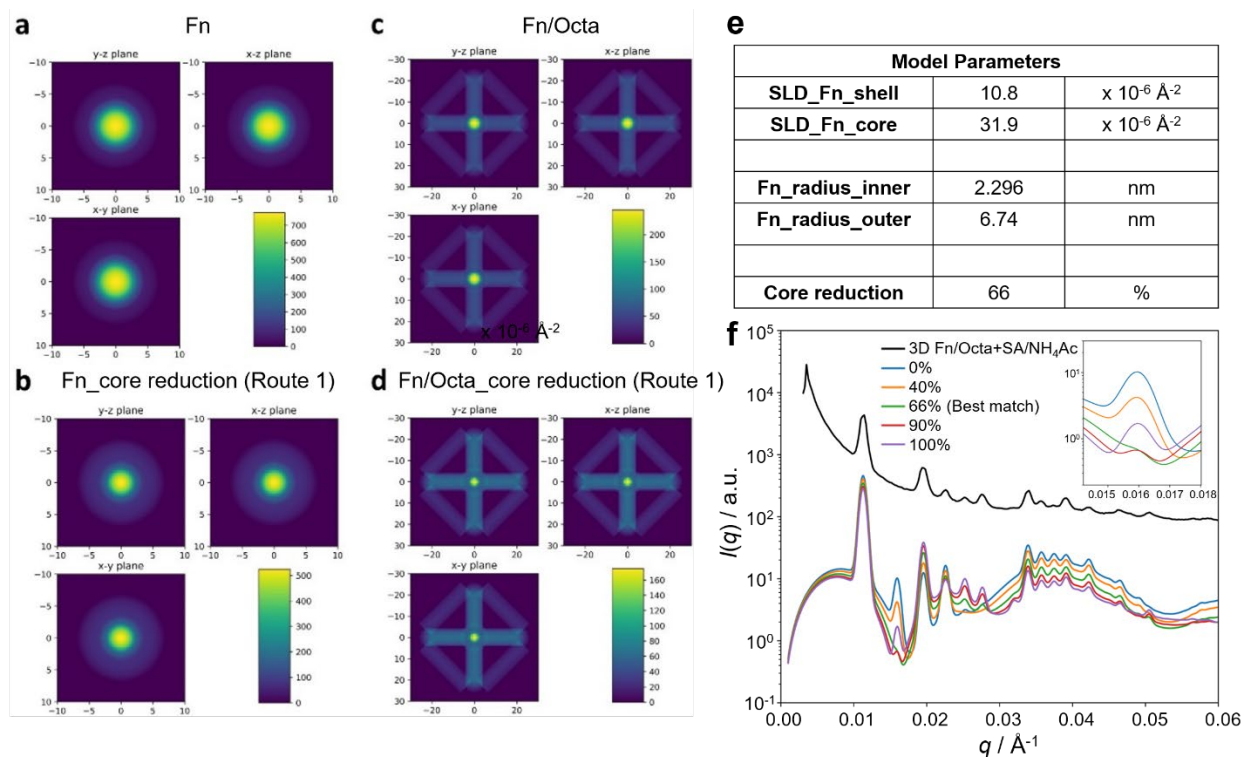
Supplementary Figure 42. a, SAXS analysis and b, TEM images of ferritin/Octa (30 nM) in TAE buffer containing 12.5 mM MgCl_2 , and in the presence of sodium ascorbate (SA, 20 mM) and 10 v/v% of the ammonium acetate (NH_4Ac , pH 5.5) solution.



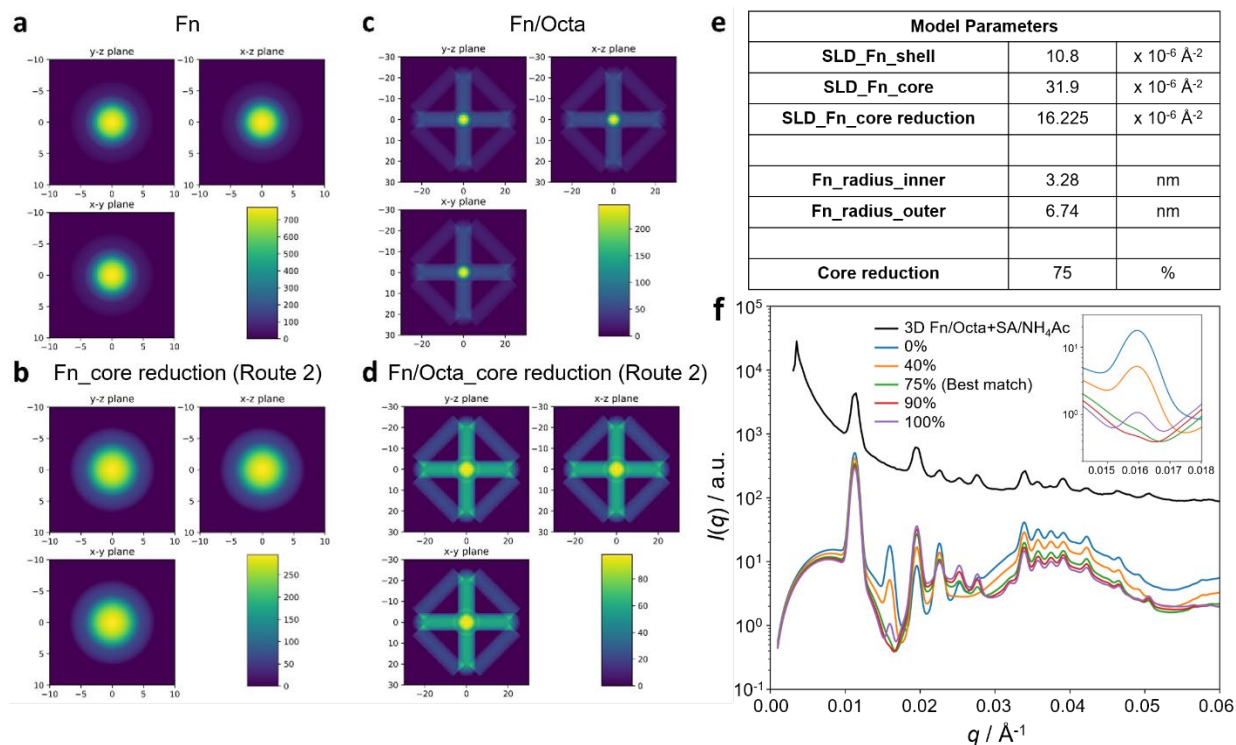
Supplementary Figure 43. Time-dependent SAXS study of the 3D ferritin/Octa lattice in the a, absence or b, presence of sodium ascorbate (SA, 20 mM) and 10 v/v% of the ammonium acetate (NH_4Ac , pH 5.5) solution. The black dashed lines indicate the scattering peaks that are expected to change in intensities during the conversion from a 3D ferritin/Octa lattice to a 3D apoferritin lattice. Peak positions are normalized by the center of the 1st peak.



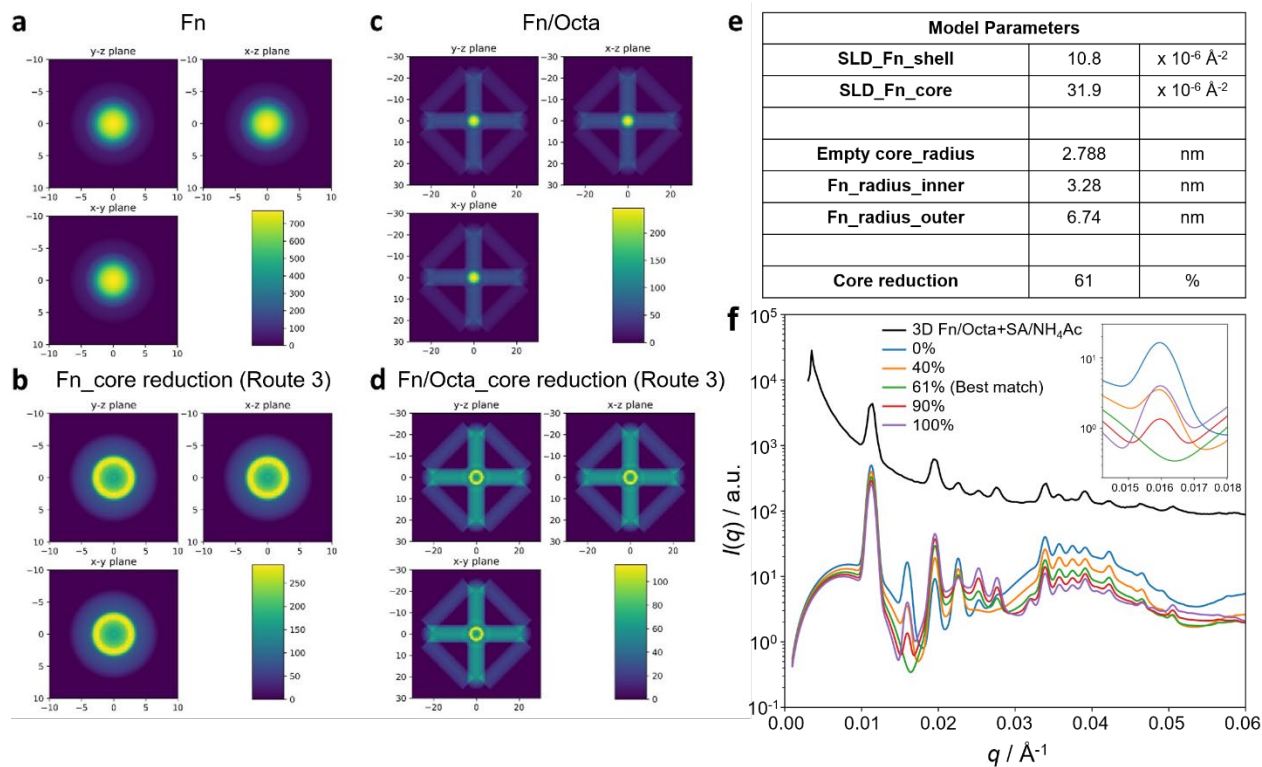
Supplementary Figure 44. Projections of NanoObjects used in the ScatterSim python library. a, Projections of the CoreShellNanoObject with the model parameters for ferritin (Fn). b, Projections of the CoreShellNanoObject with the model parameters for apoferritin (Apfn). c, Projections of the OctahedronCylindersNanoObject with the model parameters for the octahedral origami (Octa). d, Projections of the CompositeNanoObject with the model parameters for the ferritin isolated inside the modelled Octa (Fn/Octa). e, Projections of the CompositeNanoObject with the model parameters for the apoferritin isolated inside the modelled Octa (Apfn/Octa). f, Parameters used in the SAXS Models. The units for the projections are in nm, and the colormap shows relative electron/scattering length density.



Supplementary Figure 45. Projections of NanoObjects before and after core dissolution based on decrease in size at the surface of the ferritin core (route 1). a-b, Projections of ferritin (Fn) a, before and b, after core reduction, c-d, Projections of ferritin isolated inside the modelled Octa c, before and d, after reduction at the ferritin core. e, Parameters used in the SAXS Models for this dissolution mechanism. The units for the projections are in nm, and the colormap shows relative electron/scattering length density. f, SAXS modelling (colored curves) that correlated the SAXS profiles with core reduction based on the route 1 mechanism was used to analyze the extent of conversion of the ferritin array, of which the experimental result (black curve) corresponded the best to an average of 66% of reduced cores. Ferritin reduction was performed using sodium ascorbate (SA, 20 mM) solution containing ammonium acetate (NH₄Ac, pH 5.5). Inset: zoomed-in region of SAXS models for the 2nd peak, or the (110) Bragg plane.



Supplementary Figure 46. Projections of NanoObjects before and after core dissolution based on reduction of the overall electron density of the ferritin core (route 2). a-b, Projections of ferritin (Fn) a, before and b, after core reduction. c-d, Projections of ferritin isolated inside the modelled Octa c, before and d, after reduction of the ferritin core. e, Parameters used in the SAXS models for this dissolution mechanism. The units for the projections are in nm, and the colormap shows relative electron/scattering length density. f, SAXS modelling (colored curves) that correlated the SAXS profiles with core reduction based on the route 2 mechanism was used to analyze the extent of conversion of the ferritin array, of which the experimental result (black curve) corresponded the best to an average of 75% of reduced cores. Ferritin reduction was performed using sodium ascorbate (SA, 20 mM) solution containing ammonium acetate (NH₄Ac, pH 5.5). Inset: zoomed-in region of SAXS models for the 2nd peak, or the (110) Bragg plane.



Supplementary Figure 47. Projections of NanoObjects before and after core dissolution based on decrease in size from the center of the ferritin core (route 3). a-b, Projections of ferritin (Fn) a, before and b, after core reduction. c-d, Projections of ferritin isolated inside the modelled Octa c, before and d, after reduction of the ferritin core. e, Parameters used in the SAXS models for this dissolution mechanism. The units for the projections are in nm, and the colormap shows relative electron/scattering length density. f, SAXS modelling (colored curves) that correlated the SAXS profiles with core reduction based on the route 3 mechanism was used to analyze the extent of conversion of the ferritin array, of which the experimental result (black curve) corresponded the best to an average of 61% of reduced cores. Ferritin reduction was performed using sodium ascorbate (SA, 20 mM) solution containing ammonium acetate (NH_4Ac , pH 5.5). Inset: zoomed-in region of SAXS models for the 2nd peak, or the (110) Bragg plane.

Supplementary Methods

Materials

Single-stranded DNA (ssDNA) sequences were purchased from Integrated DNA Technologies and the M13mp18 ssDNA scaffold was purchased from Bayou Biolabs. Ferritin and apoferritin from horse spleen, phosphate buffered saline (PBS), magnesium chloride (MgCl_2), azido-dPEG₈-NHS ester, agarose (medium EEO), ferrozine ($\text{C}_{20}\text{H}_{13}\text{N}_4\text{NaO}_6\text{S}_2$) ammonium hydroxide, acetic acid, and phosphate buffered saline were purchased from Sigma Aldrich. (+)-Sodium L-ascorbate was purchased from Fluka. The 10X tris-acetate-ethylenediaminetetraacetic acid (TAE) and 10X tris-borate- ethylenediaminetetraacetic acid (TBE) buffers, 10X BlueJuice gel loading buffer, SYBR Gold (10,000x) dye were purchased from ThermoFisher Scientific. Carbon grid (200 mesh copper) and uranyl acetate solution were purchased from Electron Microscopy Sciences. Milli-Q (18 M Ω · cm) was used for all the experiments.

Agarose gel electrophoresis (AGE)

For AGE of Octa structures, agarose (1.0 wt%) was prepared in TBE (1X) buffer containing 12.5 mM MgCl_2 and 1X SYBR Gold dye. Octa and protein/Octa (10 nM, 20 μL) were mixed with 1X BlueJuice gel loading buffer prior to loading into the gel. Electrophoresis was performed at 60 V on ice to prevent heating damage. Similarly, AGE of ssDNA modified proteins was performed by mixing protein samples (1 μM , 20 μL) with loading buffer. After loading, electrophoresis was performed at 70 V on ice.

Dynamic light scattering (DLS)

Octa (5 nM) was dispersed in TAE buffer containing 12.5 mM MgCl_2 and proteins (0.1–2 μM) were dispersed in PBS buffer. The samples were measured 3 times with Zetasizer Nano Z (Malvern Analytical) with an equilibrium time of 120 s.

Small-angle X-ray scattering (SAXS) experiment and analysis

1) Data acquisition of proteins, single Octa and single protein/Octa:

Solution scattering data was collected at the Life Sciences X-ray Scattering beamline (LiX, 16-ID) at the National Synchrotron Light Source II (NSLS-II), Brookhaven National Laboratory (BNL). LiX utilizes an undulator source and a Si(111) monochromator. KB mirrors focus the

beam on a secondary source and X-ray energy was 12 keV with a beam size of ~400 um. An in-house solution scattering box houses a movable 3 channel flow cell such that proteins in solution flow through the beam during collection. Data was collected on 3 Pilatus detectors (SAXS: Pilatus 1M, 2 offset WAXS detectors: Pilatus 300K).¹ The data was merged, averaged, subtracted and packed into HDF5 format using the in-house py4xs software², with data visualization in jupyter notebook. For each sample exposed to the X-ray beam, five frames, with an exposure time of 1 s was collected and processed using py4xs.

2) SAXS data acquisition of 2D and 3D Octa and protein/Octa lattices:

The scattering data of Octa and protein/Octa lattices were collected at the Complex Materials Scattering (CMS, 11-BM) beamline at the NSLS-II at BNL. Measurements were carried out in transmission mode with the X-ray energy $E = 13.5$ keV ($\lambda = 0.9184$ Å) using a 2D detector, Pilatus 1M, with a sample-to-detector distance of 5.05 m. The 2D scattering images were converted into 1D scattering intensity profiles through azimuthal integration. The intensity $I(q)$ is expressed as a function of the scattering vector magnitude q , where $q = \frac{4\pi \sin \theta}{\lambda}$ with 2θ being the full scattering angle.

3) SAXS modelling:

The SAXS modeling was primary performed using the ScatterSim software package^{3,4}, a python library for simulating 1D curves for the clusters and superlattices built from arbitrary anisotropic nanoscale objects.^{3,4}

a. Modeling of single-particle proteins

The ferritin and apoferritin were modelled with a core-shell structure.

$$F(q, r_{core}, r_{total}) = 3 \left[V_{core} (\rho_{core} - \rho_{shell}) \frac{\sin(qr_{core}) - qr_{core} \cos(qr_{core})}{(qr_{core})^3} + V_{total} (\rho_{shell} - \rho_{solvent}) \frac{\sin(qr_{total}) - qr_{total} \cos(qr_{total})}{(qr_{total})^3} \right] \quad (1)$$

where ρ_{core} , ρ_{shell} and $\rho_{solvent}$ are electron density of the core, shell and solvent, respectively; r_{core} and V_{core} are the radius and the volume of the core; r_{total} and V_{total} are the radius and the volume of the whole core-shell structures.

The scattering form factor $P(q)$ is expressed as,

$$P(q) = \frac{|F(q, r_{core}, r_{total})|^2}{V_{total}} \quad (2)$$

For the polydisperse core-shell structure,

$$P(q) = \int \frac{|F(q, r_{core}, r_{total})|^2}{V_{total}(r_{core}, r_{total})} D(r_{core}) D(r_{total}) dr_{core} dr_{total} \quad (3)$$

where $D(r)$ is the size distribution function, and the Gaussian distribution is used in this model. We note that $\int D(r_{core}) D(r_{total}) dr_{core} dr_{total} = 1$.

The fitting results of free ferritin (Fn) and apoferritin (Apfn) in the aqueous solutions are shown in Fig. 2. The apoferritin was modeled as a hollow protein with a spherical shell. The electron density (ED) of the shell was estimated be $0.42 \text{ e}/\text{\AA}^3$, corresponding to a scattering length density (SLD) of $\text{SLD}_{\text{shell-Apfn}} = 11.8 \times 10^{-6} \text{ \AA}^{-2}$. The SLD of the aqueous solution inside and outside of the protein shell was $\text{SLD}_{\text{water}} = 9.43 \times 10^{-6} \text{ \AA}^{-2}$. Based on the fit, the radii of the apoferritin core and shell were $r_{\text{core-Apfn}} = 4.03 \pm 0.81 \text{ nm}$ and $r_{\text{total-Apfn}} = 6.05 \pm 0.43 \text{ nm}$, respectively.

The ferritin was modeled as an iron-encapsulated apoferritin, *i.e.*, a spherical core-shell structure with a protein shell and an iron-concentrated core. The ferritin shell was slightly expanded compared to apoferritin, where the SLD of the ferritin shell was $\text{SLD}_{\text{shell-Fn}} = 10.8 \times 10^{-6} \text{ \AA}^{-2}$. Based on the fitting result shown in Fig. 2, we obtained $r_{\text{core-Fn}} = 3.28 \pm 0.61 \text{ nm}$, $r_{\text{total-Fn}} = 6.74 \pm 0.26 \text{ nm}$ and $\text{SLD}_{\text{core-Fn}} = 31.9 \times 10^{-6} \text{ \AA}^{-2}$.

b. Modeling of single-particle Octa

The Octa model was built using ‘‘OctahedronCylindersNanoObject’’ in the ScatterSim package. The octahedral DNA frame was made up of 12 edges, and each edge of the Octa was a six-helix bundle (6HB) and was modelled as a cylinder with a radius of r_{cylinder} and a length of h_{cylinder} . The overall length of the edge of the octahedron is L_{octa} . The SLD of the 6HB was approximately $11 \times 10^{-6} \text{ \AA}^{-2}$. Based on the best fit of the SAXS profile, we obtained $r_{\text{cylinder}} = 4.16 \text{ nm}$, $h_{\text{cylinder}} = 27.8 \text{ nm}$, and $L_{\text{octa}} = 38.3 \text{ nm}$, which agreed with the Octa design.

The protein encapsulated Octa (protein/Octa) was considered as a non-overlapping ‘‘composite’’ object of the Octa frame and a protein inside. Such composite structure was modelled using the ‘‘CompositeNanoObject’’ in ScatterSim, which took into account the interference between the sub-components. We note that in our SAXS modelling we have refrained from introducing fixed distortion of octahedron shapes and polydispersity of its shape. While this effect might be present to some degree, as suggested by the cryo-EM single particle reconstruction, it also revealed that distortion was relatively small. Adding such effects in SAXS scattering would introduce several additional parameters and will increase a complexity of modeling significantly. Such studies will require a dedicated investigation, which will be addressed in the future work. We assumed that protein encapsulation in the Octa did not change the overall geometry of both

the protein and the Octa, as confirmed by our electrophoresis, EM and DLS results (Fig. 2, Supplementary Figs. 10–12).

Thus, the SAXS modeling parameters, such as geometry and SLD of the sub-components, were obtained from the fitting results of the free-dispersed individual sub-components. As shown in Supplementary Fig. 13, apoferritin/Octa showed a similar scattering profile to the Octa only; however, the 1st local minimum shifted to the high q while the 2nd shifted to the low q after the apoferritin encapsulation. These features were consistent with simulated results. In terms of ferritin/Octa, the scattering intensities of first two local maxima (at 0.022 Å⁻¹ and 0.038 Å⁻¹) changed dramatically as the electron density of the ferritin core was much higher than the protein shell and the Octa frame. Particularly, the 1st maximum was suppressed, and the 2nd maximum was enhanced, which were confirmed by the modeling.

The relative position of the protein to the Octa structures were tuned in our designs (see designs of Off1 and Off2 in Supplementary Fig. 7). In the SAXS model, the position of protein inside Octa could be controlled in the “composite” model. By shifting the position of the protein from the center of the Octa towards one of the vertices by a specific distance d_{shift} , center-shifted protein/Octa model were built. Specifically, we assumed that $d_{\text{shift-Off1}} = 3$ nm and $d_{\text{shift-Off2}} = 5$ nm. The modeling results showed that the increase of the d_{shift} led to the increase of the 1st local maxima of the scattering profiles for ferritin/Octa while apoferritin/Octa did not show any clear change. All these trends and features shared similarity with the experimental observations.

c. Modeling of protein and DNA origami arrays

To model the 2D and 3D protein arrays, the protein/Octa composite was used as a simple object to build unit cells of the lattice using ScatterSim. More details of the 3D SAXS analysis can be found in our recent work⁵. The scattering intensity profiles $I(q)$ for the periodic lattices were simulated by:

$$I(q) = cZ_0(q)G(q) + P(q)(1 - \beta(q)G(q)) \quad (4)$$

where c is an overall scaling factor, $P(q)$ is the form factor intensity of the composite object comprised of all objects in the lattice (assuming their relative positions and orientations were preserved), and

$$Z_0(q) = \frac{1}{q^2} \sum_{\{hkl\}} m_{hkl} \left| \sum_{j=1}^N \langle F_j(\mathbf{q}_{hkl}) \rangle_{\epsilon} \exp[2\pi i(x_j h + y_j k + z_j l)] \right|^2 L(q - q_{hkl}) \quad (5)$$

is known as the lattice factor, where $L(q - q_{hkl})$ is a peak shape function. The structure and symmetry of the lattice was taken into account by properly sampling over the correspondent Miller indices q_{hkl} . $G(q)$ is the Debye-Waller factor arise from thermal vibrations in the lattice and is defined as:

$$G(q) = e^{-q^2 \sigma_{D,rms}^2} \quad (6)$$

where $\sigma_{D,rms}$ is the rms displacement of the elements in the lattice. For a simple cubic lattice of unit cell size a , the equation can be re-written as a fractional displacement of the lattice length as

$\sigma_{DW} = \frac{a}{\sigma_{D,rms}}$. Finally, $\beta(q)$ is defined as:

$$\beta(q) = \frac{\langle |F(q)|_\epsilon \rangle^2}{\langle |F(q)|^2 \rangle_\epsilon} \quad (7)$$

and arises from any polydispersity in parameters ϵ . The effect of $G(q)$ under increasing thermal vibrations leads to a reduced ordered scattering from $Z_0(q)$ and an increased the diffuse scattering from unordered elements. In our case, the effect of $\beta(q)$ was only considered for polydisperse protein due to the more complex trend that depended on the length scales of the parameters ϵ .

The procedure for SAXS modeling of the lattice is briefly described below. First, for the lattice components, we used the same morphological and scattering parameters as those obtained from the single-particle form factor analysis, including size, shape and SLD. Based on these parameters, we built the lattice components with $P(q)$ and $\beta(q)$ being calculated. Next, a lattice geometry (*i.e.*, 2D square, SC, FCC, *etc.*) was introduced and the lattice constants were extracted by fitting the primary peak of the experimental intensity profile $I(q)$ using the built lattice model. Finally, we manually adjusted the Debye-Waller factor, peak shape parameters, scaling factors and the background to match the experimental measurements with the simulated results, based on the empirically the influences of each parameter on lattice properties and the as-simulated intensity profiles, as studied previously³. We did not apply direct non-linear least squares fitting of the intensity profiles because (i) such fitting is extremely time-consuming due to the complex architectures with different types of components in our lattice models and (ii) a fit convergence is limited due to the contribution of diffuse scattering.

Cryogenic electron microscopy (cryo-EM) image processing and 3D reconstruction:

All data processing and reconstruction were done in RELION^{6,7}, including motion correction, CTF estimation, particle picking, 2D classification, 3D initial model, 3D classification and

refinement. Dark gain corrected Movies were imported into RELION3, motion correction was done with RELION's own implementation and CTF estimation was done with CTFFIND4⁸. Particle picking was first done by LoG-based auto-picking (reference-free) in RELION3, and all particle images were then manually inspected in order to remove “bad” particles (partially assembled, of low contrast, or contacting other particles and/or edges of carbon supporting film) and to add missed good particles. The CTF corrected data were then subject to several rounds of unsupervised 2D image classification in an iterative manner in order to get rid of images assigned to bad classes. Particle images assigned to the same class were mutually aligned and averaged to generate a set of high-contrast class averages (good 2D classes) that represented the single apoferritin/Octa structure. A low-resolution reference-free 3D initial model was generated by using particle images assigned to representative 2D classes and imposing no symmetry (C1 symmetry). The starting model was low-pass filtered to 80Å and used for 3D refinement against the CTF corrected particle image dataset without imposing any symmetry (C1 symmetry) throughout the 3D refinement in RELION3. The resolution of the final 3D map was estimated by the so-called “Gold standard” Fourier shell correlation method at the threshold of 0.143.⁹ All image processing and 3D reconstruction were done on a 4-GPU Exxact Linux workstation or a 2-GPU Dell Linux workstation. 3D density map was displayed and manipulated in the UCSF Chimera package¹⁰.

Cryo-electron tomography (cryo-ET) image processing and 3D reconstruction:

Anisotropic image motion of each frame of image stack in super-resolution mode (0.73 Å/pixel) was corrected by MotionCor2¹¹. All tilt series were binned by two times (1.46 Å/pixel) and aligned by IMOD¹². Defocus values were measured by Gctf¹³ and the contrast transfer function (CTF) were corrected by TomoCTF¹⁴. 3D density maps of the whole micrograph were aligned and reconstructed by IMOD, after tilt series were binned eight times (11.68 Å/pixel). For high-resolution 3D structure, a tilt series of a focused area with $\sim 336 \times 336 \text{ nm}^2$, *i.e.* 288 pixel \times 11.68 Å/pixel, was windowed and extracted from the whole micrographic tilt series following the IPET reconstruction protocol¹⁵. In this process, an *ab initio* 3D map back-projected from the raw tilt series was used as an initial model for iterative refinement. During the iteration, a set of Gaussian low-pass filter, and circular and particle-shaped soft-boundary masks were automatically generated and sequentially applied to the tilt images to increase their SNRs during alignment.

To reduce artifact of missing wedge, the 3D map back-projected from the aligned tilt series was submitted for a post process for missing wedge correction¹⁶. The resolution was estimated by calculating the Fourier shell correlation (FSC) curve between two-halves of the reconstructed 3D maps that were generated from odd and even aligned tilt series¹⁷. The frequency at which the FSC curve first fell to 0.5 was used to estimate the resolution of the IPET 3D density map. All 3D maps in the figures were low-pass filtered to 80 Å using ENAN software¹⁷ and displayed in the UCSF Chimera package¹⁰.

Ferrozine-protein assays:

Ferrozine stock solution (10 mM) was prepared by dissolving ferrozine in deionized water. For pH adjustment of the ferrozine solution, an ammonium acetate buffer stock solution was prepared by mixing 19.5 mL of ammonium hydroxide (28% v/v) solution and 15 mL of acetic acid (80%) solution, adjusting the pH to 5.5 with HCl (1 N) solution and making up to 50 mL with deionized water. The ascorbate stock solution (50 mM) was prepared by dissolving sodium ascorbate in deionized water. The ferrozine working solution was prepared by mixing the ferrozine stock solution (5 mL) with the ammonium acetate buffer (3.34 mL) and 1.66 mL of deionized water.

To prepare the ferrozine assays for free ferritin and apoferritin, ascorbate (1 mM and 2.5 mM) and the ferrozine working solution (1 mM) were added to the proteins (50 nM) in PBS. The absorbance kinetics and spectra were measured in a 96 well plate (Corning) using the Spark microplate reader (Tecan). The kinetic assay for tracking the ferrozine-Fe²⁺ complexation was performed by measuring the absorbance at 562 nm every 3 min. The full spectra were scanned from 400 nm-800 nm with a step size of 2 nm.

SAXS sample preparation for iron core reduction in 3D lattice:

The 3D ferritin/Octa lattices (30 nM, 20 µL) were loaded in quartz capillaries and left to precipitate overnight at 4 °C. A sodium ascorbate stock solution (200 mM) was prepared freshly in deionized water prior to experiment. The working solution was prepared by mixing 2 µL of the ascorbate stock solution with 2 µL of the ammonium acetate stock solution (as described above) and added to the lattice solution in the capillary.

Supplementary References

- 1 DiFabio, J. *et al.* The life science x-ray scattering beamline at NSLS-II. *AIP Conference Proceedings* **1741**, 030049, doi:10.1063/1.4952872 (2016).
- 2 Yang, L. Using an in-vacuum CCD detector for simultaneous small- and wide-angle scattering at beamline X9. *Journal of Synchrotron Radiation* **20**, 211-218, doi:doi:10.1107/S0909049512048984 (2013).
- 3 Yager, K. G., Zhang, Y., Lu, F. & Gang, O. Periodic lattices of arbitrary nano-objects: modeling and applications for self-assembled systems. *Journal of Applied Crystallography* **47**, 118-129, doi:10.1107/S160057671302832X (2014).
- 4 Yager, K. G. ScatterSim. <https://github.com/CFN-sofibio/ScatterSim> (2017).
- 5 Tian, Y. *et al.* Ordered three-dimensional nanomaterials using DNA-prescribed and valence-controlled material voxels. *Nature Materials* **19**, 789-796, doi:10.1038/s41563-019-0550-x (2020).
- 6 Scheres, S. H. W. RELION: Implementation of a Bayesian approach to cryo-EM structure determination. *Journal of Structural Biology* **180**, 519-530, doi:<https://doi.org/10.1016/j.jsb.2012.09.006> (2012).
- 7 Zivanov, J. *et al.* New tools for automated high-resolution cryo-EM structure determination in RELION-3. *Elife* **7**, doi:10.7554/eLife.42166 (2018).
- 8 Rohou, A. & Grigorieff, N. CTFFIND4: Fast and accurate defocus estimation from electron micrographs. *Journal of Structural Biology* **192**, 216-221, doi:<https://doi.org/10.1016/j.jsb.2015.08.008> (2015).
- 9 Scheres, S. H. W. & Chen, S. Prevention of overfitting in cryo-EM structure determination. *Nature Methods* **9**, 853-854, doi:10.1038/nmeth.2115 (2012).
- 10 Pettersen, E. F. *et al.* UCSF Chimera—A visualization system for exploratory research and analysis. *Journal of Computational Chemistry* **25**, 1605-1612, doi:<https://doi.org/10.1002/jcc.20084> (2004).
- 11 Zheng, S. Q. *et al.* MotionCor2: anisotropic correction of beam-induced motion for improved cryo-electron microscopy. *Nature Methods* **14**, 331-332, doi:10.1038/nmeth.4193 (2017).
- 12 Kremer, J. R., Mastrorarde, D. N. & McIntosh, J. R. Computer Visualization of Three-Dimensional Image Data Using IMOD. *Journal of Structural Biology* **116**, 71-76, doi:<https://doi.org/10.1006/jsbi.1996.0013> (1996).
- 13 Zhang, K. Gctf: Real-time CTF determination and correction. *Journal of Structural Biology* **193**, 1-12, doi:<https://doi.org/10.1016/j.jsb.2015.11.003> (2016).
- 14 Fernández, J. J., Li, S. & Crowther, R. A. CTF determination and correction in electron cryotomography. *Ultramicroscopy* **106**, 587-596, doi:<https://doi.org/10.1016/j.ultramic.2006.02.004> (2006).
- 15 Zhang, L. & Ren, G. IPET and FETR: Experimental Approach for Studying Molecular Structure Dynamics by Cryo-Electron Tomography of a Single-Molecule Structure. *PLOS ONE* **7**, 1-19, doi:10.1371/journal.pone.0030249 (2012).
- 16 Zhai, X. *et al.* LoTToR: An Algorithm for Missing-Wedge Correction of the Low-Tilt Tomographic 3D Reconstruction of a Single-Molecule Structure. *Scientific Reports* **10**, 10489, doi:10.1038/s41598-020-66793-1 (2020).
- 17 Ludtke, S. J., Baldwin, P. R. & Chiu, W. EMAN: Semiautomated Software for High-Resolution Single-Particle Reconstructions. *Journal of Structural Biology* **128**, 82-97, doi:<https://doi.org/10.1006/jsbi.1999.4174> (1999).